SYNTHESIS AND PROPERTIES OF A NISOD MODEL WITH AN APICAL IMIDAZOLE DONOR

by

JESSICA LINDSEY HOWELL

(Under the Direction of Todd C. Harrop)

ABSTRACT

Nickel superoxide dismutase (NiSOD) is a redox-active, Ni-containing metalloenzyme that disproportionates superoxide to O_2 and H_2O_2 at a diffusion-limited rate. The unique $N^{peptide}N^{amine}S_2^{cysteinate}$ planar donors and loosely bound N^{His} axial donor enables NiSOD to perform chemistry with reactive oxygen species despite its oxygen-sensitive ligands. This has driven synthetic efforts at modelling the active site to better understand the structure-function relationship of NiSOD. To this end, this work presents the fourth generation of five-coordinate NiN_3S_2 complex from our group, $[Ni(N_3S_2^{NMeIm})]^-$ (**1**), that features an electronically and structurally accurate 1-methylimidazole (NMeIm) axial donor that is expectated to promote 5C Ni^{2+} with a long Ni---N_{axial} bond that is poised for functionality. Characterization of **1** is very similar to prior models however, its reactivity with oxidants suggests an enhanced electronic structural similarity to NiSOD, emphasizing the role of the axial donor as well as secondary protein structure on the functionality of NiSOD.

INDEX WORDS: Nickel, Superoxide Dismutase, Metalloenzyme, Thiolate, Model Complex

SYNTHESIS AND PROPERTIES OF A NISOD MODEL WITH AN APICAL IMIDAZOLE DONOR

by

JESSICA LINDSEY HOWELL

B.S, University of North Georgia, 2017

A Thesis Submitted to the Graduate Faculty of the University of Georgia in Partial Fulfillment of the Requirements for the Degree

MASTER OF SCIENCE

ATHENS, GEORGIA

2021

SYNTHESIS AND PROPERTIES OF A NISOD MODEL WITH AN APICAL IMIDAZOLE DONOR

by

JESSICA LINDSEY HOWELL

Major Professor: Todd C. Harrop

Committee: Jeffrey L. Urbauer
Jason Locklin

Electronic Version Approved:

Ron Walcott
Vice Provost for Graduate Education and Dean of the Graduate School
The University of Georgia
December 2021

DEDICATION

To my husband, Corbin Smith and my parents, Charles and Andrea Howell.

ACKNOWLEDGEMENTS

First, I must thank my advisor, Dr. Todd Harrop, for believing in me and providing me the resources and mentorship I needed to achieve this. Thank you for sharpening me into the independent thinker, scientist, speaker, and person I am today. I would also like to thank Dr. Jeffrey Urbauer and Dr. Jason Locklin for serving on my graduate committee and supporting me. I'm very grateful to the research professionals at UGA including Dr. Dennis Phillips, Dr. Dongtao Cui, Dr. John Glushka, and Dr. Earle Adams for your expertise with mass spectrometry and NMR spectroscopy. I would also like to thank Dr. Indranil Chakraborty at the University of Miami and the late Dr. Marilyn Olmstead at the University of California, Davis for their X-ray crystallography expertise. Thank you, Dr. Olmstead especially for collecting my very first crystal structure and the strong example you are for women like me in chemistry. Lastly, I'd like to thank so many people in the chemistry department from the front office to the facilities management. Thank you, Cedrick Henson, Floyd Johnson, and Travis Bailey, for the countless times you helped me when I was locked out at night and for sharing your lives with me. Terri Tillman, you made my seminar on Alzheimer's disease mean so much more and I'm honored to know the story of your cousin Mark.

To the Harrop group alumni that I was able to connect with, Dr. Phan Truong and Dr. Melody Walters, thank you for all your kindness and support when I needed it. Your advice, collaboration, and friendship remind me of older siblings, and I've always felt so comfortable coming to you. To my current group members, Yi Liu, Ben Yosen, Jordan Ernst, Cole Nguyen, and Adrian Torres, thank you all so much for your friendship, emotional support, and scientific help not to mention all the baked goods, desk lunches, and laughs along the way. I especially want

to thank Ben for being with me from the beginning and never missing the opportunity for a pun, deep conversation, or desk prank and ultimately, being an unparalleled friend. To my other friends, my fellow Grad Scouts: Holli Threlkeld, Brianna Blevins, Laura Andreola, Maddi Smith, Divine Francis, Rachel Bramblett, and Caitlyn Cato, thank you for always being there and reaching out to me, I can't tell you how much your encouragement and love fueled me. And to my best friend Rebekah Brucato, thank you for your love and easy friendship through each of our adventures.

Mom and Dad, I don't even know how to put into words everything that you've done to help me achieve this. You never failed to be there for me and give me the words, food, laughter, wisdom, music, love and so much more that you always knew I needed. I'm so grateful to all my other family, especially Memaw and Grampa. Every time I'm with you, I feel like a carefree kid in Alabama again and I'll always need that. To my uncle and earliest friend Peter, thank you for always being willing to listen and give me the perspective (and cousin/god-daughter, Arwyn) I needed to make the right choices with the bigger picture in mind. I'd also like to thank the family I married into, especially Michelle Beasley for never turning away a listening ear and Nick Beasley, now my little brother, for your constant joking, selfless help, and staying up late with me while I achieved this. To my family that are no longer here, Nanu, Pawpaw, and Uncle Bubba, thank you for your enduring example of pure joy, grit, and endurance. I'd do anything to hear that laugh, see that wink, and feel that proud hug I know you'd have for me right now.

Lastly, thank you to my spouse and best friend of all time, Corbin Smith. I can't overstate how much of my achievement is shared by you. You have been an anchor for me through this and the unpredictable turns the past three years have thrown at us all. I would double the page count of this work if I put into words what you've done for me. Your love, spiritual guidance, humor, selflessness, and patience are beyond my ability to write (but not beyond yours). I love you.

TABLE OF CONTENTS

Page

CHAPTER 1

INTRODUCTION

1.1 Nickel in Biology

Nickel (Ni) was first discovered as a unique element in 1751 by Swedish mineralogist and chemist, Axel Fredrik Cronstedt, from an ore called *kupfernickel.*[1-3] German miners gave it this name (*kupfer* meaning copper; *nickel* a mischievous spirit) as they believed it to be a particularly tricky copper ore from which they continually failed to isolate copper.[1, 3] Since its storied discovery, Ni has been found in a variety of settings including in trace amounts in the Earth's crust (75 ppm), the oceans (8 nM), in meteorites and primarily in the Earth's core (4×10^{-4} - 20×10^{-4} ppm).[3-4] Ni was brought up to Earth's surface by volcanic activity 2.5 to 4 billion years ago and is now found primarily as sulfide deposits such as pyrrhotite (Fe_nS_{n+1} with 3-5.5% Ni), pentlandite ($(Ni, Fe)_9S_8$), and millerite (NiS).[5-8] In addition to crustal levels of solid Ni growing, soluble (bioavailable) levels Ni in the oceans have since also increased, allowing Ni to be incorporated into the chemistry of life processes.[5] Before the Great Oxidation Event which brought a massive increase in O_2 levels and decrease in soluble Ni levels, Ni came to be utilized in biological systems similar to the environments in which it was found: anaerobic and sulfur-rich.[8-10] Accordingly, the earliest organisms on Earth were anaerobic, extremophilic (living in extreme temperature, pH, and/or chemical concentration conditions) and Ni-dependent archaea and bacteria which would become the ancestors to organisms found in similar environments today such as *Escherichia coli*, *Desulfovibrio desulfuricans,* and *Moorella thermoacetica.* [11-14]

1.2 Nickel-Containing Metalloenzymes

These primarily anaerobic organisms take advantage of Ni chemistry in the form of Ni-containing metalloenzymes which participate in reactions central to global carbon (CH_4, CO, CO_2), nitrogen ($CO(NH_2)_2$ = urea), hydrogen (H_2), and interestingly, oxygen (O_2, $O_2^{\bullet-}$, H_2O_2) cycles (Table 1.1).[13-15] A wide variety of chemistry is performed by such enzymes due to the flexible nature of Ni with regards to coordination environment, oxidation state, and redox potential window.[15] Current studies indicate that Ni coordinates to C, H, N, and O in a variety of geometries spanning three oxidation states (1+, 2+, 3+) and a potential window of ~1.5 V.[15-16] Ni is present in these enzymes clustered with other Ni and Fe metal centers and alone as the sole metal center.[14] To date, nine unique Ni-containing metalloenzymes have been discovered and can be broadly categorized into two groups: (i) redox-active, and (ii) non-redox-active.[14-15]

Table 1.1. Ni-containing metalloenzymes, the role of Ni, and enzyme function.

Enzyme (Abbreviation)	Role of Ni	Enzyme Function
Acireductone dioxygenase (ARD)	Lewis Acid	Methionine salvage
Glyoxalase I (Glx I)	Lewis Acid	Detoxification of methylglyoxal
Urease	Lewis Acid	Urea hydrolysis
Lactate racemase (LarA)	Unclear	Racemization of D- and L-lactic acid
Methyl-CoM reductase (MRS)	Redox	Synthesis of methane
CO dehydrogenase (CODh)	Redox	Reversible $CO \leftrightarrow CO_2$ conversion
Acetyl-CoA synthase	Redox	Synthesis of acetyl-CoA
[NiFe]-hydrogenase ([NiFe]-H_2ase)	Redox	Reversible $H_2 \leftrightarrow 2H^+$ conversion
Ni superoxide dismutase (NiSOD)	Redox	Disproportionation of superoxide ($O_2^{\bullet-}$)

1.2.1 Non-redox-active Ni-containing Metalloenzymes

Non-redox-active Ni-containing enzymes use Ni^{2+} as a Lewis acid to optimally orient substrates and active-site components as well as to direct chemical reactivity towards bound substrates.[17-19] Lactate racemase (LarA) was most recently discovered in 2014 and while the function of Ni in this enzyme is still not fully understood, evidence indicates that hydride transfer does not directly involve the Ni^{2+} which remains unchanged throughout catalysis.[16, 20] Another feature of non-redox-active Ni-containing enzymes (with potential exception of LarA) is exclusive N/O coordination to the Ni center. Unlike the non-redox-active category, redox-active Ni-containing metalloenzymes exclusively incorporate N/S coordination of Ni (excluding intermediates formed during catalysis).[15] A feature of almost all redox-active Ni-containing enzymes is the coordination of Ni to S atoms as thiolates or sulfides from Cys residues or [FeS] clusters, respectively. The high Lewis basicity of these S ligands enables Ni to traverse multiple oxidation states, promoting the redox activity required for a diverse array of challenging chemical processes.

1.2.2 Redox-active Ni-containing Metalloenzymes

1.2.2.1 Methyl coenzyme M reductase

The entirety of biological methane (CH_4) production is carried out by methanogenic archaea which employ methyl-coenzyme M reductase (MCR) and therefore plays an essential role in the global carbon cycle.[21] Crystal structures of MCR reveal a helical heterohexameric protein made of three unique subunits ($\alpha_2\beta_2\gamma_2$) (Figure 1.1). Both α-subunits incorporate one Ni active site featuring the most reduced cyclic tetrapyrrole in nature, with only 5 double bonds, bound to Ni *via* four pyrrole-N donors and one axially bound Gln side chain.[14, 22] These sites, known as

coenzyme F430, are bound at the end of a 50 Å long hydrophobic channel deep inside the protein to prevent solvent access.[22-23] It is here that the final step of biological methane production is carried out: conversion of methyl-coenzyme M (CH_3-S-CoM) and coenzyme B (CoB-SH) into CH_4 and heterodisulfide CoM-S-S-CoB. It is clear that the active form of MCR begins with Ni^+ however the next step in the mechanism is still under investigation. The two proposed mechanisms involve (i) Ni^+ nucleophilically attacking methyl-CoM to bind CH_3 or (ii) Ni^+ binding to the S of methyl-CoM to promote homolytic cleavage of the H_3C-S bond and generate $CH_3^{+\bullet}$.[15, 24]

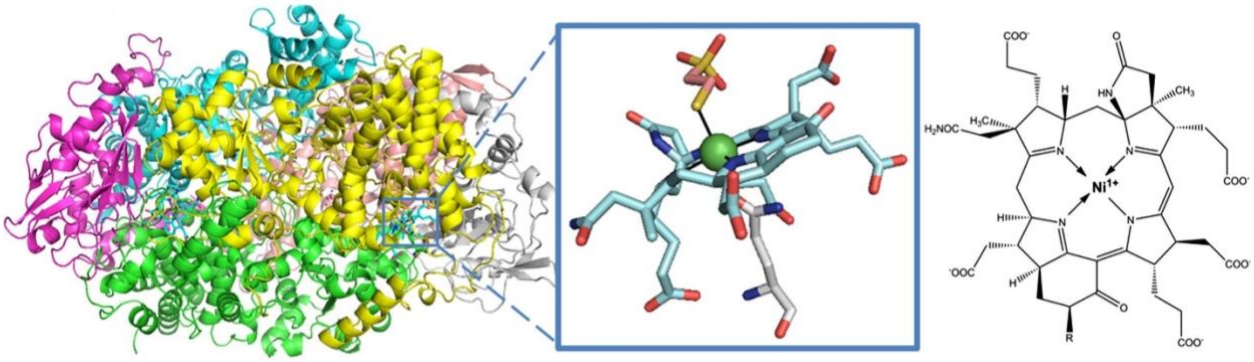

Figure 1.1. MCR structure (*left*) and active site (*middle*) from *Methanothermobacter marburgensis* (PDB: 1MRO) at 1.45 Å resolution.[25] Each active site (Ni as a green sphere with ligands in stick view) contains coenzyme F430 with an axial Gln ligand, and an additional axially coordinated CoM-SH in this particular structure. A line drawing of coenzyme F430 is illustrated for clarity (*right*), where R is H or S-CH_3, depending on the source. Images from ref 13.[13]

1.2.2.2 Acetyl-CoA synthase/Carbon monoxide dehydrogenase

Nickel-containing carbon monoxide dehydrogenase (CODh) holds an essential role in the global carbon cycle as it catalyzes the *reversible* oxidation of carbon monoxide (CO) to carbon dioxide (CO_2), a well-studied greenhouse gas.[15] CODh is found as both a homodimeric enzyme (α_2) (Figure 1.2) as well as a subunit of a larger bifunctional, tetrameric $\alpha_2\beta_2$ protein comprised of two CODh units and two acetyl-CoA synthase units (*vide infra*, Figure 1.3). In both settings, each

pair of CODh subunits has five metal clusters in total including two C-clusters, two B-clusters, and one D-cluster arranged in a V-shape with C-B-D-B-C order. The inner-most clusters, B and D, are [Fe_4S_4] clusters that serve as an electron transport from the terminal C-clusters which are [$NiFe_4S_4$] clusters that catalyze the oxidation of CO. C-clusters can also be thought of as [NiFe-Fe_3S_4] clusters as chemistry takes place specifically at the [NiFe] portion of the C-cluster where the catalytic cycle begins with Ni^{2+} in a trigonal pyramidal geometry, bound to one S-Cys and two S-sulfides of the connected [Fe_4S_4] cluster. The proposed mechanism of CO oxidation by CODh is very similar to the water-gas shift reaction ($CO + H_2O \rightleftharpoons CO_2 + H_2$) in that CO binds the Ni^{2+} which appropriately positions CO near an Fe-bound OH^- that nucleophilically attacks Ni-CO.[26-27] This step forms a bridging Ni-carboxylate-Fe intermediate that decomposes to release CO_2 and two electrons which are shuttled away from the C-cluster *via* the B and D-clusters.[28-29]

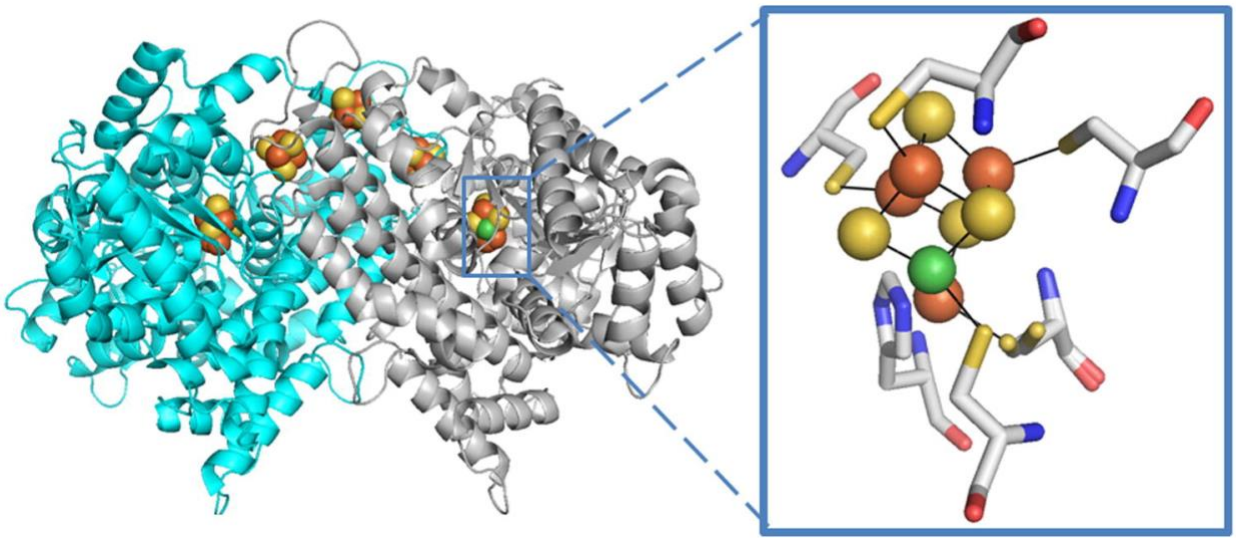

Figure 1.2. The dimeric CODH structure (*left*) and active site (*left*) from *Carboxydo thermus hydrogenoformans* (PDB: 3B53) at 1.50 Å resolution.[30] Two [1Ni–4Fe–4S] clusters and three [4Fe–4S] clusters including one that bridges the subunits are depicted with spheres (Ni in green, Fe in orange, S in yellow). Images from ref 13.[13]

Mentioned above, acetyl-CoA synthase (ACS), is a subunit of CODh/ACS, a larger bifunctional, tetrameric $\alpha_2\beta_2$ protein comprised of two central CODh units that separate each ACS unit (Figure 1.3). When coupled to CODh as CODh/ACS, this protein complex carries out a version of the Wood-Ljungdahl pathway, which may have been the first metabolic process to arise on Earth.[31] ACS catalyzes the condensation of CH_3, CO, and CoA into acetyl-CoA, a cellular energy source and carbon building block. ACS houses one A-cluster (per subunit) that is connected by a 140 Å long hydrophobic tunnel to the C-cluster of one CODh subunit.[26] The A-cluster is a NiFeS cluster made of three parts: (i) a $[Fe_4S_4]$ cluster bridged by one S-Cys to (ii) Ni_p (proximal Ni) which is coordinated by two additional S-Cys that each bridge to (iii) Ni_d (distal Ni) which is also bound to two backbone peptide-N in a four-coordinate (4C) N_2S_2 square planar geometry. The very stable Ni_d site does not participate in catalysis and remains in a 2+ oxidation state throughout, unlike Ni_p which is the site of all redox activity and chemical transformation.[26] Evidence suggests that when CODh performs reduction of CO_2 to form CO (i.e., the reverse of the aforementioned CODh reaction), the released CO travels from the C-cluster through the long tunnel to the A-cluster where reduced Ni_p binds CO as well as a methyl group from a corrinoid FeS protein (CFeSP).[26, 32] CO then inserts itself into the Ni_p^{2+}-CH_3 bond to form a Ni_p^{2+}-acetyl intermediate at which point CoA binds, prompting thiolysis of the Ni_p^{2+}-acetyl bond, and releases acetyl-CoA. There is still mechanistic discussion about the order of CO and CH_3 binding however, proposed mechanisms agree that all redox activity takes place at Ni_p which exhibits either a paramagnetic or diamagnetic transition state passing through $Ni_p^{+/2+/3+}$ or $Ni_p^{0/2+}$ oxidation states, respectively.[33-34]

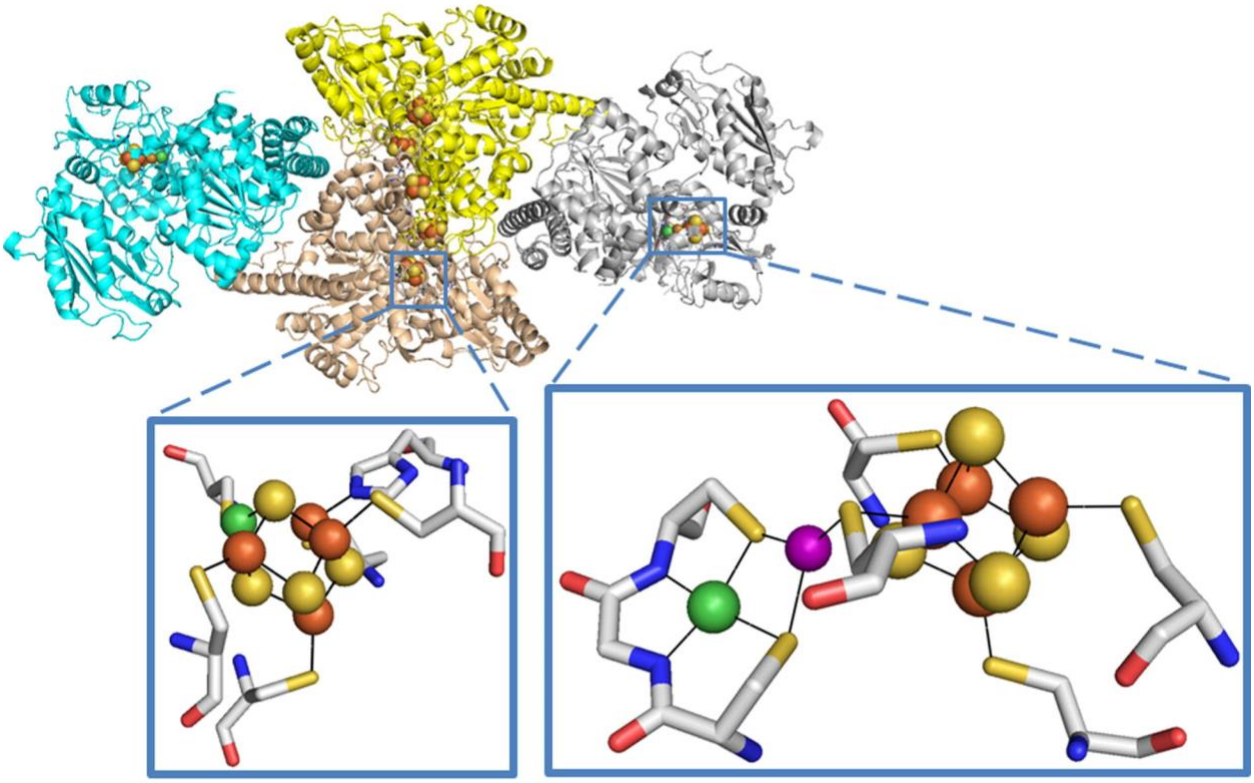

Figure 1.3. CODh/ACS structure (CODh subunits in yellow and beige; ACS subunits in blue and gray) and active sites (CODh on left, ACS on right) from *Morella thermoacetica* (PDB: 2Z8Y) at 2.5 Å resolution.[32] Two [1Ni–4Fe–4S] clusters and three [4Fe–4S] clusters from CODh, including one bridging to each ACS subunit, which each contain a [Ni–M–4Fe–4S] cluster are depicted with spheres (Ni in green, Fe in orange, S in yellow). The structure shown is for an inactive protein where M is Cu (purple sphere), but the active enzyme possesses Ni at this site. Images from ref 13.[13]

1.2.2.3 [NiFe] hydrogenase

Hydrogenases (H_2ases) are used by anaerobic microbes to reversibly catalyze the two-electron reduction of two protons (2 H^+) to hydrogen gas (H_2), making them essential players in the global hydrogen cycle. H_2ases are categorized by their metal center(s) and are thus broken down into three types: (i) [FeFe]-H_2ases, (ii) [Fe]-H_2ases, and (iii) [NiFe]-H_2ases.[35] [NiFe]-H_2ase is an $\alpha\beta$ heterodimeric protein that buries the [NiFe] active site in the α subunit at the end of a 30 Å tunnel through the β subunit that is lined with three FeS clusters (distal $[Fe_4S_4]_d$, medial

$[Fe_3S_4]_m$, and proximal $[Fe_4S_4]_p$), each spaced ~13 Å apart (Figure 1.4).[36] At the active site, Ni is bound by four S-Cys (or three and one Se-Cys) in a seesaw geometry with two S-Cys forming a bridge to an adjacent $Fe(CO)(CN)_2$ held in a distorted square pyramidal geometry. Ni cycles through 3+, 2+, and 1+ oxidation states to perform catalysis while Fe does not participate in the redox process, maintaining a 2+ oxidation state throughout. The active site is first activated by heterolytically cleaving H_2 followed by the loss of one H^+ and one electron *via* proton-coupled electron transfer (PCET). This forms a bridging hydride between Ni^{3+} and Fe^{2+} which is the catalytically active species.[19] Catalysis begins when the hydride (H^-) is transferred to a Ni-bound S-Cys (now Ni^+) and an approaching H_2 is cleaved by Ni^+ *via* oxidative addition, leaving Ni^{3+} with two bound H^-: one terminal and one bridged to Fe^{2+}.[37] This intermediate then undergoes two consecutive PCETs to regenerate the catalytically active bridging hydride Ni^{3+}-H^--Fe^{2+} species.[37] Interestingly, despite the O_2-sensitivity of the [NiFe] active site, a class of membrane-bound [NiFe]-H_2ases can sustain H_2 reactivity in the presence of O_2 due to the unique proximal $[Fe_4S_3]_p$ cluster that can be oxidized once more than the typical $[Fe_4S_4]_p$ cluster and can also be reductively rescued to continue catalysis.[38-39]

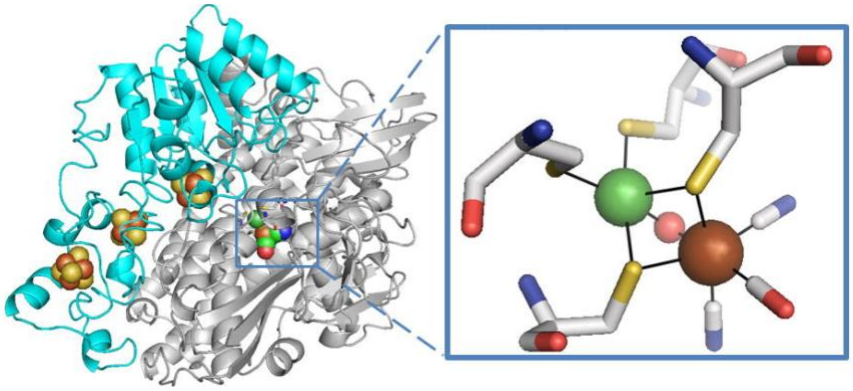

Figure 1.4. Hydrogenase structure (*left*) and active site (*right*) from *Desulfovibrio fructosovorans* (PDB: 1YRQ) at 2.10 Å contains three [FeS] clusters (brown and yellow spheres) in the small (cyan) subunit and the [NiFe] cluster in the large (white) subunit.[40] In this state, a μ-oxo group (red sphere) bridges the two metals, and the Fe possesses a CO and two cyanide ligands. Images from ref 13.[13]

1.3 Ni superoxide dismutase

Discovered in 1996, NiSOD belongs to a family of four SODs categorized by their metal cofactors including MnSOD, FeSOD, and CuZnSOD.[41-43] SODs are postulated to have emerged during the Great Oxidation Event as a cellular defense against oxidative stress/damage from O_2 and other reactive oxygen species (ROS).[44] SODs catalyze the disproportionation of superoxide ($O_2^{\bullet-}$) into oxygen (O_2) and hydrogen peroxide (H_2O_2) *via* a "ping-pong" mechanism; shuttling the redox-active metal center between a one electron reduced and oxidized state (Eq. 1.1-1.3).

$$M^{ox} + O_2^{\bullet-} \rightarrow M^{red} + O_2 \qquad \text{(Eq. 1.1)}$$

$$M^{red} + O_2^{\bullet-} + 2\ H^+ \rightarrow M^{ox} + H_2O_2 \qquad \text{(Eq. 1.2)}$$

$$\text{Overall: } 2O_2^{\bullet-} + 2H^+ \rightarrow O_2 + H_2O_2 \qquad \text{(Eq. 1.3)}$$

Like other redox-active Ni metalloenzymes, NiSOD capitalizes on the electron richness of thiolates to stabilize the high valent Ni^{3+} (M^{ox}) state.[45] As previously established, these enzymes are very sensitive to aerobic environments on account of the high reactivity of S-donors to O_2 and H_2O_2.[46-49] Most interestingly though, NiSOD is apparently insensitive to O_2 as well as other ROS such as $O_2^{\bullet-}$ and H_2O_2. Not only does NiSOD stand out from other Ni metalloenzymes for the *type* of chemistry that it performs, but it also stands out among the other SODs for the *way* it performs SOD chemistry.

NiSOD differs from its SOD family members across all orders of protein structure, from quaternary subunit count and organization down to primary peptide sequence and active site. NiSOD is a homohexamer (78 kDa) of six antiparallel 4-helix bundles arranged into a hollow 60

Å diameter sphere with a 20 Å diameter cavity in the center (Figure 1.5).[50] Each subunit holds one Ni active site at the N-terminus of the peptide strand in a motif called the "nickel hook" (Figure 1.5).[50-51] In the "nickel hook", Ni is bound in the plane by two thiolate S-donors (Cys2 and Cys6) and two N-donors (backbone amide of Cys2 and terminal amine of His1), similar to the N_2S_2 coordination of Ni_d in the A-cluster of ACS (*vide supra*). Unlike Ni_d, however, this active site axially incorporates a third N-donor (Nδ-His1) for an overall square pyramidal geometry and this Ni participates in redox chemistry.[52] Examination of the active site by crystallographic techniques reveals that the coordination environment (specifically axial Nδ-His1 coordination) varies with Ni oxidation state: $Ni^{2+}N_2S_2$ (reduced state of "His-off") and $Ni^{3+}N_3S_2$ (oxidized state or "His-on").[50-51, 53-54]

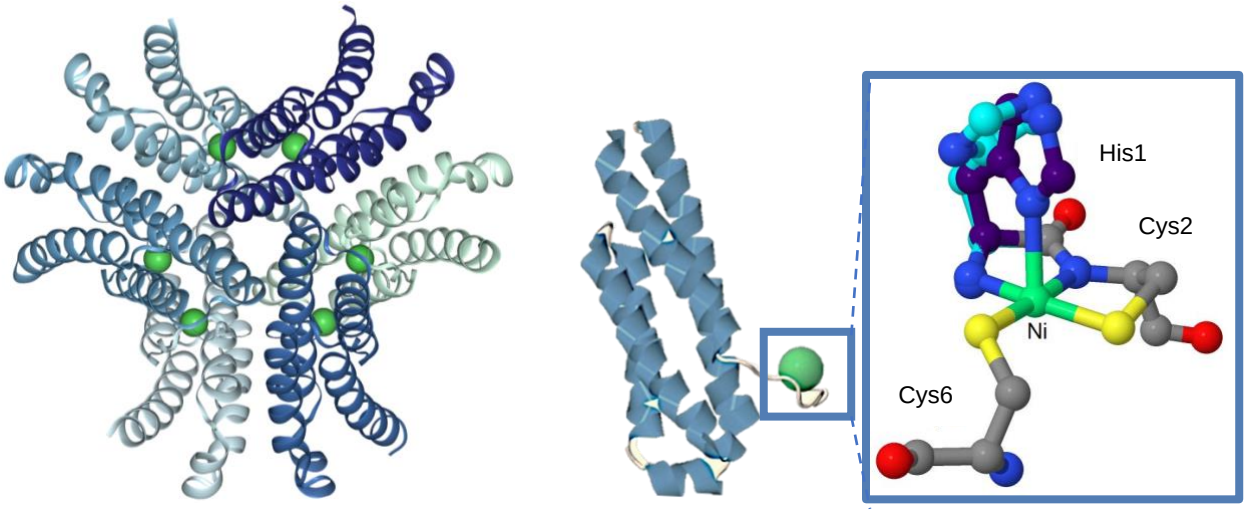

Figure 1.5. The homohexameric structure of NiSOD (*left*) from *S. coelicolor* at 1.30 Å resolution (PDB: 1T6U).[50] Single subunit of NiSOD showing Ni-hook at N-terminus coordinated to nickel ion represented with a green sphere (*middle*). Active site of NiSOD in both oxidation states: His1 residue in cyan represents the structure of the reduced NiSOD active site and His1 residue in violet represents the structure of the oxidized NiSOD active site (*right*) Images generated with Jmol and Pymol.[55]

Despite major differences from other SODs, all SODs are capable of this chemistry on account of their redox potentials (MnSOD, ~0.3 V[56]; FeSOD, ~0.1 V[57]; CuZnSOD, 0.32-0.36 V[58], all V vs NHE) which fall optimally at the midpoint (~0.36 V vs NHE) between the reduction potentials of $O_2/2H^+$ and $O_2^{\bullet-}$ (0.91 V and –0.18 V, respectively vs NHE, pH 7, 25 ºC).[59] Even aquated Fe^{2+} and Cu^+ are capable of catalyzing SOD chemistry as their $Fe^{3+/2+}$ and $Cu^{2+/1+}$ redox couples fall between this range (0.77 V and 0.16 V, respectively, vs NHE, pH 7, 25 ºC).[60] Notably, this is not true of aquated Ni^{2+}, whose $Ni^{3+/2+}$ redox couple falls well outside the $O_2^{\bullet-}$ redox window (2.26 V vs NHE).[61] This highlights the essential role that electron rich S-Cys donors play in depressing the redox potential of NiSOD down to a near-optimal 0.29 V (vs NHE).[53] Remarkably, despite the major structural differences, potentially O_2-susceptible active site, and generally ill-suited metal center, NiSOD is capable of disproportionation chemistry at the same diffusion-limited rate ($k_{cat} \approx 10^9$ M^{-1} s^{-1} per Ni site) as other SODs.[53-54, 62]

1.3.1 Structural and Spectroscopic Properties of NiSOD

One of the first indicators that this newly discovered SOD contains a Ni center responsible for catalytic activity was the detection of a low spin Ni^{3+} rhombic EPR signal: $S = ½$ ($g_x = 2.304$, $g_y = 2.248$, $g_z = 2.012$) that is very similar to that observed in [NiFe]-H_2ase with well resolved triplet hyperfine splitting ($A_{zz} = 24.9$ G) in the g_z component (Figure 1.6).[53, 63] These features indicate that the unpaired electron in oxidized NiSOD resides primarily in the d_{z2} singly-occupied molecular orbital (SOMO) of Ni^{3+} which is axially ligated by a N-donor ($I = 1$). Upon integration of this signal, it is clear that 50% of Ni sites are in the oxidized $Ni^{3+}N_3S_2$ state present in both as-isolated and oxidized NiSOD preparations.[53] This mixture of $Ni^{2+}N_2S_2$ and $Ni^{3+}N_3S_2$ makes characterization of each state challenging. The electronic absorption spectrum of RT NiSOD is

dominated by a S-Cys → Ni^{3+} ligand-to-metal charge transfer (LMCT) band at 372 nm (ε = 6800 M^{-1} cm^{-1}, ~50% v/v glycerol/tris buffer, pH 8.5) from paramagnetic oxidized Ni^{3+} active sites ($NiSOD_{ox}$).[64] MCD spectroscopy enables the weak absorption bands from reduced Ni active sites ($NiSOD_{red}$) to be visualized apart from $Ni90SOD_{ox}$. These features arise from the *d*-manifold of diamagnetic Ni^{2+} as *d-d* absorption bands around 450 and 400 nm (ε = 480 and 500 M^{-1} cm^{-1}, respectively). [64] These *d-d* features closely resemble the absorption spectra of similar planar $Ni^{2+}(N_2S_2)$ synthetic complexes.[48-49, 65-70] These spectral features are illuminated further by computational techniques that calculate the electronic structure of NiSOD's active site. MO calculations reveal the nature of $NiSOD_{red}$'s highest-occupied molecular orbital (HOMO), comprised of Ni-dπ and S/N-pπ MOs that are filled for an overall antibonding HOMO.[64] The high energy of $NiSOD_{red}$'s antibonding HOMO makes oxidation of the site easier while the π-interaction between the Ni-dπ MO and S-pπ MOs discourages S-oxidation such that $NiSOD_{red}$ is poised for facile oxidation of the Ni^{2+} metal center, specifically.

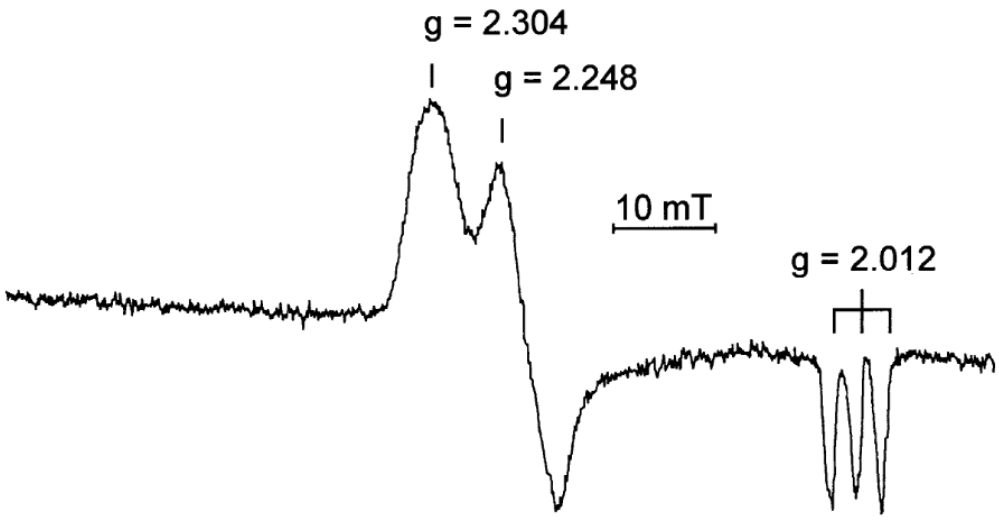

Figure 1.6. X-band EPR spectrum of *Streptomyces coelicolor* NiSOD (approximately 100 μM) dissolved in sodium phosphate buffer, pH 7.4. EPR spectra was obtained at 77 K with a microwave frequency of 9.43 GHz, a microwave power of 1 mW and a modulation amplitude of 1.0 mT. The *g* values are indicated.[63]

1.3.2 NiSOD Questions Remaining

As previously stated, the 1:1 mixture of oxidized and reduced active sites in as-isolated preparations of NiSOD makes characterization of the enzyme challenging, and the mechanism remains unclear. Aside from the broader "ping-pong" mechanism distinction, other mechanistic details of the catalytic cycle of NiSOD are still cloudy including: (i) the role of Ni ligands (namely the role of N_{axial}-His1 ligation), (ii) substrate coordination (inner and/or outer sphere electron transfer mechanism), and (iii) the source of H^+ for the reductive half-reaction.

1.3.2.1 Role of Ni Ligands

The role of Ni-coordinating ligands in NiSOD has been well-established by multiple experimental and theoretical studies of native enzyme and mutated variants. The strongly anionic nature of the thiolate and amidate ligands depresses the $Ni^{3+/2+}$ redox couple into the biological window and most-optimally for both half reactions of superoxide disproportionation.[64, 71-73] The deprotonated amide N-donor from the peptide backbone, a very uncommon feature in metalloenzymes, also alters the electronic structure of the active site such that redox activity remains Ni-based rather than S-based, protecting Cys2 and Cys6 from oxidation.[64] However, NiSOD does not exclusively require anionic ligands; mutagenesis studies reveal the importance of mixed amine/amide ligation. Substitution of the amine-N with a peptide amide-N donor yields a catalytically inactive NiSOD variant with oxidized S-Cys residues, highlighting the role of the amine in the electronic structure of native NiSOD.[71] Site-directed mutagenesis has been used to generate NiSOD variants that substitute Ser for Cys2 and/or Cys6 residues. As expected, these studies reveal that Cys is required for stabilization of the high valent Ni^{3+} state (i.e. catalysis). Also highlighted is the structural role that Cys2 and Cys6 play from primary coordination to quaternary

protein folding.[72-73] A very important feature of the NiSOD coordination sphere is the axially bound Nδ-His1. NiSOD variants that substitute this residue for Glu and Ala lose nearly all catalytic activity and lack the hallmark EPR signal observed in the native enzyme.[74-75] Theoretical calculations also support this observation and emphasize the role of His1 in fine-tuning the redox potential, stabilizing the high valent Ni^{3+} state, and also in the protein structure from the characteristic "Ni hook" to the quaternary structure.[64, 75] The relationship between the position of His1 and Ni oxidation state (on, Ni^{3+}; off, Ni^{2+}) observed in crystal structures of NiSOD have prompted the proposal that His1 changes position during catalysis as Ni shuttles between oxidation states. However, the near-perfect, diffusion-controlled rate of catalysis suggests that this molecular motion is incompatible with such a high rate of reaction. Instead, it is more likely that His1 remains loosely coordinated (2.3-2.6 Å, from the solid-state structure) to Ni in both oxidation states during catalysis and that the $Ni^{2+}N_2S_2$ and $Ni^{3+}N_3S_2$ structures observed in the crystals are inactive and resting states, respectively.[64]

1.3.2.2 Substrate coordination

The half reactions of superoxide disproportionation proceed by inner or outer sphere electron transfer mechanism where Ni binds directly to $O_2^{\bullet-}$ or does not, respectively. Considering that NiSOD performs two different reactions (oxidation and reduction of $O_2^{\bullet-}$), it is also possible that a combination of inner and outer sphere electron transfer takes placed during catalysis. The absence of structural evidence for a Ni–O bond, lack of ionic strength influence on the catalytic rate k_{cat}, and lack of inhibition by azide (N_3^-, a commonly used $O_2^{\bullet-}$ substitute) all support a mechanism lacking direct reaction between the anionic substrate $O_2^{\bullet-}$ and the Ni-center.[53, 62-63] Moreover, the susceptibility of S-donors to oxidation/oxygenation paired with the apparent

insensitivity of NiSOD to O_2 and ROS also supports a mechanism that lacks direct interface between the primary coordination sphere of Ni and substrate/products. However, the vacant coordination site on Ni as well as inhibition of catalytic activity in the presence of CN^- and H_2O_2 suggests that the substrate may interact directly with the Ni center.[63] This vacant site also appears to be "gated" by a Tyr9 that is positioned to control substrate access to this site at just 5.47 Å from Ni.[50, 53, 62] Theoretical calculations of the mechanism further support an inner sphere electron transfer mechanism on account of the electronic structure, specifically the antibonding character, of the HOMO of $NiSOD_{red}$ mentioned previously.[64] This feature encourages oxidation of Ni^{2+} (rather than S-Cys) such that electron transfer could proceed directly from Ni^{2+} to substrate $O_2^{\bullet-}$.[64]

1.3.2.3 Proton Source

Another remaining unknown about NiSOD is the source of the two protons for the one electron, two H^+ process to produce H_2O_2. Bulk solvent was one of the earlier proposals for at least one proton however, this does not appear to be the case due to the independence of k_{cat} on pH.[51, 54, 75-76] This leaves part(s) of the protein itself to be the most likely source of protons. Two peptides at the entrance to the active site have been proposed including the Nζ of Lys64 and Oη of Tyr 9 (the "gateway" Tyr).[50-51] Axially bound His1 has also been proposed however, being positioned on the opposite side of the vacant coordination site of Ni, where substrate is delivered and reacts, makes this an unlikely proton source.[74, 76] A more widely held proposal for the proton source is the thiolate S of Cys2 or Cys6 to form a Ni-thiol during catalysis, much like proposed [NiFe]-H_2ase.[39] Though there is not a consensus on which Cys might ultimately be protonated, support for a Ni–$S^{Cys2/6}$–H species can be found in both computational and experimental works.[64, 76-78] Upon protonation of Cys2 or Cys6, the filled/filled interactions of the Ni-dπ/S-pπ antibonding MOs diminish without

effecting the σ-bonding interactions, causing very minimal changes to active site and actually shortening the Ni-S-Cys bonds.[64] S K-edge XAS data of H_2O_2-reduced $NiSOD_{red}$ is also consistent with a protonated S, providing both computational and experimental support for cysteinate protonation.[78]

1.4 NiSOD Model Complexes

1.4.1 Synthetic Analogue Approach

As discussed in detail above, NiSOD is unusual among Ni-containing enzymes as well as other SOD members, from the quaternary protein structure to the active site coordination (primarily S-Cys), down to the choice of metal center. These distinctive characteristics of NiSOD make it a particularly interesting and challenging case, leaving many questions for the bioinorganic community to answer. The difficulties encountered when studying native NiSOD have led this community to synthesize and study analogues of the enzyme, a method termed the "synthetic analogue approach".[79] This approach essentially isolates the Ni active site to eliminate the complications of the whole protein and better understand the biological structure and function of NiSOD. Analogue complexes vary in size and composition but can be largely split into two groups: (i) peptide-based (including maquettes and short-peptides) and (ii) low molecular weight (LMW) complexes.[80] Peptide-based models include three or more amino acid residues that more or less accurately replicate the NiSOD peptide sequence.[81-102] The distinction between maquette and short-peptide can vary, but generally maquette models are on the larger end of the chain length spectrum. Peptide-based models incorporate secondary coordination sphere effects in NiSOD including H-bonding networks that aid in protein folding and catalysis. Notably, peptide-based model complexes are the only totally structurally faithful and catalytically active models of NiSOD

to date. LMW analogues are smaller complexes comprised of Ni coordinated to a synthesized ligand that structurally and/or functionally mimics NiSOD. These LMW models mimic the primary coordination sphere with varying degrees of structural accuracy and functionality.[103-134] Interestingly, no catalytically-active LMW models are true representations of the NiSOD active site. As such, they do not fully account for the unique structure-function relationship of NiSOD that make it such an exceptional case, nor do they perform at the same diffusion-limited rate. As discussed above, both experimental and computational evidence supports that the structural features at the active site of NiSOD establish the electronic structure essential for the redox chemistry performed the enzyme. These features include the square-planar coordination of Ni by a $N^{amide}N^{amine}S_2^{thiolate}$ donor set with variable axial N^{His} coordination. The following section will focus on structurally accurate LMW models that feature this planar donor set as well as a potential axial N ligand.

1.4.2 NiSOD LMW Analogues

LMW Ni^{2+} complexes with the structurally/electronically accurate set of planar $N^{peptide}N^{amine}S_2^{thiolate}$ donors such as $(Me_4N)[Ni^{II}(BEAAM)]$ (**1**) and $K[Ni(HL2)]$ (**2**) from Shearer and Hegg have been studied and have become the starting point for more structurally accurate models from other groups that follow (Chart 1.1).[103, 118] Masuda and coworkers published $[Ni^{II}(L_{-H})^{-}](ClO_4)$ (**3**) with a similar mixed amide/amine set of N-donors with thioethers rather than thiolates as S-donors.[114] The spectroscopic and structural properties of these models are very similar to one another as well as $NiSOD_{red}$ and are summarized in Tables 1.2 and 1.3 below. Notably, all of these complexes exhibit reversible electrochemistry and upon oxidation of **2** and **3** at –263 ºC and –196 ºC, respectively, exhibit a Ni^{3+} EPR spectrum.

Chart 1.1. 4C LMW NiSOD Model Complexes with Mixed Amine/Amide N-donors

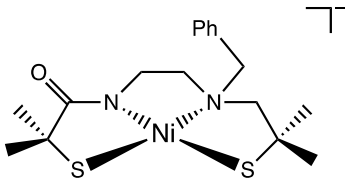

anion of
$Me_4N[Ni(BEAAM)]$
(**1**)

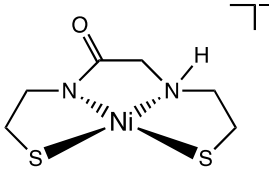

anion of
K[Ni(HL2)]
(**2**)

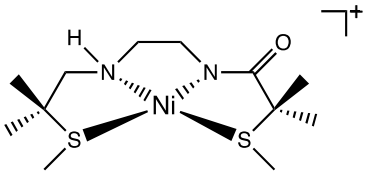

cation of
$[Ni^{II}(L_{-H})^{-}](ClO_4)$
(**3**)

The first LMW model complex to incorporate an axial N-donor in addition to a spatially and electronically accurate set of planar donors is $K[Ni(N_3S_2)]$ (**4**) (where $[N_3S_2]^{3-}$ = deprotonated form of *N*-(2-mercaptoethyl)-2-((2-mercaptoethyl)(pyridin-2-ylmethyl)amino)acetamide) from the Harrop group (Chart 1.2).[120] Structurally, complex **4** is very similar to $NiSOD_{red}$ with the pyridine (py) intended for axial binding of Ni lying far away from the Ni-center ($Ni\text{---}N_{axial}$ = 3.21 Å) not unlike that of $NiSOD_{red}$ ($Ni\text{---}N_{axial}$ = 3.81-4.11 Å) (Table 1.2). Much like $NiSOD_{red}$ and 4C N_2S_2 model complexes, complex **4** displays the hallmark spectroscopic features of double-humped ligand-field electronic absorption bands (449 nm, ε = 230 $M^{-1}cm^{-1}$; 570 nm, ε = 50 $M^{-1}cm^{-1}$ in MeOH) around 450 nm and 550 nm (Table 1.3) and diamagnetism ($S = 0$ by ^1H NMR).[120] Like the native enzyme and peptide-based models, **4** is also water-soluble.[80, 121] Irreversible electrochemistry of **4** and disulfide formation upon one-electron oxidation of **4** reveal that the MO (RAMO) of **4** is not Ni-based as is the case in $NiSOD_{red}$. Specifically, due to the *trans* effect, the thiolate that is *trans* to the carboxamide-N is oxidized to a thiyl radical, is labilized, and replaced by the fifth coordinate py N-donor to form a $Ni^{2+}N_3S$ thiyl radical species which then reacts with another equivalent to form a disulfide bond between two $Ni^{2+}N_3S$ species forming complex **5**, exclusively (Scheme 1.1). To prevent or slow this S-based reactivity, low temperature oxidation of **4** was conducted and monitored by EPR which shows an anisotropic signal (g = [2.26, 2.17,

~2.00]) similar to that of $NiSOD_{ox}$ (Figure 1.2) and indicates a resonance between Ni^{3+}-thiolate ↔ Ni^{2+}-thiol species.

Chart 1.2. Structurally/Electronically Accurate LMW NiSOD Model Complexes with Mixed Amine/Amide N-donors, Thiolate S-donors and Axial N-donor.[a]

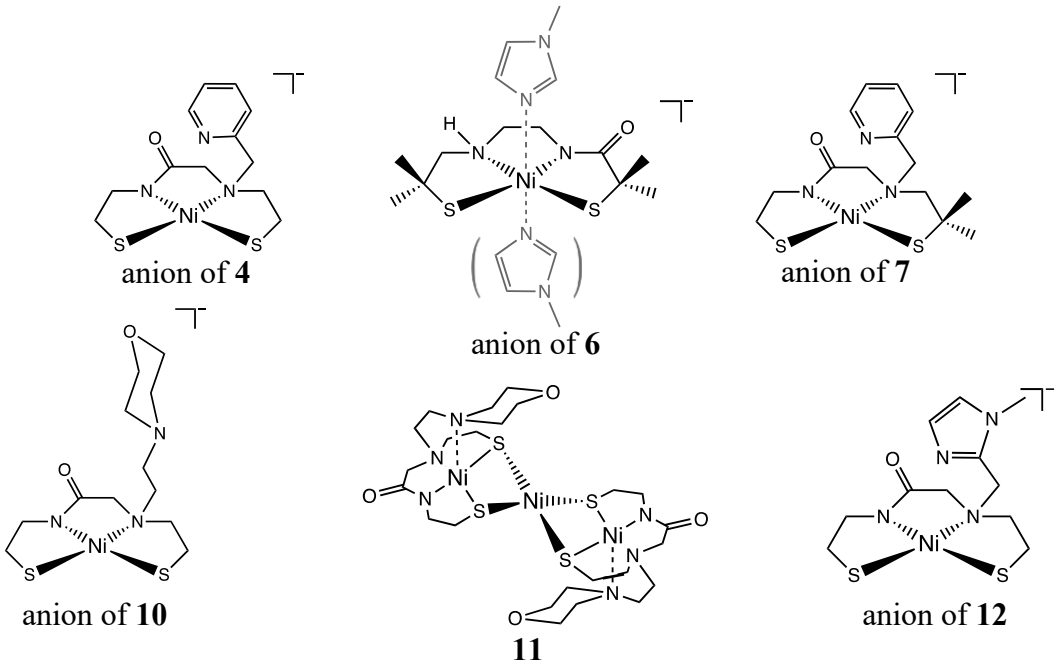

[a]Axial N-donor (shown in gray) not part of **6** ligand frame but added as free ligand during reactivity studies.

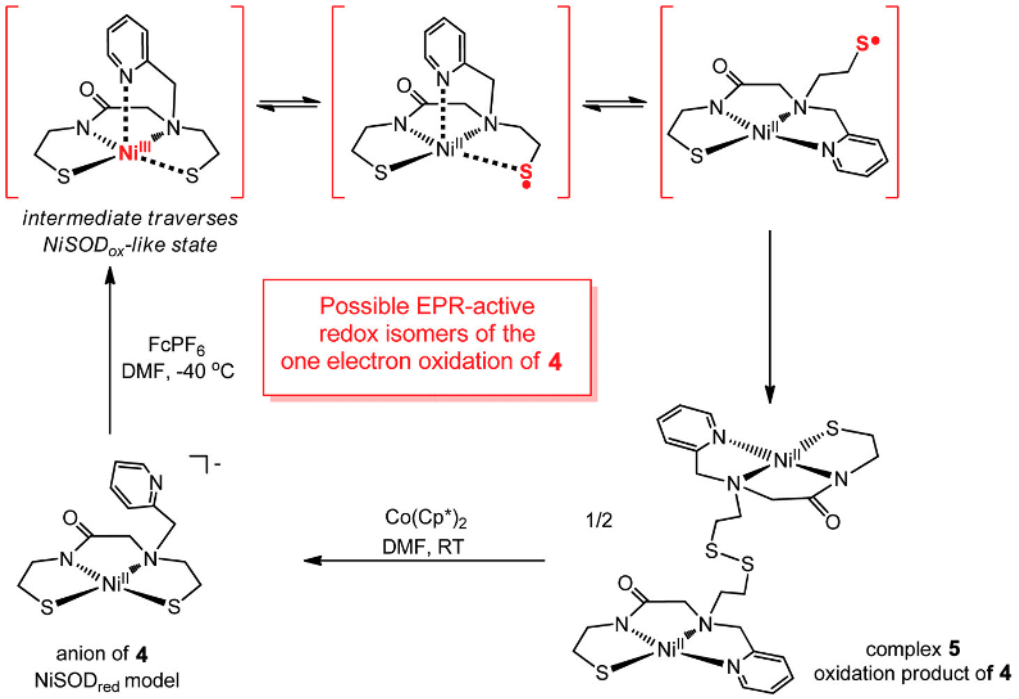

Scheme 1.1. Proposed Mechanism of the Oxidative Conversion of NiSOD$_{red}$ Model Complex **4** to Disulfide-Linked Complex **5**. This figure was adapted from ref 77.

In 2014, Masuda published a 4C $[Ni^{2+}(N_2S_2)]^-$ complex, Na[Ni(L_1)] (**6**) (where L_1 = deprotonated form of 2-mercapto-*N*-(2-((2-mercapto-2-methylpropyl)amino)ethyl)-2-methylpropanamide) (Chart 1.2).[126] This complex does not feature an axial N-donor constructed onto the ligand frame but studies of **6** were conducted in the presence of imidazole and monitored by low temperature UV-vis and EPR spectroscopies. When **6** is oxidized in the presence of imidazole at –60 ºC and –196 ºC, the absorption and EPR spectra, respectively, exhibit characteristic features of NiSOD$_{ox}$ including a new intense absorption band (393 nm, ε = 6200 $M^{-1}cm^{-1}$; 575 nm, ε = 2100 $M^{-1}cm^{-1}$) and rhombic EPR signal (g_x = 2.31, g_y = 2.26, g_z = 2.01) with triplet hyperfine splitting on the g_z tensor ($|A|$ = 2.5 mT) indicating an axially N-bound Ni^{3+} complex. EPR and UV-vis spectra of further low temperature reactivity studies of **6** in the presence

of 1-methylimidazole with superoxide has been interpreted as a N_2S_2-Ni^{2+}-superoxo intermediate however, neither this species nor the oxidized product(s) have been isolated.

To discourage the S-based reactivity observed in **4**, the second generation of complex from the Harrop group was designed with a more sterically robust thiolate, much like that of complex **1** from Shearer that exhibits reversible electrochemistry and even produces a new short-lived purple/blue species upon one-electron oxidation.[103] Discussed above, upon oxidation of **4**, the thiolate *trans* to the carboxamide reacts to form a disulfide-linked complex (**5**). Therefore, *geminal*-methyl groups were added to the carbon α to this S to provide steric bulk for $Na[Ni(N_3S_2^{Me2})]$ (**7**) (where $[N_3S_2^{Me2}]^{3-}$ = the deprotonated form of 2-((2-mercapto-2-methylpropyl)(pyridin-2- ylmethyl)amino)-*N*-(2-mercaptoethyl)acetamide) (Chart 1.2).[131] Like **4**, complex **7** is very structurally similar to $NiSOD_{red}$ with a distant Ni---N_{axial} length of 3.23 Å. Despite the added steric bulk, complex **7** exhibits irreversible electrochemistry and similar oxidation products, indicating a primarily S-based RAMO which is confirmed by computational studies. The primary oxidation product of **7** is the rearranged, disulfide-linked bimetallic species (**8)** (analogous to **5**) as well as minor amounts of a thiazolidine complex (**9**), a two-electron oxidized, monometallic rearrangement product (Scheme 1.2). Altogether, these results suggests that the addition of steric bulk does not ensure primarily Ni-based reactivity but does in fact prevent disulfide formation and opens up new reaction pathways. This observation draws attention toward the role of the axial N-donor that is known to be essential for stabilizing high valent Ni^{3+} and redox tuning of the active site of NiSOD (*vide supra*).

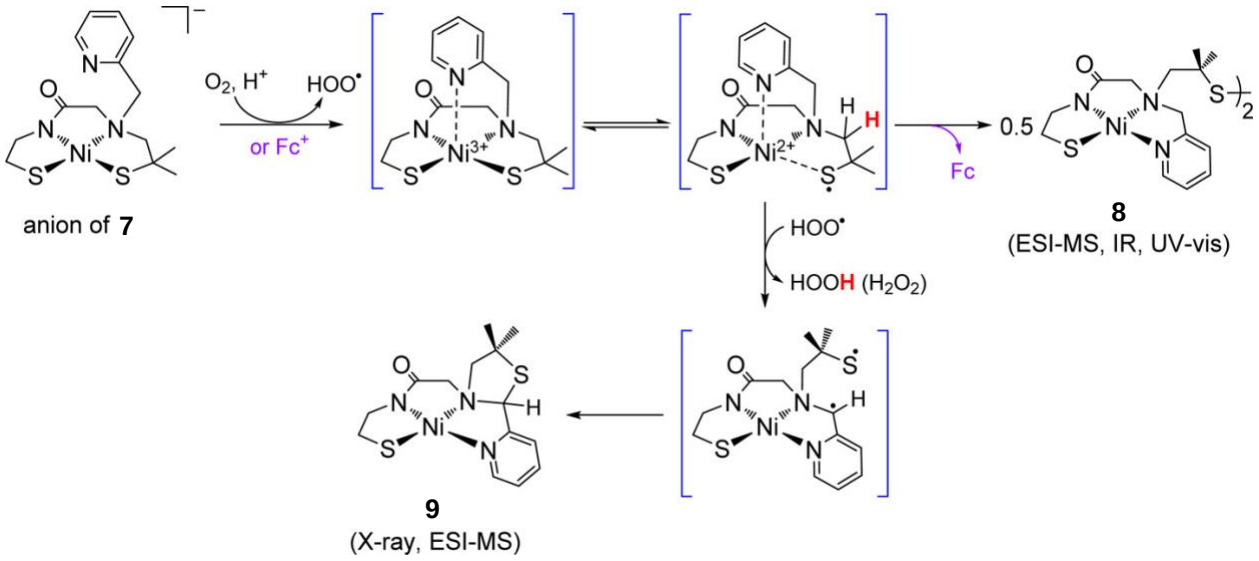

Scheme 1.2. Proposed Mechanism of the Oxidative Conversion of $NiSOD_{red}$ Model Complex **7** to Disulfide-Linked Complex **8** and Thiazolidine Complex **9**. This figure was adapted from ref 85.

In 2021, the Harrop group submitted its third generation of NiSOD model complex for publication: Na[Ni($N_3S_2^{NEM}$)] (**10**) (where $[N_3S_2^{NEM}]^{3-}$ = the deprotonated form of *N*-(2-mercaptoethyl)-2-((2-mercaptoethyl)(2-morpholinoethyl)amino)-acetamide).[135] Understanding the unstable nature of Ni^{3+} and essential role of the axially bound Nδ-His1 in the native enzyme, complex **10** was designed to assess the role of axial N-donor basicity by incorporating N-ethylmorpholine (NEM), a ~250-fold more Lewis basic axial N-donor than py from **4** and **7** (pK_a = 15.68 for N-ethylmorpholine[136]; pK_a = 13.28 for 2-methylpyridine[137]; both in MeCN). The hypothesis being that enhancing the Lewis basicity of the axial N-donor will encourage 5C square-pyramidal geometry for both Ni^{2+} and Ni^{3+} oxidation states, donating significant electron density from the axial ligand to the Ni center. This would reduce the S-based component of the RAMO (observed in previously described 4C NiSOD models) and prime the electronic structure of **10** for catalytic SOD activity. Again, the structural, electrochemical, and electronic feature of **10** closely resemble that of prior generations with a long Ni---N_{axial} distance (4.50 Å), irreversible electrochemistry, and a significantly S-based RAMOs. However, the reactivity of **10** differs

greatly. Upon oxidation, a new trimetallic, "stair-step" species (**11**) is formed, consisting of two units of **10** joined by an additional Ni^{2+} ion at the S donors (two from each unit of **10**) in a square-planar geometry (Chart 1.2, Scheme 1.3). Interestingly, the resulting geometry of the two terminal Ni centers are now 5C square pyramidal with a long Ni---N_{axial} distance of ~2.6 Å, which now falls within the range of observed distances of $NiSOD_{ox}$ (Ni---Nδ-His1 = ~2.3-2.6 Å)[50-51] and computed distances for His-on/low-spin Ni^{2+}-SOD.[108] Additionally, **11** exhibits reversible and quasireversible electrochemistry, a significantly less S-based HOMO (23.0% S-pπ in **10**; 8% S-pπ in **11**), as well as SOD-like reactivity with $O_2^{\bullet-}$ when assayed in nonaqueous conditions. These results support earlier findings that the Ni---Nδ-His1 bond is essential for active site assembly and catalysis and supports hypotheses that Ni in NiSOD remains 5C throughout catalysis and that the coordinated S-Cys are possible H^+ shuttles during catalysis.

Scheme 1.3. Reactivity of **10:** Oxidative (*top, middle*) and Direct (*bottom*) Synthetic Conditions that Convert **10** to **11**.

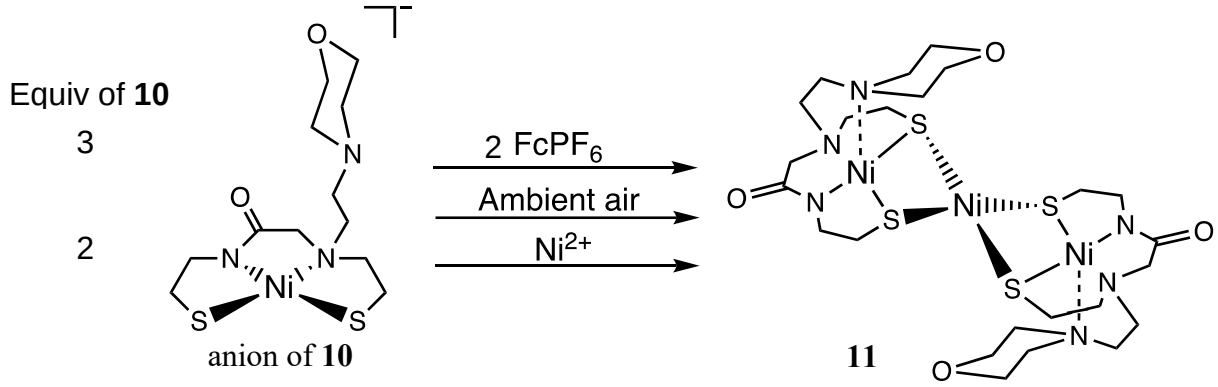

Table 1.2. Select Bond Distances (Å) for $NiSOD_{red}$ (PDB code) and Select NiSOD Models[a].

NiSOD and Models	Ni–N_{amide}	Ni–N_{amine}	Ni–$S_{trans\text{-}amide}$	Ni–S	Ni---N_{axial}	ref
$NiSOD_{red}$ (1T6U)	1.91	1.87	2.19	2.16	4.11[b]	50
$NiSOD_{red}$ (1Q0K)	1.99	2.17	2.29	2.30	3.81	51
Me_4N[Ni(BEAAM)] (**1**)	1.858	1.989	2.177	2.137	N/A	103
K[Ni(HL2)] (**2**)	1.862	1.937	2.1711	2.1671	N/A	118
$[Ni^{II}(L_{-H})^{-}](ClO_4)$ (**3**)	1.845	1.909	2.1692	2.1772	undetermined	114
K[Ni(N_3S_2)] (**4**)	1.8565	1.954	2.181	2.174	~3.21	120
Na[Ni(L_1)] (**6**)	1.865	1.923	2.1702	2.1450	N/A	126
Na[Ni($N_3S_2^{Me2}$)] (**7**)	1.856	1.937	2.1819	2.1582	~3.23	131
Na[Ni($N_3S_2^{NEM}$) (**10**)	1.8644	1.9556	2.1743	2.1707	~4.50	135
[[Ni($N_3S_2^{NEM}$)]$_2$Ni] (**11**)	1.8553	1.9577	2.1570	2.1653	~2.593	135

[a]Abbreviation: TW = this work. [b]This value represents the average of the Ni-His1-δN separation in the active sites of NiSOD in the reduced (His-off) state; standard deviation is 0.15 Å. [c]From nonmethylated-N to Ni^{2+}.

Table 1.3. UV-vis Data of NiSOD and Select NiSOD Models[a].

NiSOD and Models	λ (nm) (ε (M^{-1} cm^{-1}))[b]	*E* (V vs. Fc^+/Fc)[c]	ref
$NiSOD_{red}$	450 (480), 543 (150)[f]	$E_{½}$: 0.290 V (vs. NHE)[d], $E_{½}$: –0.340[e]	53,64
Me_4N[Ni(BEAAM)] (**1**)	461 (290), 556 sh (70)[g]	$E_{½}$: –0.330[g]	103
K[Ni(HL2)] (**2**)	449 (340), 570 sh (~70)	E_{ox}: –0.458	118
$[Ni^{II}(L_{-H})^{-}](ClO_4)$ (**3**)	436 (390)[h]	$E_{½}$: –1.76; $E_{½}$: 0.63[h]	114
K[Ni(N_3S_2)] (**4**)	449 (320), 570 sh (90)	E_{ox}: –0.620, E_{red}: –1.84	120
Na[Ni(L_1)] (**6**)	441 (258)	$E_{½}$: –0.593; $E_{½}$: –0.570[g]	126
Na[Ni($N_3S_2^{Me2}$)] (**7**)	459 (250), 557 sh (75)	E_{ox}: –0.670, E_{red}: –1.98	131
Na[Ni($N_3S_2^{NEM}$) (**10**)	455 (240), 575 sh (65)	E_{ox}: –0.40, E_{red}: –1.49	135
[[Ni($N_3S_2^{NEM}$)]$_2$Ni] (**11**)	448 (3300), 550 sh (2260), 688 sh (1100)	$E_{½}$: –1.56; $E_{½}$: 0.07; $E_{½}$[j]: 0.21[i]	135

[a]Abbreviations: sh = shoulder; TW = this work. [b]UV–vis spectra reported for MeOH solutions unless otherwise stated. [c]Data represents the redox potential as reported versus the ferrocenium/ferrocene (Fc^+/Fc) couple in DMF unless otherwise stated. [d]Potassium phosphate buffer (pH 7.5). [e]Redox potential normalized to *E* vs. Fc^+/Fc based on information found in ref. 138: [*E* vs. Fc+/Fc = *E* vs. NHE – 0.630 V].[138] [f]Aqueous buffer. [g]MeCN. [h]Acetone. [i]CH_2Cl_2. [j]quasi-reversible couple.

1.5 Research Objectives and Purpose

Since its incorporation into biological systems, Ni has played an essential role in global C, H, N, and O cycles as the center of catalytic activity in redox-active Ni-containing enzymes. Despite their early and oxygen-free origins, these enzymes perform a wide variety of chemistry relevant to the energetic (H_2, CH_4), physiological ($O_2^{\bullet-}$), and environmental (CH_4, CO, CO_2) issues we face today. For this reason, it is of great interest to better understand the features of these enzymes that afford such functional variety and efficiency. Essential to the function of these enzymes is not only Ni, but specifically, Ni-S-Cys coordination which can be found in each redox-active Ni-enzyme. A particularly notable member of this group is NiSOD which catalyzes disproportionation of ROS despite its oxygen-sensitive S-rich coordination environment and a metal with a redox potential far outside the redox window for SOD chemistry in its aquated state. The goal of this research is to establish the fundamentals of NiSOD catalysis, and biocatalytic Ni redox activity in general, using a synthetic analogue approach to synthesize, characterize, and assess the properties of structurally and electronically accurate models of NiSOD in order to elucidate its mechanism and contribute to the broader field of biologically-relevant Ni-thiolate redox chemistry.

Prior work from our group (*vide supra*) has produced three generations of NiSOD model complexes, which have emphasized the structure-function role of sterically bulky thiolates, Lewis basicity of the axial N-donor, engagement of thiolate-S groups with a Lewis acid species, and coordination geometry during turnover. Together, these aspects lower the S-contribution to the RAMO thereby enhancing the Ni-contribution to the electronic structure of each model, tuning the RAMO for Ni-based electrochemistry. However, these complexes still exhibit largely S-based reactivity.

In the following chapter (Ch. 2), a fourth-generation complex is reported and includes not only a structurally and electronically accurate basal set of donors, but also an axial N-donor using 1-methylimidazole (NMeIm). This complex (**12**) is the first NiSOD model complex to feature an axial N-donor that is electronically and structurally faithful to that of the His1 in the native enzyme. It is expected that the basicity of NMeIm (greater than pK_a of imidazole = 15.07 in MeCN)[137] being similar to NEM and greater than py, coupled with the π-accepting ability of NMeIm, which is present in py but absent in NEM will produce a 5C square pyramidal geometry without the need to modify the thiolates as in **10**. The stronger field nature of NMeIm should promote the low-spin state Ni^{2+} to result in a 5C Ni^{2+} with a long Ni---N_{axial} as in **10**. Because the electronic structure of low-spin 5C Ni^{2+} is primarily d_{z2}-based[64], we anticipate a model that is poised for functionality and given that all electrochemical prerequisites are met. The synthesis, characterization, and reactivity studies on **12** are reported in Ch. 2.

Past and future synthetic model complexes from our group have and will contribute a greater understanding to the bioinorganic community on the role of the coordination environment, requirements for Ni-based redox-activity, and answer questions remaining about the mechanism of NiSOD. More broadly, this work will also provide further insight into the structure-function relationships employed by the larger family of Ni-thiolate redox-active enzymes.

1.6 References

1. Bartow, V., Axel Fredrick Cronstedt. *J. Chem. Educ.* **1953,** *30*, 247-252.

2. Cronstedt, A. F., Rön och försök, Gjorde Med en Malm-art från Los Kobolt Grufvor i Farila Socken och Helsingeland. *K. Sven. vetensk.akd. handl.* **1751,** *12*, **287-292**.

3. Enghag, P., Nickel. In *Encyclopedia of the Elements*, Wiley-VCH Verlag GmbH & Co. KGaA: 2004; pp 685-706.

4. Bertini, I.; Gray, H. B.; Valentine, J. S.; Stiefel, E. I., *Biological Inorganic Chemistry: Structure and Reactivity*. University Science Books: 2007; p 739.

5. Rothman, D. H.; Fournier, G. P.; French, K. L.; Alm, E. J.; Boyle, E. A.; Cao, C.; Summons, R. E., Methanogenic burst in the end-Permian carbon cycle. *Proc. Natl. Acad. Sci. U. S. A.* **2014,** *111*, 5462-5467.

6. Reichow, M. K.; Pringle, M. S.; Al'Mukhamedov, A. I.; Allen, M. B.; Andreichev, V. L.; Buslov, M. M.; Davies, C. E.; Fedoseev, G. S.; Fitton, J. G.; Inger, S.; Medvedev, A. Y.; Mitchell, C.; Puchkov, V. N.; Safonova, I. Y.; Scott, R. A.; Saunders, A. D., The timing and extent of the eruption of the Siberian Traps large igneous province: Implications for the end-Permian environmental crisis. *Earth. Planet. Sci. Lett.* **2009,** *277*, 9-20.

7. C.L. Coyle, E. I. S., The Bioinorganic Chemistry of Nickel. Lancaster, J. R., Ed. VCH: New York, N.Y. :, 1988; p 3.

8. Konhauser, K. O.; Pecoits, E.; Lalonde, S. V.; Papineau, D.; Nisbet, E. G.; Barley, M. E.; Arndt, N. T.; Zahnle, K.; Kamber, B. S., Oceanic nickel depletion and a methanogen famine before the Great Oxidation Event. *Nature* **2009,** *458*, 750-753.

9. Liu, Y.; Beer, L. L.; Whitman, W. B., Methanogens: a window into ancient sulfur metabolism. *Trends Microbiol.* **2012,** *20*, 251-258.

10. Weiss, M. C.; Sousa, F. L.; Mrnjavac, N.; Neukirchen, S.; Roettger, M.; Nelson-Sathi, S.; Martin, W. F., The physiology and habitat of the last universal common ancestor. *Nat. Microbiol.* **2016,** *1*, 1-8.

11. Baross, J. A.; Hoffman, S. E., Submarine hydrothermal vents and associated gradient environments as sites for the origin and evolution of life. *Origins Life Evol. Biosphere* **1985,** *15*, 327-345.

12. Martin, W.; Russell, M. J., On the origin of biochemistry at an alkaline hydrothermal vent. *Philos. T. Roy. Soc. B.* **2007,** *362*, 1887-1926.

13. Scott B. Mulrooney, R. P. H., Nickel Uptake and Utilization by Microorganisms. *FEMS Microbiol. Rev.* **2003,** *27*, 239-261.

14. Boer, J. L.; Mulrooney, S. B.; Hausinger, R. P., Nickel-dependent metalloenzymes. *Arch. Biochem. Biophys.* **2014,** *544*, 142-152.

15. Ragsdale, S. W., Nickel-based Enzyme Systems. *J. Biol. Chem.* **2009,** *284*, 18571-18575.

16. Desguin, B.; Goffin, P.; Viaene, E.; Kleerebezem, M.; Martin-Diaconescu, V.; Maroney, M. J.; Declercq, J.-P.; Soumillion, P.; Hols, P., Lactate racemase is a nickel-dependent enzyme activated by a widespread maturation system. *Nat. Commun.* **2014,** *5*, 1-12.

17. Ju, T.; Goldsmith, R. B.; Chai, S. C.; Maroney, M. J.; Pochapsky, S. S.; Pochapsky, T. C., One Protein, Two Enzymes Revisited: A Structural Entropy Switch Interconverts the Two Isoforms of Acireductone Dioxygenase. *J. Mol. Biol.* **2006,** *363*, 823-834.

18. Dai, Y.; Pochapsky, T. C.; Abeles, R. H., Mechanistic Studies of Two Dioxygenases in the Methionine Salvage Pathway of Klebsiella pneumoniae. *Biochemistry* **2001,** *40*, 6379-6387.

19. Sigel, A.; Sigel, H.; Sigel, R. K. O., *Nickel and Its Surprising Impact in Nature*. Wiley: 2007; Vol. 5, p 35-491.

20. Rankin, J. A.; Mauban, R. C.; Fellner, M.; Desguin, B.; McCracken, J.; Hu, J.; Varganov, S. A.; Hausinger, R. P., Lactate Racemase Nickel-Pincer Cofactor Operates by a Proton-Coupled Hydride Transfer Mechanism. *Biochemistry* **2018,** *57*, 3244-3251.

21. Scheller, S.; Goenrich, M.; Boecher, R.; Thauer, R. K.; Jaun, B., The key nickel enzyme of methanogenesis catalyses the anaerobic oxidation of methane. *Nature* **2010,** *465*, 606-608.

22. Grabarse, W.; Mahlert, F.; Duin, E. C.; Goubeaud, M.; Shima, S.; Thauer, R. K.; Lamzin, V.; Ermler, U., On the mechanism of biological methane formation: structural evidence for

conformational changes in methyl-coenzyme M reductase upon substrate binding. *J. Mol. Biol.* **2001,** *309*, 315-330.

23. Grabarse, W.; Mahlert, F.; Shima, S.; Thauer, R. K.; Ermler, U., Comparison of three methyl-coenzyme M reductases from phylogenetically distant organisms: unusual amino acid modification, conservation and adaptation. *J. Mol. Biol.* **2000,** *303*, 329-344.

24. Kadish, K. M.; Guilard, R.; Smith, K. M.; Ragsdale, S. W., *The The Porphyrin Handbook: Bioinorganic and Bioorganic Chemistry* World Scientific Publishing Company: 2012; Vol. 11.

25. Ermler, U.; Grabarse, W.; Shima, S.; Goubeaud, M.; Thauer, R. K., Crystal Structure of Methyl-Coenzyme M Reductase: The Key Enzyme of Biological Methane Formation. *Science* **1997,** *278*, 1457-1462.

26. Can, M.; Armstrong, F. A.; Ragsdale, S. W., Structure, Function, and Mechanism of the Nickel Metalloenzymes, CO Dehydrogenase, and Acetyl-CoA Synthase. *Chem. Rev.* **2014,** *114*, 4149-4174.

27. Newsome, D. S., The Water-Gas Shift Reaction. *Cataly. Rev.* **1980,** *21*, 275-318.

28. Ragsdale, S. W.; Pierce, E., Acetogenesis and the Wood–Ljungdahl pathway of CO_2 fixation. *BBA - Proteins Proteom.* **2008,** *1784*, 1873-1898.

29. Amara, P.; Mouesca, J.-M.; Volbeda, A.; Fontecilla-Camps, J. C., Carbon Monoxide Dehydrogenase Reaction Mechanism: A Likely Case of Abnormal CO_2 Insertion to a $Ni{-}H^-$ Bond. *Inorg. Chem.* **2011,** *50*, 1868-1878.

30. Jeoung, J.-H.; Dobbek, H., Carbon Dioxide Activation at the Ni,Fe-Cluster of Anaerobic Carbon Monoxide Dehydrogenase. *Science* **2007,** *318*, 1461-1464.

31. Fuchs, G., Alternative Pathways of Carbon Dioxide Fixation: Insights into the Early Evolution of Life? *Annu. Rev. Microbiol.* **2011,** *65*, 631-658.

32. Doukov, T. I.; Blasiak, L. C.; Seravalli, J.; Ragsdale, S. W.; Drennan, C. L., Xenon in and at the End of the Tunnel of Bifunctional Carbon Monoxide Dehydrogenase/Acetyl-CoA Synthase. *Biochemistry* **2008,** *47*, 3474-3483.

33. Lindahl, P. A., Acetyl-coenzyme A synthase: the case for a Ni_p^0-based mechanism of catalysis. *J. Biol. Inorg. Chem.* **2004,** *9*, 516-524.

34. Ragsdale, S. W., Metals and Their Scaffolds To Promote Difficult Enzymatic Reactions. *Chem. Rev.* **2006,** *106*, 3317-3337.

35. Vignais, P. M.; Billoud, B.; Meyer, J., Classification and phylogeny of hydrogenases. *FEMS Microbiol. Rev.* **2001,** *25*, 455-501.

36. Montet, Y.; Amara, P.; Volbeda, A.; Vernede, X.; Hatchikian, E. C.; Field, M. J.; Frey, M.; Fontecilla-Camps, J. C., Gas access to the active site of Ni-Fe hydrogenases probed by X-ray crystallography and molecular dynamics. *Nat. Struct. Biol.* **1997,** *4*, 523-526.

37. Lill, S. O. N.; Siegbahn, P. E. M., An Autocatalytic Mechanism for NiFe-Hydrogenase: Reduction to Ni(I) Followed by Oxidative Addition. *Biochemistry* **2009,** *48*, 1056-1066.

38. Volbeda, A.; Darnault, C.; Parkin, A.; Sargent, F.; Fraser; Juan, Crystal Structure of the O_2 -Tolerant Membrane-Bound Hydrogenase 1 from *Escherichia coli* in Complex with Its Cognate Cytochrome b. *Structure* **2013,** *21*, 184-190.

39. Ogata, H.; Lubitz, W.; Higuchi, Y., Structure and function of [NiFe] hydrogenases. *J. Biochem.* **2016,** *160*, 251-258.

40. Volbeda, A.; Martin, L.; Cavazza, C.; Matho, M.; Faber, B. W.; Roseboom, W.; Albracht, S. P. J.; Garcin, E.; Rousset, M.; Fontecilla-Camps, J. C., Structural differences between the ready and unready oxidized states of [NiFe] hydrogenases. *J. Biol. Inorg. Chem.* **2005,** *10*, 239-249.

41. McCord, J. M.; Fridovich, I., Superoxide Dismutase. *J. Biol. Chem.* **1969,** *244*, 6049-6055.

42. Keele, B. B.; McCord, J. M.; Fridovich, I., Superoxide Dismutase from *Escherichia coli* B. *J. Biol. Chem.* **1970,** *245*, 6176-6181.

43. Yost, F. J.; Fridovich, I., An Iron-containing Superoxide Dismutase from *Escherichia coli*. *J. Biol. Chem.* **1973,** *248*, 4905-4908.

44. Fridovich, I.; Poole, L. B.; Holmgren, A.; Lou, M. F.; Gladyshev, V. N.; David, S. S.; Osborne, R. L.; Dawson, J. H.; Copley, S. D.; Kadokura, H.; Beckwith, J.; Gilbert, H. F.; Ragsdale, S. W., Antioxidant Enzymes. In *Redox Biochemistry*, John Wiley & Sons, Inc.: 2008; pp 49-134.

45. Maroney, M. J., Structure/function relationships in nickel metallobiochemistry. *Curr. Opin. Chem. Biol.* **1999,** *3*, 188-199.

46. Grapperhaus, C. A.; Darensbourg, M. Y., Oxygen Capture by Sulfur in Nickel Thiolates. *Acc. Chem. Res.* **1998,** *31*, 451-459.

47. Mirza, S. A.; Pressler, M. A.; Kumar, M.; Day, R. O.; Maroney, M. J., Oxidation of nickel thiolate ligands by dioxygen. *Inorg. Chem.* **1993,** *32*, 977-987.

48. Maroney, M. J.; Choudhury, S. B.; Bryngelson, P. A.; Mirza, S. A.; Sherrod, M. J., Theoretical Study of the Oxidation of Nickel Thiolate Complexes by O_2. *Inorg. Chem.* **1996,** *35*, 1073-1076.

49. Kumar, M.; Day, R. O.; Colpas, G. J.; Maroney, M. J., Ligand oxidation in a nickel thiolate complex. *J. Am. Chem. Soc.* **1989,** *111*, 5974-5976.

50. Barondeau, D. P.; Kassmann, C. J.; Bruns, C. K.; Tainer, J. A.; Getzoff, E. D., Nickel superoxide dismutase structure and mechanism. *Biochemistry* **2004,** *43*, 8038-8047.

51. Wuerges, J.; Lee, J.-W.; Yim, Y.-I.; Yim, H.-S.; Kang, S.-O.; Carugo, K. D., Crystal structure of nickel-containing superoxide dismutase reveals another type of active site. *Proc. Natl. Acad. Sci. U. S. A.* **2004,** *101*, 8569-8574.

52. Matysik, J.; Schulten, E.; Alia, A.; Gast, P.; Raap, J.; Lugtenburg, J.; Hoff, A. J.; Groot, H. J. M. D., Photo-CIDNP ^{13}C Magic Angle Spinning NMR on Bacterial Reaction Centres: Exploring the Electronic Structure of the Special Pair and Its Surroundings. *Biol. Chem.* **2001,** *382*, 1271-1276.

53. Herbst, R. W.; Guce, A.; Bryngelson, P. A.; Higgins, K. A.; Ryan, K. C.; Cabelli, D. E.; Garman, S. C.; Maroney, M. J., Role of conserved tyrosine residues in NiSOD catalysis: a case of convergent evolution. *Biochemistry* **2009,** *48*, 3354-3369.

54. Choudhury, S. B.; Lee, J.-W.; Davidson, G.; Yim, Y.-I.; Bose, K.; Sharma, M. L.; Kang, S.-O.; Cabelli, D. E.; Maroney, M. J., Examination of the Nickel Site Structure and Reaction Mechanism inStreptomycesseoulensisSuperoxide Dismutase. *Biochemistry* **1999,** *38*, 3744-3752.

55. Rose, A. S.; Bradley, A. R.; Valasatava, Y.; Duarte, J. M.; Prlić, A.; Rose, P. W., NGL viewer: web-based molecular graphics for large complexes. *Bioinformatics* **2018,** *34*, 3755-3758.

56. Vance, C. K.; Miller, A.-F., Novel Insights into the Basis for *Escherichia coli* Superoxide Dismutase's Metal Ion Specificity from Mn-Substituted FeSOD and Its Very High E_m. *Biochemistry* **2001,** *40*, 13079-13087.

57. Yikilmaz, E.; Rodgers, D. W.; Miller, A.-F., The Crucial Importance of Chemistry in the Structure−Function Link: Manipulating Hydrogen Bonding in Iron-Containing Superoxide Dismutase. *Biochemistry* **2006,** *45*, 1151-1161.

58. Azab, H. A.; Banci, L.; Borsari, M.; Luchinat, C.; Sola, M.; Viezzoli, M. S., Redox chemistry of superoxide dismutase. Cyclic voltammetry of wild-type enzymes and mutants on functionally relevant residues. *Inorg. Chem.* **1992,** *31*, 4649-4655.

59. Koppenol, W. H.; Stanbury, D. M.; Bounds, P. L., Electrode potentials of partially reduced oxygen species, from dioxygen to water. *Free Radical Biol. Med.* **2010,** *49*, 317-322.

60. Bertocci, U.; Wagman, D. D.; Heusler, K. E.; Lorenz, W. J., *Standard Potentials in Aqueous Solution* 1st ed. ed.; New York : M. Dekker: New York, 1985.

61. Zilbermann, I.; Maimon, E.; Cohen, H.; Meyerstein, D., Redox Chemistry of Nickel Complexes in Aqueous Solutions. *Chem. Rev.* **2005,** *105*, 2609-2626.

62. Sheng, Y.; Abreu, I. A.; Cabelli, D. E.; Maroney, M. J.; Miller, A.-F.; Teixeira, M.; Valentine, J. S., Superoxide Dismutases and Superoxide Reductases. *Chem. Rev.* **2014,** *114*, 3854-3918.

63. Youn, H.-D.; Kim, E.-J.; Roe, J.-H.; Hah, Y. C.; Kang, S.-O., A novel nickel-containing superoxide dismutase from *Streptomyces* spp. *Biochem. J.* **1996,** *318*, 889-896.

64. Fiedler, A. T.; Bryngelson, P. A.; Maroney, M. J.; Brunold, T. C., Spectroscopic and Computational Studies of Ni Superoxide Dismutase: Electronic Structure Contributions to Enzymatic Function. *J. Am. Chem. Soc.* **2005,** *127*, 5449-5462.

65. Mills, D. K.; Reibenspies, J. H.; Darensbourg, M. Y., Sterically Protected Nickel(II) in a N_2S_2 Donor Environment: 1,5-bis(mercaptoethyl)-1,5-diazacyclooctane and Its Methylated Derivative. *Inorg. Chem.* **1990,** *29*, 4364-4366.

66. Kruger, H.; Peng, G.; Holm, R., Low-potential nickel (III, II) complexes: new systems based on tetradentate amidate-thiolate ligands and the influence of ligand structure on potentials in relation to the nickel site in [NiFe]-hydrogenases. *Inorg. Chem.* **1991,** *30*, 734-742.

67. Farmer, P. J.; Reibenspies, J. H.; Lindahl, P. A.; Darensbourg, M. Y., Effects of sulfur site modification on the redox potentials of derivatives of [N, N'-bis (2-mercaptoethyl)-1, 5-diazacyclooctanato] nickel (II). *J. Am. Chem. Soc.* **1993,** *115*, 4665-4674.

68. Smee, J. J.; Miller, M. L.; Grapperhaus, C. A.; Reibenspies, J. H.; Darensbourg, M. Y., Subtle Bite-Angle Influences on N_2S_2Ni Complexes. *Inorg. Chem.* **2001,** *40*, 3601-3605.

69. Grapperhaus, C. A.; Maguire, M. J.; Tuntulani, T.; Darensbourg, M. Y., Singlet oxygen and the production of sulfur oxygenates of nickel (II) and palladium (II) thiolates. *Inorg. Chem.* **1997,** *36*, 1860-1866.

70. Hanss, J.; Krüger, H. J., First isolation and structural characterization of a nickel (III) complex containing aliphatic thiolate donors. *Angew. Chem. Int. Ed.* **1998,** *37*, 360-363.

71. Huang, H.-T.; Dillon, S.; Ryan, K. C.; Campecino, J. O.; Watkins, O. E.; Cabelli, D. E.; Brunold, T. C.; Maroney, M. J., The Role of Mixed Amine/Amide Ligation in Nickel Superoxide Dismutase. *Inorg. Chem.* **2018,** *57*, 12521-12535.

72. Johnson, O. E.; Ryan, K. C.; Maroney, M. J.; Brunold, T. C., Spectroscopic and computational investigation of three Cys-to-Ser mutants of nickel superoxide dismutase: insight into the roles played by the Cys2 and Cys6 active-site residues. *J. Biol. Inorg. Chem.* **2010,** *15*, 777-793.

73. Ryan, K. C.; Johnson, O. E.; Cabelli, D. E.; Brunold, T. C.; Maroney, M. J., Nickel superoxide dismutase: structural and functional roles of Cys2 and Cys6. *J. Biol. Inorg. Chem.* **2010,** *15*, 795-807.

74. Bryngelson, P. A.; Arobo, S. E.; Pinkham, J. L.; Cabelli, D. E.; Maroney, M. J., Expression, reconstitution, and mutation of recombinant Streptomycescoelicolor NiSOD. *J. Am. Chem. Soc.* **2004,** *126*, 460-461.

75. Ryan, K. C.; Guce, A. I.; Johnson, O. E.; Brunold, T. C.; Cabelli, D. E.; Garman, S. C.; Maroney, M. J., Nickel Superoxide Dismutase: Structural and Functional Roles of His1 and Its H-Bonding Network. *Biochemistry* **2015,** *54*, 1016-1027.

76. Pelmenschikov, V.; Siegbahn, P. E. M., Nickel Superoxide Dismutase Reaction Mechanism Studied by Hybrid Density Functional Methods. *J. Am. Chem. Soc.* **2006,** *128*, 7466-7475.

77. Prabhakar, R.; Morokuma, K.; Musaev, D. G., A DFT study of the mechanism of Ni superoxide dismutase (NiSOD): Role of the active site cysteine-6 residue in the oxidative half-reaction. *J. Comput. Chem.* **2006,** *27*, 1438-1445.

78. Szilagyi, R. K.; Bryngelson, P. A.; Maroney, M. J.; Hedman, B.; Hodgson, K. O.; Solomon, E. I., S K-Edge X-ray Absorption Spectroscopic Investigation of the Ni-Containing Superoxide Dismutase Active Site: New Structural Insight into the Mechanism. *J. Am. Chem. Soc.* **2004,** *126*, 3018-3019.

79. Ibers, J. A.; Holm, R. H., Modeling Coordination Sites in Metallobiomolecules. *Science* **1980,** *209*, 223-235.

80. Broering, E. P.; Truong, P. T.; Gale, E. M.; Harrop, T. C., Synthetic Analogues of Nickel Superoxide Dismutase: A New Role for Nickel in Biology. *Biochemistry* **2013,** *52*, 4-18.

81. Shearer, J.; Long, L. M., A Nickel Superoxide Dismutase Maquette That Reproduces the Spectroscopic and Functional Properties of the Metalloenzyme. *Inorg. Chem.* **2006,** *45*, 2358-2360.

82. Neupane, K. P.; Gearty, K.; Francis, A.; Shearer, J., Probing Variable Axial Ligation in Nickel Superoxide Dismutase Utilizing Metallopeptide-Based Models: Insight into the Superoxide Disproportionation Mechanism. *J. Am. Chem. Soc.* **2007,** *129*, 14605-14618.

83. Schmidt, M.; Zahn, S.; Carella, M.; Ohlenschläger, O.; Görlach, M.; Kothe, E.; Weston, J., Solution Structure of a Functional Biomimetic and Mechanistic Implications for Nickel Superoxide Dismutases. *ChemBioChem* **2008,** *9*, 2135-2146.

84. Tietze, D.; Breitzke, H.; Imhof, D.; Kothe, E.; Weston, J.; Buntkowsky, G., New Insight into the Mode of Action of Nickel Superoxide Dismutase by Investigating Metallopeptide Substrate Models. *Chem. - Eur. J.* **2009,** *15*, 517-523.

85. Shearer, J.; Neupane, K. P.; Callan, P. E., Metallopeptide Based Mimics with Substituted Histidines Approximate a Key Hydrogen Bonding Network in the Metalloenzyme Nickel Superoxide Dismutase. *Inorg. Chem.* **2009,** *48*, 10560-10571.

86. Tietze, D.; Tischler, M.; Voigt, S.; Imhof, D.; Ohlenschläger, O.; Görlach, M.; Buntkowsky, G., Development of a Functional cis-Prolyl Bond Biomimetic and Mechanistic Implications for Nickel Superoxide Dismutase. *Chem. - Eur. J.* **2010,** *16*, 7572-7578.

87. Krause, M. E.; Glass, A. M.; Jackson, T. A.; Laurence, J. S., Novel Tripeptide Model of Nickel Superoxide Dismutase. *Inorg. Chem.* **2010,** *49*, 362-364.

88. Tietze, D.; Voigt, S.; Mollenhauer, D.; Tischler, M.; Imhof, D.; Gutmann, T.; González, L.; Ohlenschläger, O.; Breitzke, H.; Görlach, M.; Buntkowsky, G., Revealing the Position of the Substrate in Nickel Superoxide Dismutase: A Model Study. *Angew. Chem. Int. Ed.* **2011,** *50*, 2946-2950.

89. Krause, M. E.; Glass, A. M.; Jackson, T. A.; Laurence, J. S., MAPping the Chiral Inversion and Structural Transformation of a Metal-Tripeptide Complex Having Ni-Superoxide Dismutase Activity. *Inorg. Chem.* **2011,** *50*, 2479-2487.

90. Glass, A. M.; Krause, M. E.; Laurence, J. S.; Jackson, T. A., Controlling the Chiral Inversion Reaction of the Metallopeptide Ni-Asparagine-Cysteine-Cysteine with Dioxygen. *Inorg. Chem.* **2012,** *51*, 10055-10063.

91. Krause, M. E.; Glass, A. M.; Jackson, T. A.; Laurence, J. S., Embedding the Ni-SOD Mimetic Ni-NCC within a Polypeptide Sequence Alters the Specificity of the Reaction Pathway. *Inorg. Chem.* **2013,** *52*, 77-83.

92. Shearer, J., Dioxygen and superoxide stability of metallopeptide based mimics of nickel containing superoxide dismutase: The influence of amine/amidate vs. bis-amidate ligation. *J. Inorg. Biochem.* **2013,** *129*, 145-149.

93. Shearer, J., Use of a Metallopeptide-Based Mimic Provides Evidence for a Proton-Coupled Electron-Transfer Mechanism for Superoxide Reduction by Nickel-Containing Superoxide Dismutase. *Angew. Chem. Int. Ed.* **2013,** *52*, 2569-2572.

94. Liu, Y.; Wang, Q.; Wei, Y.; Lin, Y.-W.; Li, W.; Su, J.-H.; Wang, Z.; Tian, Y.; Huang, Z.-X.; Tan, X., Functional conversion of nickel-containing metalloproteins via molecular design: from a truncated acetyl-coenzyme A synthase to a nickel superoxide dismutase. *Chem. Commun.* **2013,** *49*, 1452-1454.

95. Shearer, J.; Peck, K. L.; Schmitt, J. C.; Neupane, K. P., Cysteinate protonation and water hydrogen bonding at the active-site of a nickel superoxide dismutase metallopeptide-based mimic: implications for the mechanism of superoxide reduction. *J. Am. Chem. Soc.* **2014,** *136*, 16009-16022.

96. Campeciño, J. O.; Dudycz, L. W.; Tumelty, D.; Berg, V.; Cabelli, D. E.; Maroney, M. J., A Semisynthetic Strategy Leads to Alteration of the Backbone Amidate Ligand in the NiSOD Active Site. *J. Am. Chem. Soc.* **2015,** *137*, 9044-9052.

97. Tietze, D.; Sartorius, J.; Koley Seth, B.; Herr, K.; Heimer, P.; Imhof, D.; Mollenhauer, D.; Buntkowsky, G., New insights into the mechanism of nickel superoxide degradation from studies of model peptides. *Sci. Rep.* **2017,** *7*.

98. Tietze, D.; Koley Seth, B.; Brauser, M.; Tietze, A. A.; Buntkowsky, G., Ni^{II} Complex Formation and Protonation States at the Active Site of a Nickel Superoxide Dismutase-Derived Metallopeptide: Implications for the Mechanism of Superoxide Degradation. *Chem. - Eur. J.* **2018,** *24*, 15879-15888.

99. Lihi, N.; Csire, G.; Szakács, B.; May, N. V.; Várnagy, K.; Sóvágó, I.; Fábián, I., Stabilization of the Nickel Binding Loop in NiSOD and Related Model Complexes: Thermodynamic and Structural Features. *Inorg. Chem.* **2019,** *58*, 1414.

100. Domergue, J.; Pécaut, J.; Proux, O.; Lebrun, C.; Gateau, C.; Le Goff, A.; Maldivi, P.; Duboc, C.; Delangle, P., Mononuclear Ni(II) Complexes with a S3O Coordination Sphere Based on a Tripodal Cysteine-Rich Ligand: pH Tuning of the Superoxide Dismutase Activity. *Inorg. Chem.* **2019,** *58*, 12775-12785.

101. Lihi, N.; Kelemen, D.; May, N. V.; Fábián, I., The Role of the Cysteine Fragments of the Nickel Binding Loop in the Activity of the Ni(II)-Containing SOD Enzyme. *Inorg. Chem.* **2020,** *59*, 4772-4780.

102. Kelemen, D.; May, N. V.; Andrási, M.; Gáspár, A.; Fábián, I.; Lihi, N., High Enzyme Activity of a Binuclear Nickel Complex Formed with the Binding Loops of the NiSOD Enzyme**. *Chem. - Eur. J.* **2020,** *26*, 16767-16773.

103. Shearer, J.; Zhao, N., $[Me_4N](Ni^{II}(BEAAM))$: A Synthetic Model for Nickel Superoxide Dismutase That Contains Ni in a Mixed Amine/Amide Coordination Environment. *Inorg. Chem.* **2006,** *45*, 9637-9639.

104. Patel, R. N.; Singh, N.; Gundla, V. L. N., Synthesis, characterization and superoxide dismutase activity of some octahedral nickel(II) complexes. *Polyhedron* **2007,** *26*, 757-762.

105. Fiedler, A. T.; Brunold, T. C., Spectroscopic and Computational Studies of Ni^{3+} Complexes with Mixed S/N Ligation: Implications for the Active Site of Nickel Superoxide Dismutase. *Inorg. Chem.* **2007,** *46*, 8511-8523.

106. Stenson, P. A.; Board, A.; Marin-Becerra, A.; Blake, A. J.; Davies, E. S.; Wilson, C.; McMaster, J.; Schröder, M., Molecular and Electronic Structures of One-Electron Oxidized Ni^{II}–(Dithiosalicylidenediamine) Complexes: Ni^{III}–Thiolate versus Ni^{II}–Thiyl Radical States. *Chem. - Eur. J.* **2008,** *14*, 2564-2576.

107. Ma, H.; Chattopadhyay, S.; Petersen, J. L.; Jensen, M. P., Harnessing Scorpionate Ligand Equilibria for Modeling Reduced Nickel Superoxide Dismutase Intermediates. *Inorg. Chem.* **2008,** *47*, 7966-7968.

108. Shearer, J.; Dehestani, A.; Abanda, F., Probing Variable Amine/Amide Ligation in $Ni^{II}N_2S_2$ Complexes Using Sulfur K-Edge and Nickel L-Edge X-ray Absorption Spectroscopies: Implications for the Active Site of Nickel Superoxide Dismutase. *Inorg. Chem.* **2008,** *47*, 2649-2660.

109. Jenkins, R. M.; Singleton, M. L.; Almaraz, E.; Reibenspies, J. H.; Darensbourg, M. Y., Imidazole-Containing (N_3S)-Ni^{II} Complexes Relating to Nickel Containing Biomolecules. *Inorg. Chem.* **2009,** *48*, 7280-7293.

110. Nakane, D.; Funahashi, Y.; Ozawa, T.; Masuda, H., Synthesis of an N_3S_2-type Ni(II) Complex Directed to NiSOD Active Site and Its Structural, Electrochemical, and Spectroscopic Properties. *Trans. Mater. Res. Soc. Jpn* **2009,** *34*, 513-516.

111. Ma, H.; Wang, G.; Yee, G. T.; Petersen, J. L.; Jensen, M. P., Scorpionate-supported models of nickel-dependent superoxide dismutase. *Inorg. Chim. Acta* **2009,** *362*, 4563-4569.

112. Mullins, C. S.; Grapperhaus, C. A.; Frye, B. C.; Wood, L. H.; Hay, A. J.; Buchanan, R. M.; Mashuta, M. S., Synthesis and Sulfur Oxygenation of a (N_3S)Ni Complex Related to Nickel-Containing Superoxide Dismutase. *Inorg. Chem.* **2009,** *48*, 9974-9976.

113. Gale, E. M.; Patra, A. K.; Harrop, T. C., Versatile Methodology Toward NiN_2S_2 Complexes as Nickel Superoxide Dismutase Models: Structure and Proton Affinity. *Inorg. Chem.* **2009,** *48*, 5620-5622.

114. Daisuke, N.; Yasuhiro, F.; Tomohiro, O.; Hideki, M., A Square-planar Ni(II) Complex with an Asymmetric N_2S_2 Donor Set as a Model for the Active Site of Nickel-containing SOD: Structural Conversion Driven by Addition of a Strong Donor Ligand in the High Oxidation State. *Chem. Lett.* **2010,** *39*, 344-346.

115. Gennari, M.; Orio, M.; Pécaut, J.; Neese, F.; Collomb, M.-N.; Duboc, C., Reversible Apical Coordination of Imidazole between the Ni(III) and Ni(II) Oxidation States of a Dithiolate Complex: A Process Related to the Ni Superoxide Dismutase. *Inorg. Chem.* **2010,** *49*, 6399-6401.

116. Patel, R. N.; Shukla, K. K.; Singh, A.; Choudhary, M.; Patel, D. K.; Niclós-Gutiérrez, J.; Choquesillo-Lazarte, D., Spectral, structural, and superoxide dismutase activity of some octahedral nickel(II) complexes with tri-tetradentate ligands. *J. Coord. Chem.* **2010,** *63*, 3648-3661.

117. Nakane, D.; Kuwasako, S.-I.; Tsuge, M.; Kubo, M.; Funahashi, Y.; Ozawa, T.; Ogura, T.; Masuda, H., A square-planar Ni(II) complex with an N_2S_2 donor set similar to the active centre of nickel-containing superoxide dismutase and its reaction with superoxide. *Chem. Commun.* **2010,** *46*, 2142.

118. Mathrubootham, V.; Thomas, J.; Staples, R.; McCraken, J.; Shearer, J.; Hegg, E. L., Bisamidate and Mixed Amine/Amidate NiN_2S_2 Complexes as Models for Nickel-Containing Acetyl Coenzyme A Synthase and Superoxide Dismutase: An Experimental and Computational Study. *Inorg. Chem.* **2010,** *49*, 5393-5406.

119. Gale, E. M.; Narendrapurapu, B. S.; Simmonett, A. C.; Schaefer, H. F.; Harrop, T. C., Exploring the effects of H-bonding in synthetic analogues of nickel superoxide dismutase (Ni-SOD): experimental and theoretical implications for protection of the Ni-SCys bond. *Inorg. Chem.* **2010,** *49*, 7080.

120. Gale, E. M.; Simmonett, A. C.; Telser, J.; Schaefer, H. F.; Harrop, T. C., Toward Functional Ni-SOD Biomimetics: Achieving a Structural/Electronic Correlation with Redox Dynamics. *Inorg. Chem.* **2011,** *50*, 9216-9218.

121. Gale, E. M.; Cowart, D. M.; Scott, R. A.; Harrop, T. C., Dipeptide-based models of nickel superoxide dismutase: solvent effects highlight a critical role to Ni-S bonding and active site stabilization. *Inorg. Chem.* **2011,** *50*, 10460.

122. Herdt, D. R.; Grapperhaus, C. A., Kinetic study of nickel-thiolate oxygenation by hydrogen peroxide. Implications for nickel-containing superoxide dismutase. *Dalton Trans.* **2012,** *41*, 364-366.

123. Ramadan, A. E.-M. M., Macrocyclic nickel(II) complexes: Synthesis, characterization, superoxide scavenging activity and DNA-binding. *J. Mol. Struct.* **2012,** *1015*, 56-66.

124. Lee, W.-Z.; Chiang, C.-W.; Lin, T.-H.; Kuo, T.-S., A Discrete Five-Coordinate Ni^{III} Complex Resembling the Active Site of the Oxidized Form of Nickel Superoxide Dismutase. *Chem. - Eur. J.* **2012,** *18*, 50-53.

125. Rawat, S. P., Synthesis, spectroscopic, electrochemical, magnetic properties and super oxide dismutase activity of nickel (II) complexes with unsymmetrical Schiff base ligands. *IOSR J. Appl. Chem.* **2013,** *6*, 25-31.

126. Nakane, D.; Wasada-Tsutsui, Y.; Funahashi, Y.; Hatanaka, T.; Ozawa, T.; Masuda, H., A novel square-planar Ni(II) complex with an amino-carboxamido-dithiolato-type ligand as an active-site model of NiSOD. *Inorg. Chem.* **2014,** *53*, 6512-6523.

127. Chatterjee, S. K.; Maji, R. C.; Barman, S. K.; Olmstead, M. M.; Patra, A. K., Hexacoordinate Nickel(II)/(III) Complexes that Mimic the Catalytic Cycle of Nickel Superoxide Dismutase. *Angew. Chem. Int. Ed.* **2014,** *126*, 10348-10353.

128. Chiang, C. W.; Chu, Y. L.; Chen, H. L.; Kuo, T. S.; Lee, W. Z., Synthesis and Characterization of $Ni^{III}N_3S_2$ Complexes as Active Site Models for the Oxidized Form of Nickel Superoxide Dismutase. *Chem. - Eur. J.* **2014,** *20*, 6283-6286.

129. Broering, E. P.; Dillon, S.; Gale, E. M.; Steiner, R. A.; Telser, J.; Brunold, T. C.; Harrop, T. C., Accessing Ni(III)-Thiolate Versus Ni(II)-Thiyl Bonding in a Family of Ni–N_2S_2 Synthetic Models of NiSOD. *Inorg. Chem.* **2015,** *54*, 3815.

130. Snider, V. G.; Farquhar, E. R.; Allen, M.; Abu-Spetani, A.; Mukherjee, A., Design and reactivity of Ni-complexes using pentadentate neutral-polypyridyl ligands: Possible mimics of NiSOD. *J. Inorg. Biochem.* **2017,** *175*, 110-117.

131. Truong, P. T.; Gale, E. M.; Dzul, S. P.; Stemmler, T. L.; Harrop, T. C., Steric Enforcement about One Thiolate Donor Leads to New Oxidation Chemistry in a NiSOD Model Complex. *Inorg. Chem.* **2017,** *56*, 7761-7780.

132. Steiner, R. A.; Dzul, S. P.; Stemmler, T. L.; Harrop, T. C., Synthesis and Speciation-Dependent Properties of a Multimetallic Model Complex of NiSOD That Exhibits Unique Hydrogen-Bonding. *Inorg. Chem.* **2017,** *56*, 2849-2862.

133. Senaratne, N. K.; Mwania, T. M.; Moore, C. E.; Eichhorn, D. M., Ni complexes of N_2S ligands with amine/imine and amine/amide donors with relevance to the active site of Ni superoxide dismutase. *Inorg. Chim. Acta* **2018,** *476*, 27-37.

134. Domergue, J.; Guinard, P.; Douillard, M.; Pécaut, J.; Proux, O.; Lebrun, C.; Le Goff, A.; Maldivi, P.; Delangle, P.; Duboc, C., A Bioinspired NiII Superoxide Dismutase Catalyst Designed on an ATCUN-like Binding Motif. *Inorg. Chem.* **2021,** *60*, 12772-12780.

135. Truong, P. T.; Howell, J. L.; Chakraborty, I.; Olmstead, M. M.; Harrop, T. C., Synthetic Models of NiSOD with N_3S_2 Coordination: Modulation of Ligand Basicity Leads to Five-Coordinate Ni^{2+} and Reversible Ni-Redox. *submitted to Inorg. Chem.* **2021**, manuscript id: ic-2021-03791z.

136. Leffek, K. T.; Pruszynski, P.; Thanapaalasingham, K., Basicity of substituted 2-phenyl-1,1,3,3- tetramethylguanidines and other bases in acetonitrile solvent. *Can. J. Chem.* **1989,** *67*, 590-595.

137. Tshepelevitsh, S.; Kütt, A.; Lõkov, M.; Kaljurand, I.; Saame, J.; Heering, A.; Plieger, P. G.; Vianello, R.; Leito, I., On the Basicity of Organic Bases in Different Media. *Eur. J. Org. Chem.* **2019,** *2019*, 6735-6748.

138. Pavlishchuk, V. V.; Addison, A. W., Conversion constants for redox potentials measured versus different reference electrodes in acetonitrile solutions at 25°C. *Inorg. Chim. Acta* **2000,** *298*, 97-102.

CHAPTER 2

SYNTHESIS AND PROPERTIES OF A NISOD MODEL WITH AN APICAL IMIDAZOLE DONOR[1]

[1] Howell, J. L.; Harrop, T. C. To be submitted to Inorganic Chemistry.

2.1 Abstract

Ni superoxide dismutase (NiSOD) is a redox-active Ni enzyme that interestingly performs chemistry with reactive oxygen species (ROS) despite its oxygen-sensitive thiolate-rich active site. The *objective of this research* is to investigate the chemistry of Ni superoxide dismutase (NiSOD) by synthesizing the most structurally accurate low molecular weight (LMW) model of its active sites in order to probe their chemical properties and reactivities towards reactive oxygen species (ROS). For this work, Ni^{2+} complexes of the N_3S_2 ligand $[N_3S_2^{NMeIm}]^{3-}$ ($[N_3S_2^{NMeIm}]^{3-}$ = deprotonated form of N-(2-mercaptoethyl)-2-((2-mercaptoethyl)((1-methyl-1H-imidazol-2-yl)methyl)amino)acetamide), including $Na[Ni(N_3S_2^{NMeIm})]$ (**4**^{Na}) and $Et_4N[Ni(N_3S_2^{NMeIm})]$ (**4**^{Et4N}), as models of NiSOD were synthesized. These complexes feature a structurally accurate set of mixed N/S planar donors as well as imidazole axial donor that most closely reflects His1 of NiSOD. The X-ray crystal structure of **4**^{Na} paired with spectroscopic measurements from ^{1}H NMR, IR, UV-vis, and mass spectrometry (MS), reveal a planar Ni^{2+} coordinated by the planar N_2S_2 donors of the ligand, comparable to those of reduced NiSOD ($NiSOD_{red}$) as well other models. Also like previous models, reactivity of **4 s**eems to be primarily S-based rather than Ni-based as in the enzyme as evidenced by irreversible electrochemical measurements and MS analysis of the oxidation products. Unlike previous models, the persistence of UV-vis signal of **4**^{Na} even six days after air exposure indicate this model is more resistant to decomposition upon oxygenation (presumably at the S groups). All experiments point to a similarity in electronic structure of **4**^{Na} to that of $NiSOD_{red}$ while the lack of axial coordination emphasizes the essential role of the secondary sphere present in the native enzyme, but absent in **4**^{Na}.

2.2 Introduction

Aerobic respiration is an essential process for most life on Earth, however, intermediates of O_2 metabolism are also reactive enough to cause cellular damage.[1-2] These intermediates, known as reactive oxygen species (ROS), have been implicated in a variety of diseases including Alzheimer's, Parkinson's, amyotrophic lateral sclerosis (ALS), and more.[3-7] Superoxide ($O_2^{\bullet-}$) is the first ROS generated during O_2 reduction and is the starting species for subsequent ROS including hydroxyl radical, an extremely potent and oxidant ($E^{o\prime}$ = +2.31 V vs. NHE, pH 7, 25 ºC) capable of crossing membrane barriers due to its neutral charge and performing indiscriminate oxidation throughout the cell.[1, 8] As a result, aerobic organisms have developed metalloenzymes capable of defending the cell against ROS, namely superoxide dismutase (SOD).[1] SODs use a metal center with a redox potential suitable for both the oxidation (Eq. 2.1) and reduction (Eq. 2.2) of $O_2^{\bullet-}$ into O_2 and H_2O_2, respectively.[1] This disproportionation is highly efficient, operating at a near-diffusion limited rate ($k_{cat} \approx 10^9\ M^{-1}s^{-1}$).[2, 6, 9]

$$M^{ox} + O_2^{\bullet-} \rightarrow M^{red} + O_2 \qquad \text{(Eq. 2.1)}$$

$$\underline{M^{red} + O_2^{\bullet-} + 2H^+ \rightarrow M^{ox} + H_2O_2} \qquad \text{(Eq. 2.2)}$$

$$\text{Overall: } 2O_2^{\bullet-} + 2H^+ \rightarrow O_2 + H_2O_2 \qquad \text{(Eq. 2.3)}$$

There are four types of SODs, categorized by the metal(s) at their active site including CuZn, Mn, Fe, and Ni.[1] NiSOD, found primarily in bacteria and some eukarya, is the latest and most unusual member of the SOD family (Fig. 2.1).[1, 10] Unlike others, NiSOD utilizes a metal (Ni) and coordination environment (including CysS-donors) generally ill-suited for O_2-derived redox chemistry, i.e. redox-active Ni-enzymes are generally found in anaerobes and CysS-donors are themselves susceptible to oxidation.[11-12] In NiSOD, Ni is coordinated by two CysS, one peptido-

N, the primary amine of His1, and the His1-Nδ (unbound in reduced (Ni^{2+}) enzyme; coordinated when oxidized to Ni^{3+}; Scheme 2.1).[10]

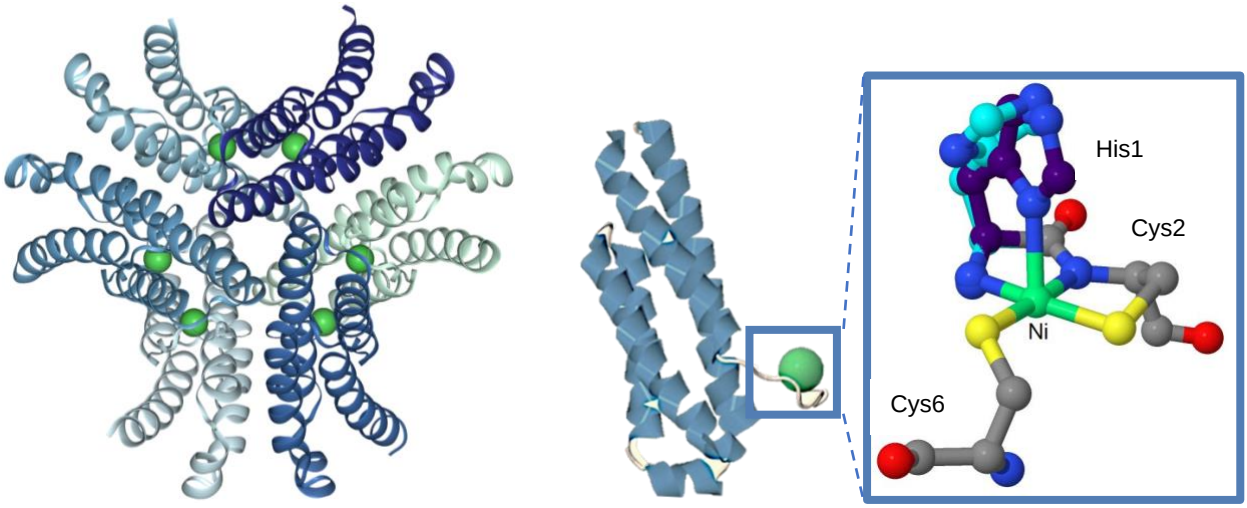

Figure 2.1. X-ray crystal structure of NiSOD from *Streptomyces coelicolor,* (1.30 Å resolution, PDB: 1T6U). (*Left*) Homohexameric NiSOD enzyme; each subunit displayed in a different color; Ni centers shown as green spheres. (*Center*) NiSOD subunit with Ni binding hook motif. (*Right*) NiSOD active site with His1 C atoms colored to depict the reduced Ni^{2+} (cyan) and the oxidized Ni^{3+} (violet) states. Images generated with Jmol and Pymol.[13-14]

Scheme 2.1. Currently understood NiSOD disproportionation process. Reduced NiSOD active site ($NiSOD_{red}$, left), oxidized NiSOD active site ($NiSOD_{ox}$, right).[1]

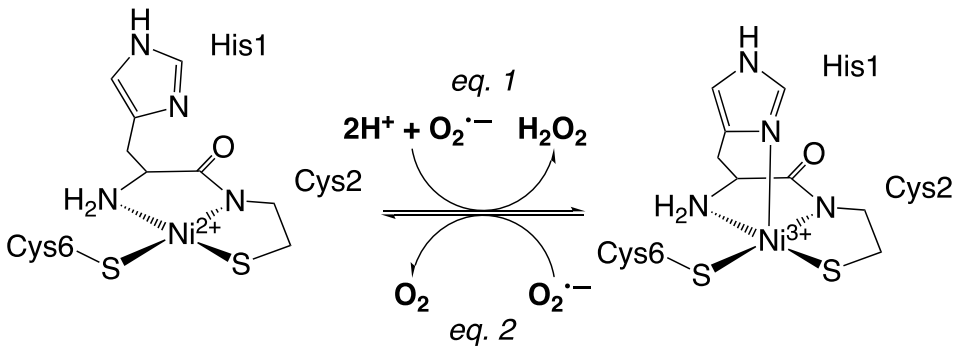

One proposal is that axial His1-Nδ coordination, in combination with ***specific*** basal plane $N_{peptide}N_{amine}S_2$ ligation, is required to achieve Ni^{3+}, maintain a five-coordinate (5C) active site during catalysis, and promote a Ni-based redox-active MO (vs. the covalent Ni(dπ)-S(pπ)

antibonding HOMO in planar Ni-N_2S_2 complexes).[15-21] However, mechanistic detail for such a unique SOD remains unclear. One accepted mechanism of NiSOD supposes that the His1-Nδ axial donor is labile during catalysis which does not agree very well with NiSOD's extremely efficient catalytic rate.[1] Questions concerning the type of interaction between Ni and $O_2^{\bullet-}$ (i.e. inner- or outer-sphere electron transfer) are still unanswered as well.[1, 14, 16-17] During the H_2O_2-forming half reaction of SOD, coordinated CysS residues are likely to serve as binding sites for the required protons (as proposed in [NiFe] hydrogenase, another redox-active Ni-thiolate enzyme).[22] This would also provide an explanation for the exceptional O_2/ROS stability of the CysS donors, but where these protons originate and how they interact with the substrate has yet to be firmly established. Indeed, NiSOD function is based on its underlying electronic structure, which supports a $Ni^{3+/2+}$ ($E_{1/2}$ = 0.290 V vs. NHE)[17] couple at the center of the superoxide redox window (+0.91 and –0.18 V vs. NHE, pH 7)[1], but the characteristics that determine this electronic structure have yet to be fully elucidated.[14, 23]

To understand the critical features that promote Ni-based electrochemical activity in NiSOD (as well as other Ni-enzymes), our group has designed and synthesized several Ni-N/S complexes as low molecular weight (LMW) models of the NiSOD active site (Scheme 2.2).[13, 15, 24-25] Model complexes from our group incorporate $N_{carboxamide}N_{amine}S_2$ planar ligand donors with a potential axial N-donor tethered to the N_{amine}. [13, 15, 24-25] First and second generation complexes, $[Ni(N_3S_2)]^-$ (**1**) and $[Ni(N_3S_2^{Me2})]^-$ (**2**), utilized pyridine (py) as the axial donor based on synthetic ease, similar Lewis basicity (pK_a = 5.94, H_2O)[26], and structural characteristics to that of the native imidazole (pK_a = 7.21, H_2O)[27] from His1. [13, 15, 24-25, 28] However, redox-activity continued to occur at the S-donor *trans* to the caboxamido-N, even when altered to be more sterically robust to prevent S-based reactivity.[24] The third-generation model $[Ni(N_3S_2^{NEM})]^-$ (**3**) sought to encourage axial N

binding to the Lewis acidic Ni^{2+} metal center with a more Lewis basic axial N-donor, morpholine (NEM, pK_a = 7.4, H_2O)[29], which yielded similar S-based redox activity.[13] These results suggest that enhanced basicity or steric bulk *alone* cannot enforce the electronic structure required to support the 5C geometry necessary for SOD activity. Rather, there are additional characteristics of the axial N-donor and/or the planar ligand set, such as ligand-field strength (i.e. π-accepting ability of axial N, σ-donating ability of S, S nucleophilicity), that influence NiSOD's electronic structure and should be probed to better grasp the NiSOD mechanism and furthering the field of NiSOD/Ni-thiolate chemistry.

Scheme 2.2. Previously published NiSOD models from our group; complexes **1-3** from left to right.

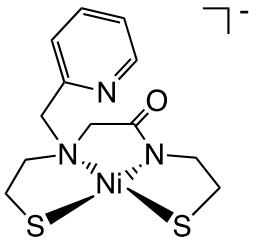

(1)

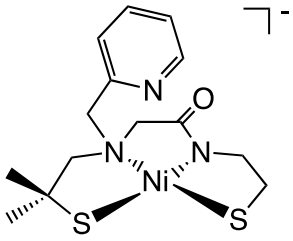

(2)

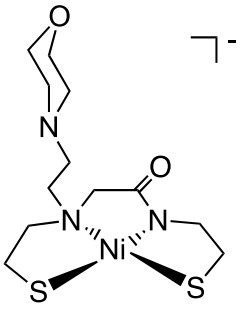

(3)

The goal of this work is to design, synthesize, and characterize a LMW NiSOD analogue with the general formula $[Ni(N_3S_2)]^{-1}$ which structurally and electronically models the coordination sphere in the enzyme. For this work, Ni^{2+} complexes of the N_3S_2 ligand $[N_3S_2^{NMeIm}]^{3-}$ ($[N_3S_2^{NMeIm}]^{3-}$ = deprotonated form of N-(2-mercaptoethyl)-2-((2-mercaptoethyl)((1-methyl-1H-imidazol-2-yl)methyl)amino)acetamide), including $Na[Ni(N_3S_2^{NMeIm})]$ (**4**^{Na}) and $Et_4N[Ni(N_3S_2^{NMeIm})]$ (**4**^{Et4N}), were synthesized as models of NiSOD. These complexes feature a structurally and electronically accurate set of mixed N/S planar donors as well as imidazole axial

donor that most closely reflects His1 of NiSOD. It is expected that the basicity of NMeIm being similar to NEM and greater than py, coupled with the π-accepting ability of NMeIm, which is present in py but absent in NEM will produce a 5C square pyramidal geometry without the need to modify the thiolates as in **3**. The stronger field nature of NMeIm should promote the low-spin state Ni^{2+} to result in a 5C Ni^{2+} with a long Ni---N_{axial} as in **3**. Because the electronic structure of low-spin 5C Ni^{2+} is primarily d_{z2}-based[16], we anticipate a model that is poised for functionality and given that all electrochemical prerequisites are met. Results of this synthetic analogue approach are anticipated to advance our mechanistic understanding of NiSOD. This work will also answer important questions regarding redox-active Ni-thiolate containing enzymes, which constitute a class of biocatalysts that participate in diverse reactions critical to life processes involving the global C, N, and O cycles.[1, 22, 30]

2.3 Results and Discussion

2.3.1 Synthesis and Properties of N_3S_2 Ligand

Synthesis of the pentadentate ligand ($H_3N_3S_2^{NMeIm}$•2HCl H = dissociable hydrogens) follows procedures used for other NiSOD models from our lab (Scheme 2.3). [13, 24-25] Much like the prior generation, the HCl salt of the ligand is much easier to handle and obtain accurate measurements for. Trifluoroacetic acid (TFA) was also difficult to remove from this deprotected ligand, likely due to the similar basicity of NMeIm (pK_a of N-NMeIm – 7.21; pK_a of N-NEM – 7.4 both in H_2O).[27, 29] Defining spectroscopic properties are listed in the Materials and Methods section and indicated on the spectra in the Supplemental Information (SI) section (Figures 2.S1-2.S8).

Scheme 2.3. Synthesis of $H_3N_3S_2^{NMeIm}$•2HCl ligand and Ni^{2+} Complex **4**.

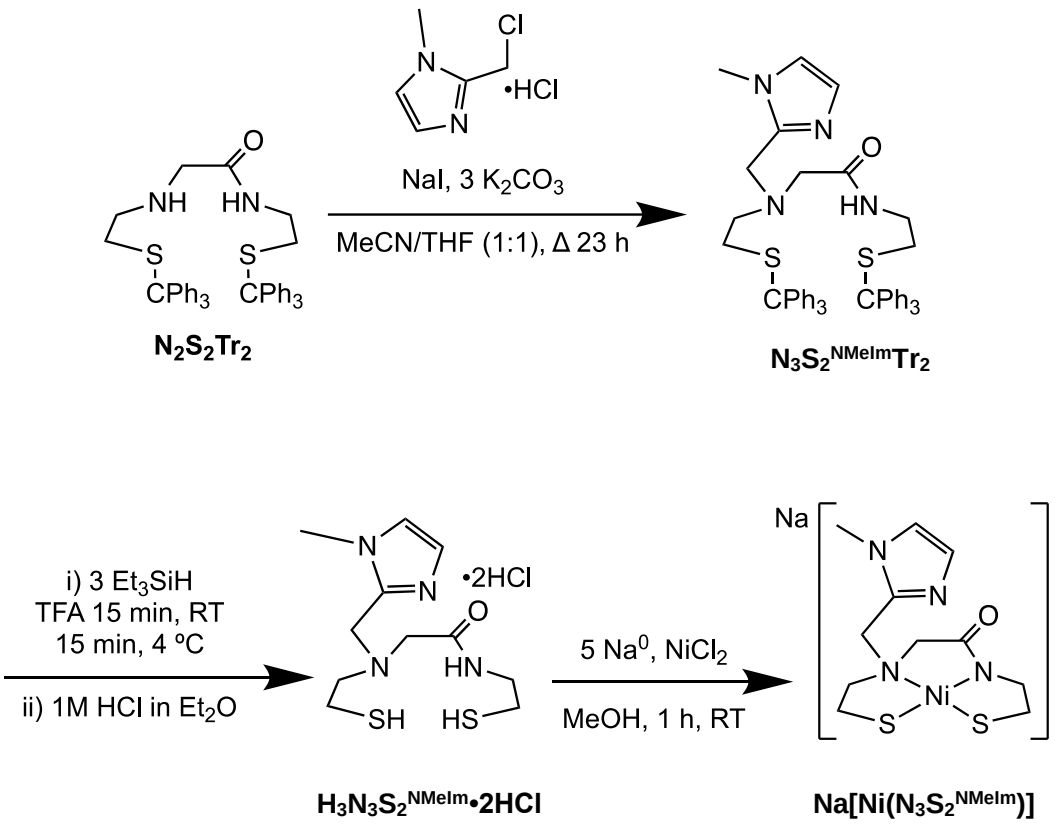

2.3.2 Synthesis of Ni^{2+} and Zn^{2+} Complexes

$Na[Ni(N_3S_2^{NMeIm})]$ (**4**^{Na}) was synthesized by reacting the deprotonated ligand with $NiCl_2$ (1:1) in MeOH to yield the red-brown complex in excess of 100% yield. This excess is likely NaCl which is generated as a byproduct of the reaction and was difficult to remove due to very similar solubility of **4**^{Na} and NaCl. Complex **4** is soluble in polar solvents (MeOH, H_2O, and DMF) with very slight solubility in MeCN and THF. In order to eliminate the H-bonding effects of polar-protic solvents, namely on the apical N-donor, studies and characterization of **4** should be conducted in aprotic media, however, **4**^{Na} is not soluble in these types of solvents. To enhance solubility of **4** in less polar and aprotic solvents, the Na^+ counterion was exchanged with Et_4N^+ by stirring **4**^{Na} and Et_4NCl (1:1) in MeCN to yield the red-brown $Et_4N[Ni(N_3S_2^{NMeIm})]$ (**4**^{Et4N}**)** complex

in 92% yield. Using analogous synthetic conditions, the Zn^{2+} analogue Na[Zn($N_3S_2^{NMeIm}$)] (**5**) was produced using $ZnCl_2$ and isolated as an off-white powder in 80% yield.

2.3.3 Spectroscopic Properties of Ni^{2+} and Zn^{2+} Complexes

All metal complexes were characterized by FTIR, ^{1}H NMR, UV-vis, low resolution electrospray ionization mass spectrometry (LR-ESI-MS), and CHN analyses. IR spectra of each complex reveals a characteristic downshift in ν_{CO} by approximately 80-90 cm^{-1} as well as loss of the ν_{NH} signal as compared to the salt of the ligand (Figures 2.S7, 2.S14, 2.S21, and 2.S28). These signals indicate coordination of the carboxamido-N. The identity of each complex is further supported by LR-ESI-MS which shows molecular ion peaks for the anion of each complex that agree with simulated isotopic distributions (Figures 2.S16, 2.S23, 2.S24, and 2.S29). As expected, ^{1}H NMR of all spectra show signals within 0-10 ppm, indicating formation of diamagnetic complexes (Figures 2.S9-10, 2.S18, and 2.S25). Further NMR analysis of all complexes using COSY (Figures 2.2, 2.S20, and 2.S27), HSQC (Figure 2.S12) and ROESY (Figure 2.S13) shows a high degree of coupling across the complex and a variety of parts of the molecule that are spatially close to one another. The large number of unique COSY signals could be due to long-range coupling (e.g ^4J and ^5J) across the molecule and/or from through-space interactions between atoms that are spatially close to one another.[31] Such long range coupling is often observed in large, rigid systems and results from the coplanarity of protons that may be more than three bonds away from one another. Considering the very protic media in which these spectra are collected (CD_3OD and D_2O), it is possible that H-bonding to $\mathbf{4^{Na}}$ may hold the molecule in a more rigid conformation, allowing for a detectable signal from the long-range coupling of protons with a high degree of coplanarity. Though the solution structure is likely not identical to the solid-state structure, the

crystal structure of $\mathbf{4^{Na}}$ (*vide infra*) does show several somewhat coplanar protons more than 3 bonds apart that could cause this long-range coupling. By orienting the molecule so that carbons greater than one bond away from another overlap, the coplanarity of long-range protons can be visually assessed (Figure 2.3). Specifically, the C (C7) bridging the NMeIm ring to the amine of the N_2S_2 ligand frame has two protons that are nearly adjacent to several protons on the N_2S_2 ligand frame (those on C4 and C5) (Figure 2.3, B and C) as well as the methyl group of NMeIm (C11) (Figure 2.3, D). One proton from C4, C5, and C7 are all oriented similarly forming a triangle that may exhibit unusual long-range coupling (Figure 2.3, E). Additionally, both sets of protons on each C that is adjacent to the amine of the N_2S_2 ligand frame are considerably planar and could exhibit some of the long-range coupling observed (Figure 2.3, F). Together with the typical ^3J signals observed in COSY, these additional signals make specific proton assignment much more complicated. UV-vis spectra of each Ni^{2+} complex exhibit typical features observed in other NiSOD models[13, 24-25, 32-36] and in reduced NiSOD[14, 16-17, 37], i.e., weak intensity ligand-field d-d transitions at ~450 nm and ~570 nm (Table 2.1, Figures 2.S15 and 2.S22).

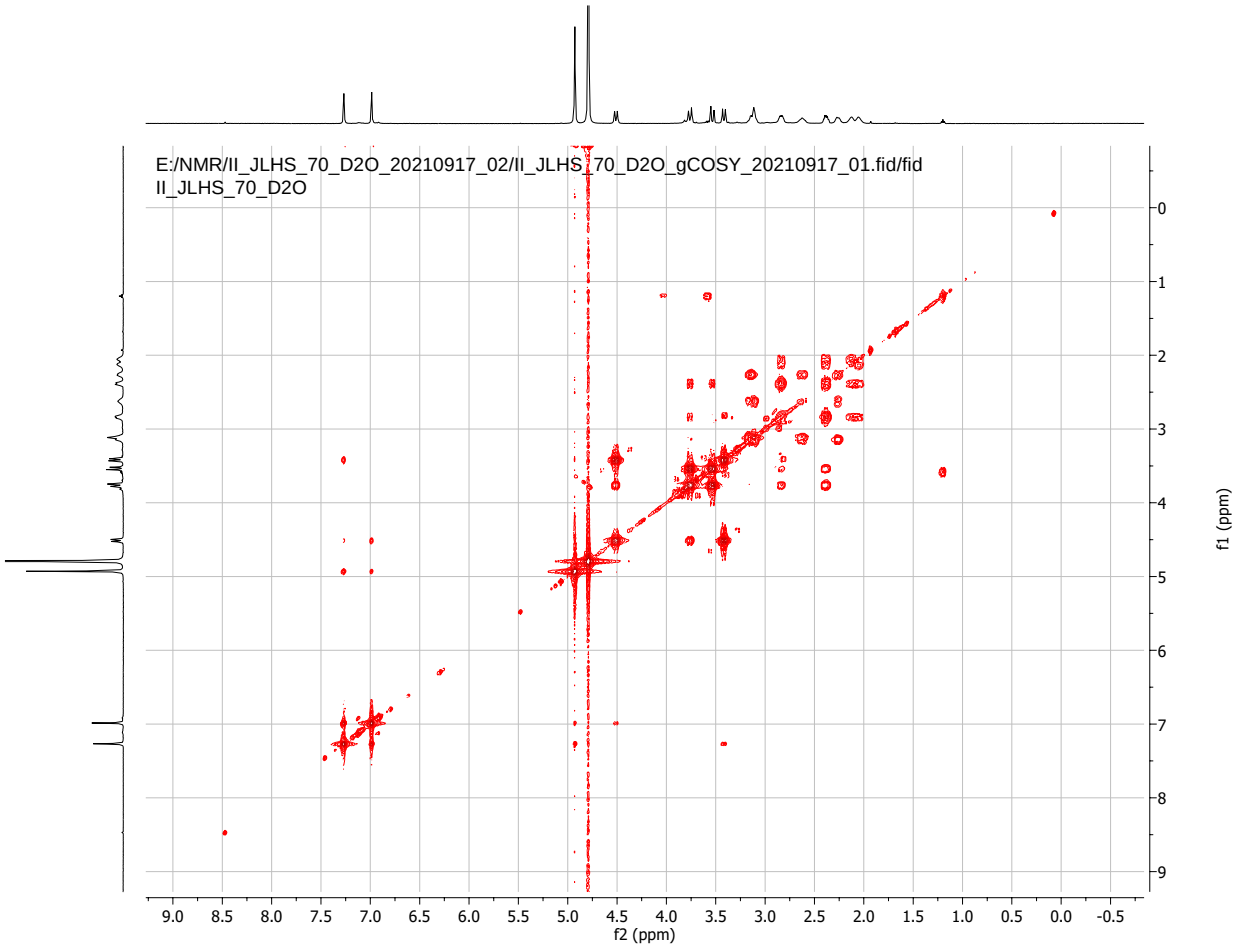

Figure 2.2. COSY NMR of $\mathbf{4^{Na}}$ in D_2O (500 MHz, δ from protio solvent).

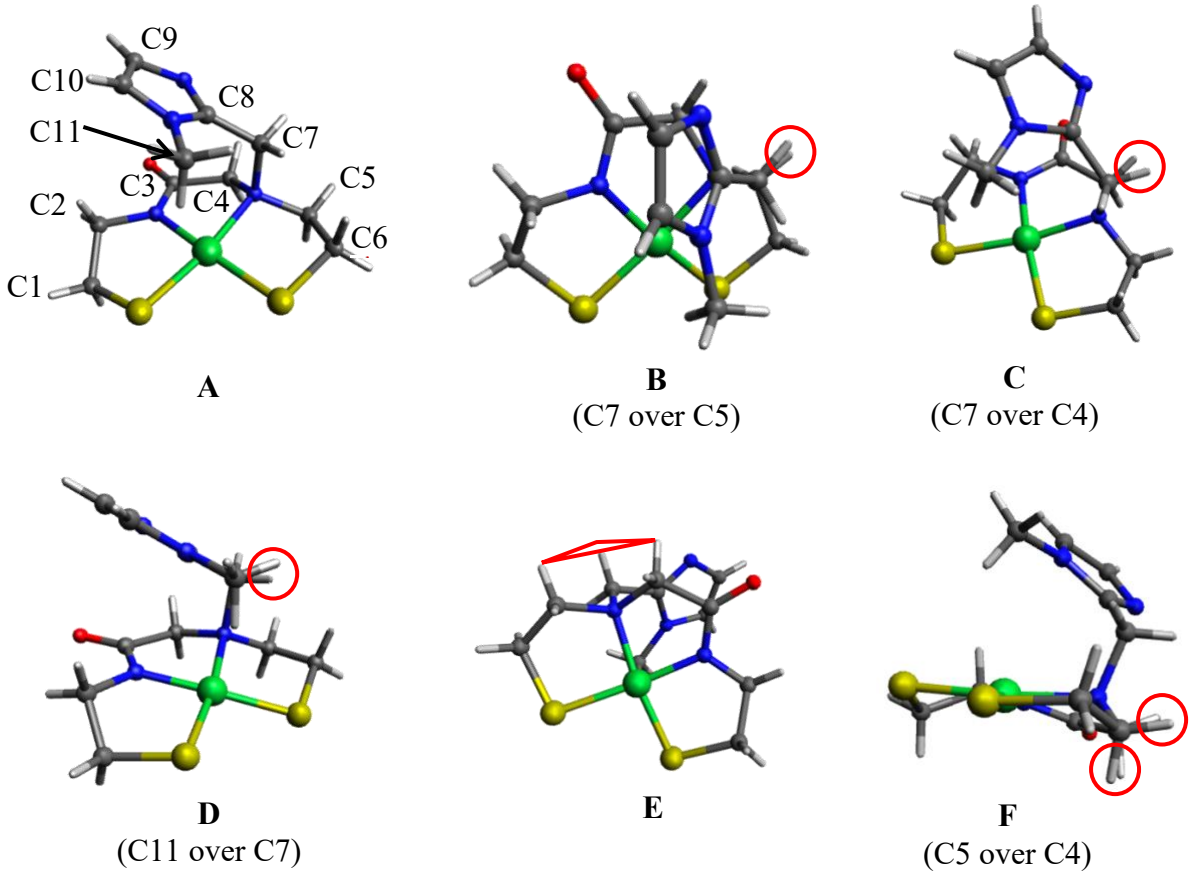

Figure 2.3. (A) Structure of the anion of Na[Ni($N_3S_2^{NMeIm}$)]•2MeOH (**4•2MeOH**) oriented to clearly show the structure. (B) A "top-down" orientation that aligns C7 on top of C5. (C) A rotated orientation that aligns C7 on top of C4. (D) A rotated orientation that aligns C11 on top of C7. (E) A "bottom-up" view showing the similar orientation of protons on C5, C7, and C4 (moving left to right). (F) A side view that aligns C4 and C5. Potentially long-range coupled protons are indicated with red circles and triangles.

Table 2.1. UV-vis Spectroscopic Data of NiSOD and Select NiSOD Models[a]

Complex	**λ (nm) (ε (M^{-1} cm^{-1}))[b]**	**ref**
$NiSOD_{red}$	450 (480), 543 (150)[c]	16
K[Ni(N_3S_2)] (**1**)	449 (320), 570 sh (90)	25
Na[Ni($N_3S_2^{Me2}$)] (**2**)	459 (250), 557 sh (75)	24
Na[Ni($N_3S_2^{NEM}$) (**3**)	455 (238), 575 sh (64)	13
Na[Ni($N_3S_2^{NMeIm}$)] (**4**)	454, 565	TW

[a]Abbreviations: sh = shoulder; TW = this work. [b]UV–vis spectra reported for MeOH solutions unless otherwise stated. [c]~50% v/v glycerol/ tris buffer (pH 8.5).

2.3.4 X-ray Structure of Ni^{2+} Complex

Characterization of $\mathbf{4^{Na}}$ also included X-ray diffraction (XRD), the details of which can be found in the SI section (Table 2.S1). Orange block crystals of $\mathbf{4^{Na}}$•2MeOH were crystallized from the slow diffusion of Et_2O into a solution of $\mathbf{4^{Na}}$ in MeOH at –25 ºC over nine days. The structure shows coordination of Ni^{2+} to the mixed amine/amide N_2S_2 donor set in a square planar geometry very similar to the primary coordination sphere of reduced NiSOD (Figure 2.4). This geometry is further confirmed by the very low tetrahedral distortion parameter τ_4 (= 0 for square-planar; = 1 for tetrahedral[38]) for $\mathbf{4^{Na}}$ (τ_4 = 0.12), which is slightly more distorted than previous model complexes as well as reduced NiSOD, and still square-planar. All bond lengths between the ligand and Ni^{2+} are very similar to those of reduced NiSOD as well as other similar NiSOD model complexes (Table 2.2). Notably, the Ni–N_{amide} bond length (Ni–N1 = 1.8541 (13) Å) is the shortest due to the strongly σ-donating character of this N-donor and is a feature present in previous generations of NiSOD model complexes. This strong σ-donation prompts a *trans* effect on the Ni–$S_{trans\text{-amide}}$ bond which is consequently longer than that of Ni–$S_{trans\text{-amine}}$ in all prior synthetic analogues. This elongation, however, is not observed in $\mathbf{4^{Na}}$•2MeOH (Ni–S2 = 2.1692 (5) Å; Ni–S1 = 2.1736 (5) Å) and may be a result of interactions between S2 and Na^+ in the crystal lattice (Figure 2.5) which contract the Ni–S2 bond to alleviate the Ni dπ-S pπ repulsions due to the antibonding nature of the HOMO, an electronic structural feature present in reduced NiSOD and synthetic analogues alike.[13, 16, 24] Despite the similar basicity of NEM and NMeIm, the Im-N-donor is closer (Ni---N_{axial} = 4.215 Å) to the central Ni than that of **3** (Ni---N^{NEM}_{axial} = 4.50 Å) that may emphasize the favorable effect that field strength/π-donating ability of the axial ligand has in addition to basicity of the N-donor. However, this more likely results from the packing in the solid state and in both structures, the axial N-donor is unbound as in $NiSOD_{red}$. Each Ni---N_{axial} distance

in $\mathbf{4^{Na}}$ is in fact longer than that of **1** (Ni---N^{py}_{axial} = ~3.21 Å), **2** (Ni---N^{py}_{axial} = ~3.23 Å), and reduced NiSOD (average Ni---N_{axial} = 4.11 Å), however, the angle between the basal plane and the plane of the aromatic axial donor (basal-arom plane ∠) is appreciably smaller, a sign that the axial donor ligand is brought closer to the Ni-center overall though individual N-donors may not be. Most notably, this angle in $\mathbf{4^{Na}}$ (40.94°) is nearly identical to that of the reduced NiSOD active site (40.95°). Solid state structural analysis of $\mathbf{4^{Na}}$ clearly shows that incorporation of NMeIm as the axial ligand results in a very similar model complex to prior generations as well as to reduced NiSOD and even improves upon several structural aspects including basal-arom plane ∠, τ_4 parameter, and Ni---N_{axial} distance which are anticipated to reflect electronic structural similarity capable of electronic and electrochemical NiSOD mimicry.

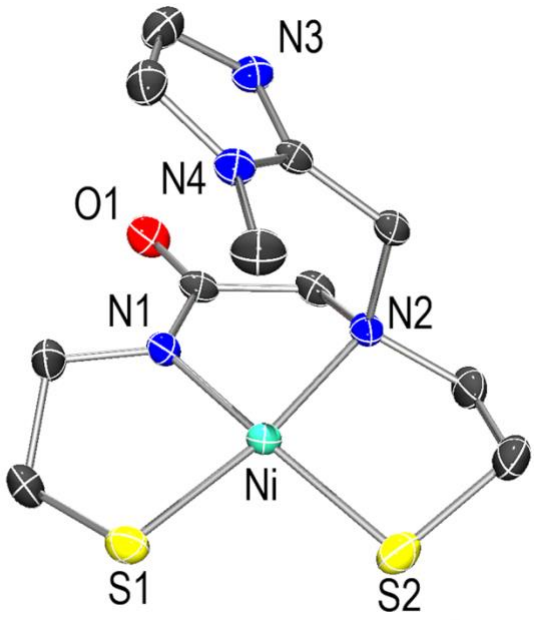

Figure 2.4. Structure of the anion of Na[Ni($N_3S_2^{NMeIm}$)]•2MeOH (**4•2MeOH**) showing 50% thermal probability ellipsoids with the atom labeling scheme. H atoms, Na^+ counterion, and MeOH molecules of crystallization are omitted for clarity. Selected bond angles (deg): N2–Ni–S1 = 171.65(4), N1–Ni–S2 = 171.62(4), S1–Ni–S2 = 96.279(18), N2–Ni–S2 = 91.20(4), N1–Ni–S1 = 88.49(4), N2–Ni–N1 = 84.54(6).

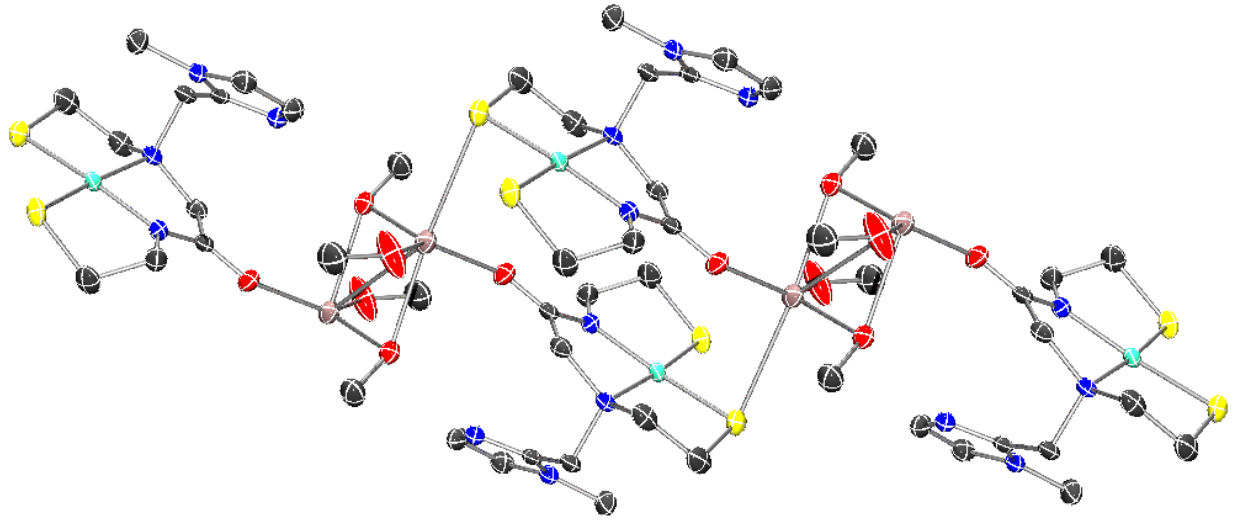

Figure 2.5. ORTEP diagram of the extended lattice of $\mathbf{4^{Na}}$ at 50% thermal probability ellipsoids. H atoms omitted for clarity. C = gray; Ni = aquamarine; S = yellow; N = blue; O = red; Na = pink.

Table 2.2. Select Structural Parameters for $NiSOD_{red}$ (PDB code) and Prior Generation NiSOD Models[a].

Complex	Ni–N_{amide}	Ni–N_{amine}	Ni–$S_{trans\text{-}amide}$	Ni–S	Ni---N_{axial}	Basal-arom plane ∠	τ_4	ref
$NiSOD_{red}$ (1T6U)	1.91	1.87	2.19	2.16	4.11[b]	40.95°	0.09	14
K[Ni(N_3S_2)] (**1**)	1.8565	1.954	2.181	2.174	~3.21	45.58°	0.09	25
Na[Ni($N_3S_2^{Me2}$)] (**2**)	1.856	1.937	2.1819	2.1582	~3.23	44.71°	0.08	24
Na[Ni($N_3S_2^{NEM}$) (**3**)	1.8644	1.9556	2.1743	2.1707	~4.50	n/a	0.14	13
Na[Ni($N_3S_2^{NMeIm}$)] (**4**)	1.854	1.950	2.169	2.174	~4.215	40.94°	0.12	TW

[a]Abbreviation: TW = this work. [b]This value represents the average of the Ni-His1N separation in the active sites of NiSOD in the reduced (His-off) state; standard deviation is 0.15 Å.

2.3.6 Electrochemistry of Ni^{2+} Complex

Cyclic voltammetry (CV) and differential pulse voltammetry (DPV) of $\mathbf{4^{Na}}$ were measured in DMF (0.25 M $^{n}Bu_4NPF_6$ electrolyte), and all potentials are reported versus and internal ferrocenium/ferrocene (Fc^+/Fc) standard. Upon scanning in the positive direction, the full CV of $\mathbf{4^{Na}}$ shows three irreversible oxidation waves (E_{ox}) at –0.52 V, 0.00 V, and +0.51 V and an

irreversible reduction wave (E_{red}) at –2.15 V (Figure 2.6). This E_{red} is primarily coupled to the E_{ox} at –0.52 V based on CV that vary the positive potential boundary to isolate which E_{ox} might correspond to E_{red} (Figure 2.S17). Based on CV of prior generations of model complexes (Table 2.3), it is most likely that the E_{ox} waves result from oxidation of the thiolate moieties of **4**. More specifically, the E_{ox} at –0.52 V is a Ni/thiolate-based feature and the E_{ox} at 0.00 V and +0.51 V are primarily ligand-based features.[13, 24-25] The E_{red} of **4** best corresponds to the irreversible disulfide to thiolate conversion of complex **2**. However, due to the more Lewis basic axial ligand of **4**, this process is more thermodynamically demanding for **4** as evidenced by the slightly more negative potential (–2.15 V) than in **2** (–1.98 V) under the same conditions.[24] However, assessing the electrochemical behavior of complex **5** will aid in confirming these assignments. Interestingly, the DPV of $\mathbf{4^{Na}}$ under the same conditions shows four E_{ox} at –0.60 V, –0.09 V, +0.27 V, and +0.47 V which each have very low intensity corresponding E_{red} waves at –0.55 V, –0.06 V, +0.27 V, and +0.46 V with two additional E_{red} at –1.37 V and –2.10 V (Figure 2.6). The low intensity of the return E_{red} waves indicates that some small portion of **4** is not irreversibly decomposed upon oxidation but is not evidence of an electrochemically reversible compound, much like prior generations of monometallic complexes from our group.

Table 2.3. Electrochemical Data of NiSOD and Select Models[a].

Complex	*E* (V vs. Fc^+/Fc)[b]	ref
$NiSOD_{red}$ (1T6U)	$E_{½}$: 0.290 (vs. NHE)[c]; $E_{½}$: –0.340[d]	37
$K[Ni(N_3S_2)]$ (**1**)	E_{ox}: –0.620; E_{red}: –1.84	25
$Na[Ni(N_3S_2^{Me2})]$ (**2**)	E_{ox}: <u>–0.670</u>; E_{red}: –1.98	24
$Na[Ni(N_3S_2^{NEM})$ (**3**)	E_{ox}: <u>–0.36</u>; E_{red}: –1.49[e]	13
$Na[Ni(N_3S_2^{NMeIm})]$ (**4**)	E_{ox}: –0.52; E_{red}: –2.15	TW

[a]TW = this work; <u>underlined potentials</u> indicate confirmed Ni/thiolate-based redox. [b]Data represents the redox potential as reported versus the ferrocenium/ferrocene (Fc^+/Fc) couple in DMF unless otherwise stated. [c]Potassium phosphate buffer (pH 7.5). [d]Redox potential normalized to *E* vs. Fc^+/Fc based on information found in ref. 39.[39] [*E* vs. Fc+/Fc = *E* vs. NHE – 0.630 V]. [e]MeOH.

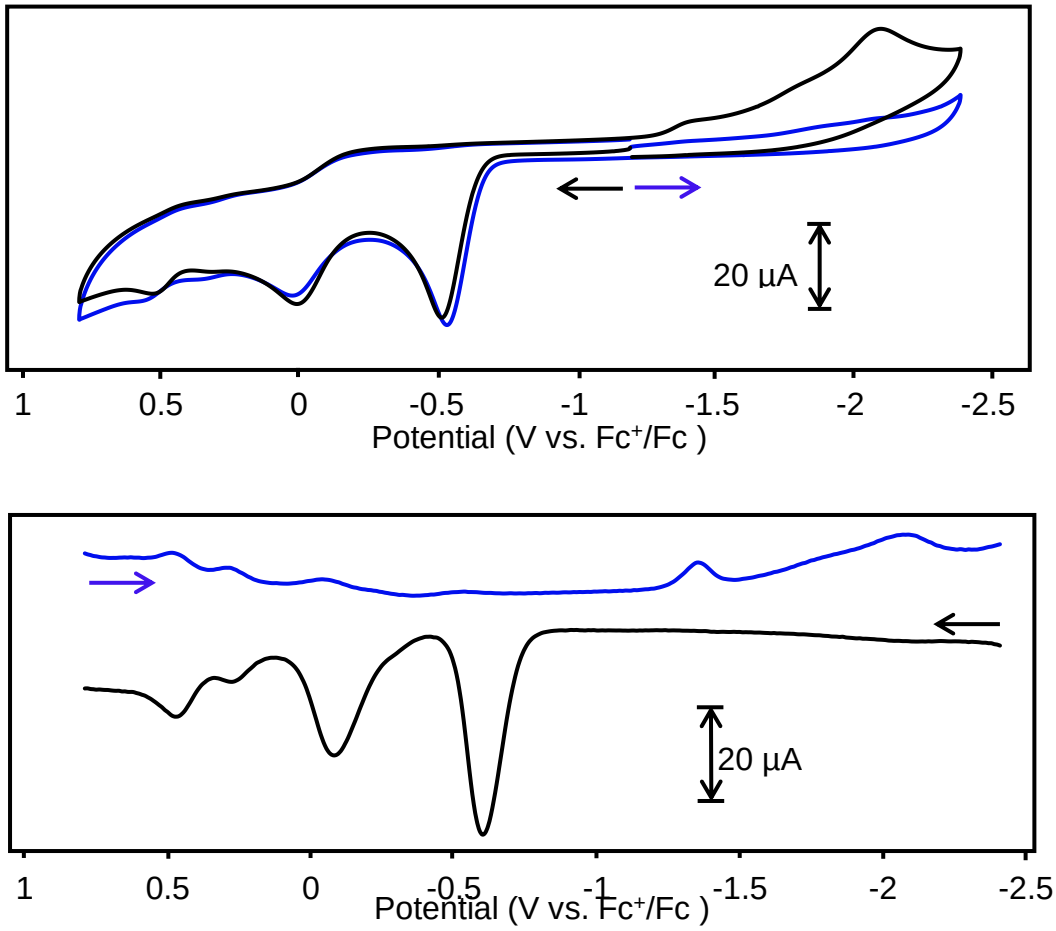

Figure 2.6. *Top*: CV of $\mathbf{4^{Na}}$ in DMF (3.14 mM) at RT (0.25 M ^{n}Bu$_4$NPF$_6$ supporting electrolyte, glassy carbon working electrode, 100 mV/s scan rate). *Bottom*: DPV of $\mathbf{4^{Na}}$ (3.14 mM) in DMF at RT (0.25 M ^{n}Bu$_4$NPF$_6$ supporting electrolyte, glassy carbon working electrode, amplitude = 50 mV, frequency = 10 Hz, E_{step} = 10 mV). Arrow indicates direction of scan.

2.3.7 Reactivity of Ni^{2+} Complex

*Air-exposure of **4***

With the broader goal of accessing Ni^{3+}, the simplest oxidation experiment was to expose a solution of **4** to air and monitor the spectral changes over time. Considering the sensitivity of thiolates to oxygen, the expectation is a quick loss of UV-vis spectral features on account of the decomposition of the complex. Alternatively, the appearance of new features from the formation of a new species could also be expected. Both results have been observed in earlier generations of model complexes, however, the behavior of **4** was unique. Solutions of $\mathbf{4^{Na}}$ in MeOH and $\mathbf{4^{Et4N}}$ in MeCN were each exposed to air for 1 min and scanned hourly for at least 8 h and then again at 2 d ($\mathbf{4^{Na}}$) and 3 d ($\mathbf{4^{Et4N}}$), and finally at 6 d ($\mathbf{4^{Na}}$) (Figure 2.7 and 2.8) with no color change detectable by the eye. For $\mathbf{4^{Na}}$, there was very little change in the UV-vis spectrum 8 h after exposure with a very slight blue-shift in the λ_{max} (454 nm shifts to 444 nm) and a very small decrease in intensity. Even after 6 days following air exposure, the λ_{max} of $\mathbf{4^{Na}}$ only blue-shifts by 20 nm (434 nm) and does not bleach like **1** and **2**, suggesting lower thiolate reactivity and therefore lower S-contribution to the HOMO of $\mathbf{4^{Na}}$. For $\mathbf{4^{Et4N}}$, the change after 9 h was more pronounced though very similar to $\mathbf{4^{Na}}$ as the λ_{max} (458 nm) was blue-shifted by 24 nm (434 nm). However, instead of decreasing in intensity over this time and these wavelengths, the λ_{max} increases in intensity by 12%, which may indicate the formation of a minor amount new species as in the case of **3** which forms a trimetallic species upon air exposure, exhibiting a much more dramatic change in the UV-vis spectrum.[13] After three days in solution, the new λ_{max} (423 nm) loses some intensity and blue-shifts further by 11 nm. After 5 days, this solution was collected and analyzed with LR-ESI-MS and found to consist primarily of $[\mathbf{4} + 2O]^-$ as well as an array of $[\mathbf{4} + nO]^-$ (n = 2-8) oxygenated species with no unoxygenated **4** (Figure 2.S30). Each experiment reveals that **4** is less susceptible to S-oxidation

and subsequent complex decomposition than prior generations of model complexes. The difference in spectral response is likely due to the different conditions of each experiment rather than the difference in counter ion. Exposure of $\mathbf{4}^{\mathbf{Na}}$ takes place in protic solvent (MeOH) which is expected to H-bond to the S atoms, sequestering electron density from the S and presumably making them less reactive than those of $\mathbf{4}^{\mathbf{Et4N}}$ in polar aprotic solvent (MeCN). With less reactive thiolates, especially in polar protic conditions like in MeOH, the electronic structure of the complex could be reasonably be expected to exhibit more Ni-character and therefore more Ni-based redox to form a Ni^{3+}. However, the axial N-donors are likely engaged in H-bonding to the bulk solvent as well, preventing them from coordinating to and stabilizing the high valent Ni^{3+} state. This is not the case for the trial of $\mathbf{4}^{\mathbf{Et4N}}$ in MeCN which may indicate the transient formation of a Ni^{3+} compound or, more likely, formation of new Ni^{2+} complex(es) such as a multimetallic species observed previously with similar compounds under the same conditions.[13]

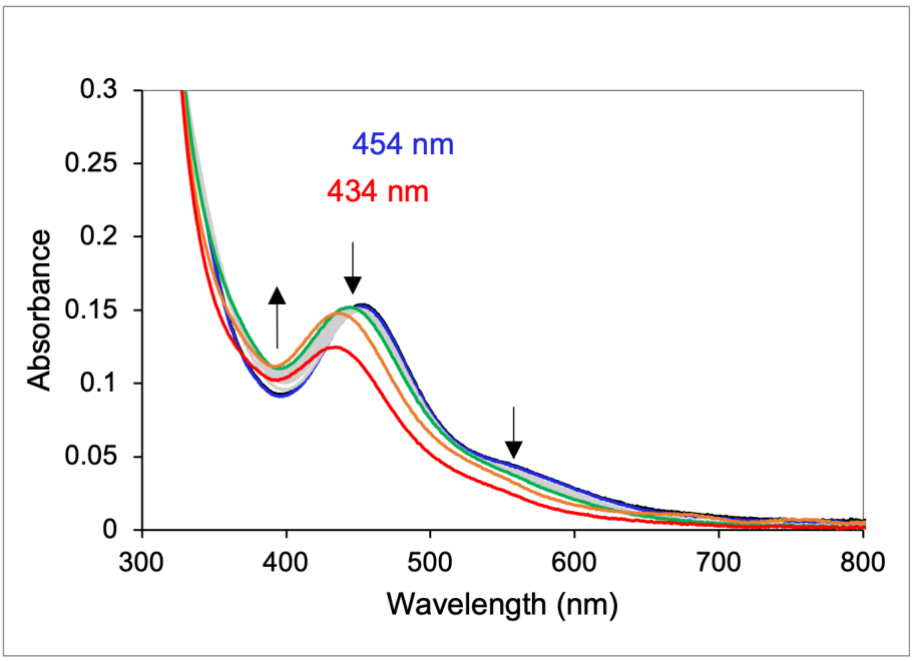

Figure 2.7. UV-vis spectrum of **Na[Ni($N_3S_2^{NMeIm}$)]** (**4^{Na}**) in MeOH at RT (black) with no change after exposed to air for 1 min (blue), scanned hourly (grey) for 9 h (green), after 2 d (orange), and again after 6 d (red). Arrows indicate spectral changes and wavelengths indicate λ_{max} at 1 min (blue) and 6 d (red) following air exposure.

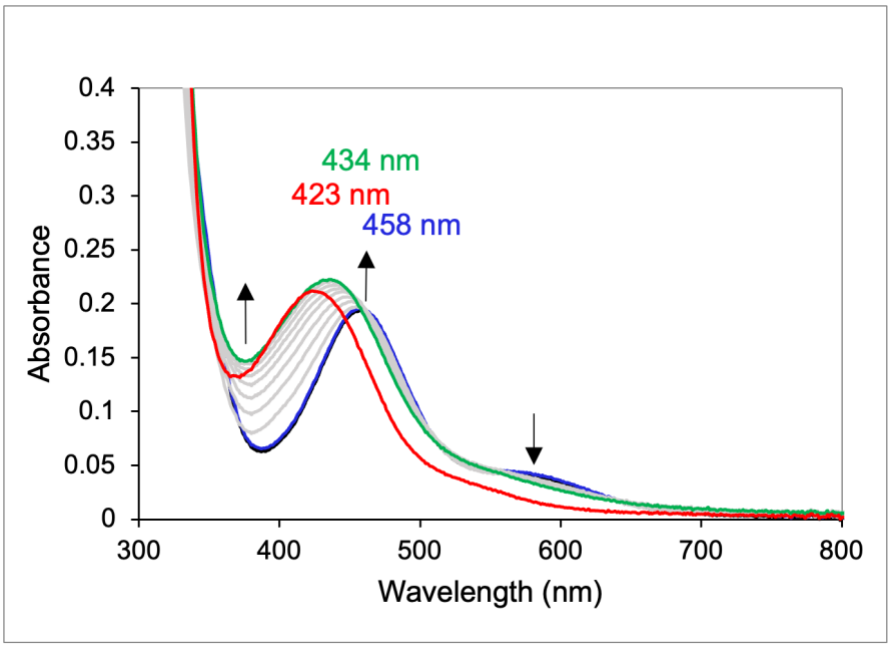

Figure 2.8. UV-vis spectrum of **Et_4N[Ni($N_3S_2^{NMeIm}$)]** (**4^{Et4N}**) in MeCN at RT (black) with no change after exposed to air for 1 min (blue), scanned hourly (grey) for 8 h (green), and after 3 d (red). Arrows indicate spectral changes and wavelengths indicate λ_{max} at 1 min (blue), 8 h (green), and 3 d (red) following air exposure.

Chemical Oxidation of $\boldsymbol{4^{Na}}$

A one-electron oxidant, ferrocenium hexafluorophosphate ($FcPF_6$), was then used to oxidize $\boldsymbol{4^{Na}}$. In a cuvette, a light brown DMF solution of $\boldsymbol{4^{Na}}$ (0.411 mM) was held at 15 ºC and to it was added an equimolar amount of $FcPF_6$ (0.411 mM). The expectation is that by conducting the reaction at a lower temperature, unstable intermediates, namely Ni^{3+}, will be stabilized well enough and long enough to be detectable as demonstrated by other low temperature studies on model complexes and NiSOD.[10, 17, 25, 34, 40] The mixture was monitored by UV-vis spectroscopy while stirring for 27.5 min. Immediately upon addition of $FcPF_6$ the absorbance across all wavelengths increased dramatically and the λ_{max} shifts from 454 nm to 417 nm (Figure 2.9). This shape reaches a maximum at 2.5 min and decreases until scans were stopped at 27.5 min. The absence of the Fc^+ peak around 619 nm indicates that all Fc^+ reacted and was reduced by $\mathbf{4^{Na}}$.[41] Overall, the loss of intensity at 454 nm (d-d band) and emergence of a new peak at 417 nm (charge-transfer band) are analogous to features in the deconvoluted UV-vis spectrum of $NiSOD_{red}$ and as-isolated NiSOD (which contains a 1:1 ratio of Ni^{2+}/Ni^{3+}) at 450 nm and 380 nm, respectively.[16]

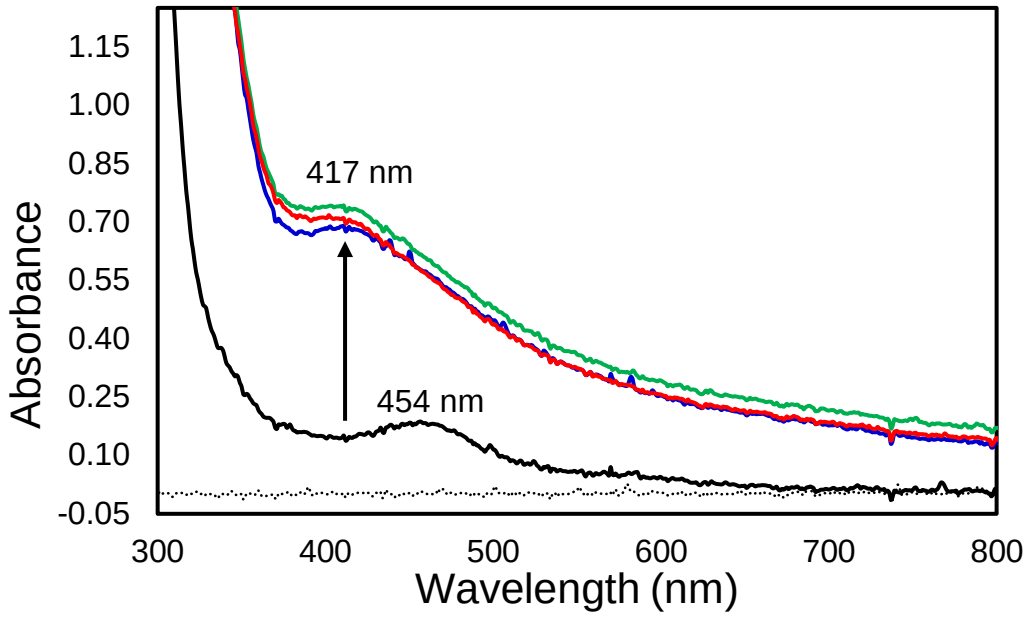

Figure 2.9. UV-vis spectrum of **Na[Ni($N_3S_2^{NMeIm}$)]** (**4^{Na}**) (0.411 mM) in DMF at 15 ºC (black) immediately following addition of $FcPF_6$ (0.411 mM) (blue), at 2.5 min (green), and at 27.5 min (red). Dotted line is DMF before addition of **4^{Na}** and $FcPF_6$. Arrow indicates spectral changes and wavelengths indicate λ_{max} of peaks below.

2.3.8 Electronic Structure Calculations

The ground state electronic structure of **4*** (* indicates DFT-optimized complex using coordinates from the X-ray structure of **4^{Na}**) was examined with DFT at the M06-L/def2-SVP level of theory. Overall, the bond distances in **4*** are in good agreement with those in the crystal structure of **4** (Figure 2.4 and S2.31).

The frontier MOs (FMOs) of **4*** reveal a highest-occupied molecular orbital (HOMO, MO 90) that is antibonding MO with 61.60% Ni- and 23.70% S-contributions (Table 2.S3). The LUMO (MO 91) is also antibonding with primary contributions from Ni and equatorial N/S donors of the ligand. While the Ni contribution in the HOMO of **4*** is very similar to those in **1***, **2***, and **3*** (62.7%, 61.9%, and 62.9% respectively), the S contribution in **4*** is higher than that of **3*** and

lower **2*** (25.9%), which is expected because of the *gem*-$(CH_3)_2$ in the α-C position of the $S_{trans\text{-}carboxamide}$ of **2***.

2.4 Conclusions

Alongside the results of prior generations of NiSOD model complexes from our group, this most recent work reveals that a square-planar Ni^{2+} model complex with a structurally accurate basal plane *and* axial donor still exhibits signs of primarily ligand-based reactivity upon oxidation.[13, 24-25] Comparison to earlier generations aids in tentative assignments of spectral features, namely electrochemical and oxidation reactivity results. The irreversible electrochemical behavior of $\mathbf{4^{Na}}$ suggests that redox activity is not solely Ni-based. Individual redox waves fall around potentials similar to those of prior models and are therefore tentatively assigned as primarily S-based events and a Ni/thiolate-based event with no evidence of a purely Ni-based redox event. These results suggest that even with the proper axial-N ligand, high valent Ni^{3+} is still not able to be stabilized. Despite this familiar S-based electrochemistry, **4** demonstrates a unique reactivity to molecular oxygen and a one-electron chemical oxidant. Complex **4** indeed becomes oxygenated, most likely at the thiolates, however, this does not seem to prompt complete decomposition of **4**, evidenced by the shifted but steady UV-vis spectra for days after air exposure. Considering the electrochemical results of $\mathbf{4^{Na}}$, it is unlikely that these new peaks originate from a Ni^{3+} species. However, it is possible that the new and apparently stable chromophore formed in the air-exposure experiments is $[\mathbf{5} + 2O]^-$ (the main ion peak in the MS of an air exposed solution of $\mathbf{4^{Et4N}}$ after 5 days in solution). It cannot yet be ruled out that these peaks might also indicate the formation of one or more multimetallic species as has occurred with **3**. However, there are no signs of such species according to MS results. Regardless of the exact identity of the oxidation products,

the resistance to decomposition (i.e. bleaching) of these species may indicate a high degree of covalency between Ni and S, a lower S-contribution to the HOMO of **4**, or even Ni-N_{axial} binding, all of which is also true of NiSOD.[16] Not only does $\mathbf{4^{Na}}$ display exceptional integrity in the presence of oxidants but the specific pattern of loss and emergence of peaks similar $NiSOD_{red}$ and $NiSOD_{ox}$, respectively, upon chemical oxidation reflects a similarity in electronic structure to NiSOD. So, despite the lack of reversible electrochemistry and identical UV-vis features to that of $NiSOD_{ox}$, these results suggest that the incorporation of an appropriately Lewis basic and stronger field axial-N donor produces a model complex with reactivity that more closely resembles that of NiSOD. These results also emphasize the essential role of the secondary sphere of the native enzyme in arranging the active site appropriately and support mutagenic and theoretical biochemical works that conclude the same.[16, 20-21] RT experiments monitored by UV-vis and NMR may also provide more insight into the species forming during the reactivity studies discussed in this work. Further oxidation experiments at low temperatures will be essential to capture unstable Ni^{3+} and visualize it with electron paramagnetic resonance (EPR) spectroscopy.

2.5 Materials and Methods

2.5.1 General Information

All reagents were purchased from commercial suppliers and used as received unless otherwise noted. Acetonitrile (MeCN), methylene chloride (CH_2Cl_2), tetrahydrofuran (THF), diethyl ether (Et_2O), and pentane were purified by passage through activated alumina columns using an MBraun MB-SPS solvent purification system and stored over 4 Å molecular sieves under an N_2 atmosphere before use. *N*,*N*-dimethylformamide (DMF) was purified with a VAC Solvent Purifier containing 4 Å molecular sieves and stored under similar conditions. Methanol (MeOH)

was stored over 3 Å molecular sieves for at least 1 week before using. The compounds *S*-tritylcysteamine,[42] 2-bromo-*N*-(2-(tritylthio)ethyl)acetamide,[43] N-(2-(tritylthio)ethyl)-2-((2-(tritylthio)ethyl)amino)acetamide[43], and 2-(chloromethyl)-1-methyl-1*H*-imidazole hydrochloride (NMeImCl•HCl)[44] were prepared and checked according to the published procedures. All complex synthesies were performed under an inert atmosphere of N_2 using standard Schlenk techniques or in an MBraun Unilab glovebox under an atmosphere of purified N_2.

2.5.2 Physical Methods

FTIR spectra were collected on a ThermoNicolet 6700 spectrophotometer running the OMNIC software, where samples were prepared as pressed KBr pellets. Electronic absorption spectra were recorded at 25 °C using a Cary-50 spectrophotometer containing a Quantum Northwest TC 125 temperature control unit. All UV–vis samples were prepared in gastight Teflon-lined screw-cap quartz cells with an optical pathlength of 1 cm. Cyclic voltammetry (CV) measurements were performed with a WaveDriver 40 Bipotentiostat/Galvanostat from Pine Research Instrumentation using an Ag/Ag+ reference electrode, Pt wire counter electrode, and a stationary glassy-carbon working electrode (3 mm diameter). Measurements were performed at ambient temperature using 1-3 mM analyte in the appropriate solvent under Ar containing 0.25 M $^{n}Bu_4NPF_6$ as the supporting electrolyte. Analyte potentials were referenced against a ferrocene internal standard under identical conditions, where $E_{1/2}$ = 0.403 V in DMF vs the reported nonaqueous Ag wire reference electrode. Low-resolution electrospray ionization mass spectrometry (LR- ESI-MS) data were collected using a PerkinElmer Sciex API I Plus quadrupole mass spectrometer or a Bruker Esquire 3000 plus ion trap mass spectrometer Elemental microanalysis for C, H, and N was performed by Midwest Microlab in Indianapolis, IN. 1D NMR

spectra were recorded in the listed deuterated solvent on a 400 MHz Bruker BZH 400/52 NMR spectrometer at RT with chemical shifts referenced to tetramethylsilane (TMS) or the residual protio signal of the deuterated solvent.[45] 2D NMR spectra (COSY, HSQC, and ROESY) were performed either on the 400 MHz Bruker BZH 400/52 NMR spectrometer or on the 500 MHz Varian Inova wide-bore NMR spectrometer at RT.

2.5.3 Synthesis and Characterization

The synthesis of the ligand N-(2-mercaptoethyl)-2-((2-mercaptoethyl)((1-methyl-1H-imidazol-2-yl)methyl)amino)acetamide (***$H_3N_3S_2^{NMeIm}$•2HCl***) is comprised of the following two steps.

*Step 1: 2-(((1-methyl-1*H*-imidazol-2-yl)methyl)(2-(tritylthio)ethyl)amino)-N-(2-(tritylthio)ethyl)acetamide (***$N_3S_2^{NMeIm}Tr_2$***)*

To a slightly cloudy, yellow solution of NMeImCl•HCl (0.1985 g, 1.520 mmol) in 20 mL THF/MeCN (1:1) was added 1 equiv of NaI (0.2309 g, 1.541 mmol). The mixture was allowed to react for 15 min at which point 3 equiv of K_2CO_3 (0.6337 g, 4.585 mmol) and 1 equiv of $N_2S_2Tr_2$ (1.0314 g, 1.5191 mmol) were added. The light-yellow mixture was refluxed for 23 h, yielding a light-brown slurry. The solvent was concentrated by vacuum distillation to yield a light-brown foam. To the foam was added 100 mL of CH_2Cl_2 and the mixture was then washed with 100 mL of satd. $NaHCO_3$ solution and 100 mL of satd. NaCl. The CH_2Cl_2-soluble portion was dried over $MgSO_4$ and gravity filtered. The CH_2Cl_2 was removed by rotary evaporation to yield a light brown foam (1.0988 g, 89% recovery). Crude material from multiple syntheses (6.2104 g) was purified by column chromatography using SiO_2 and a mobile phase of 4% MeOH in CH_2Cl_2. The desired

product fractions (R_f = 0.27) were collected, dried over $MgSO_4$, concentrated, and dried on a vacuum line to yield an off-white foam (2.4597 g, 3.182 mmol, 37% yield when all equiv of limiting reagent that make up this crude batch are taken into account). mp 63-65 °C. ^{1}H NMR (400 MHz $CDCl_3$ with 0.05% v/v TMS, δ from TMS): 7.36-7.23 (m, 38H, integrates higher than expected due to overlap with residual $CHCl_3$), 7.18 (t, 1H, N*H*), 6.87 (d, 1H, Im-C*H*), 6.84 (d, 1H, Im-*CH'*), 3.51 (s, 2H, Im-CH_2), 3.47 (s, 3H, Im-CH_3), 2.99 (q, 2H), 2.95 (s, 2H), 2.53 (t, 2H), 2.32 (q, 4H). ^{13}C NMR (101 MHz, CDCl3 with 0.05% v/v TMS, δ from solvent signal): 170.27 (*C*═O), 144.81, 144.09, 129.66, 128.06, 127.60, 126.90, 121.90, 66.76, 54.77, 50.24 37.76, 33.15, 32.21, 30.05. FTIR (KBr pellet) ν_{max} (cm^{-1}): 3378 (br w, ν_{NH}), 3054 (w), 3028 (w), 2924 (w), 2865 (w), 1955-1720 (w, arom overtones) 1675 (s, ν_{CO}), 1594 (w), 1488 (s), 1489 (m), 1443 (m), 1384 (w), 1360 (w), 1282 (w), 1183 (w), 1082 (w), 1033 (m), 1001 (w), 973 (w), 908 (w), 850 (w), 801 (w), 743 (vs), 700 (vs), 675 (m), 629 (w), 620 (m), 506 (w). LR-ESI-MS (*m*/z): $[M + H]^+$calcd for $C_{49}H_{49}N_4OS_2$, 773.3, 774.3, 775.3, 776.3; found, 773.3, 774.3, 775.3, 776.3.

*Step 2: N-(2-mercaptoethyl)-2-((2-mercaptoethyl)((1-methyl-1*H*-imidazol-2-yl)methyl)amino)acetamide dihydrochloride (**$H_3N_3S_2^{NMeIm}$•2HCl**)*

To a clear gold/orange 20 mL neat TFA soln of $N_3S_2^{NMeIm}Tr_2$ (1.0108 g, 1.3075 mmol) under positive N_2 pressure was added 3.557 mol-equiv of triethylsilane (0.5408 g, 4.651 mmol). Immediately, the solution became colorless and a white solid precipitated out, and after 15 min became a white slurry. The slurry was concentrated slightly then stored at 4 ºC for 15 minutes. The slurry was filtered yielding a white solid (triphenylmethane). The pale-yellow filtrate was then concentrated to a clear gold oil using a shortpath distillation unit. The oil was then stirred with pentane and decanted (2 mL x 10) and dried to remove excess triphenylmethane. In a slow

dropwise fashion, 5 equiv. of 1M HCl•Et_2O (6.60 mL, 6.60 mmol) was added to the gold oil resulting in a mixture of white solid and oil. This mixture was stirred for 20 min and then scraped into a homogenous slurry. This slurry was then filtered, rinsed with Et_2O, and dried over vacuum to yield a white powder (483.1 mg, 1.337 mmol, 102% yield). ^{1}H NMR (400 MHz CD_3OD, δ from protio signal): 7.57 and 7.53 (dd, 1H and 1H, Im-C*H*), 4.53 (s, 2H, Im-C*H*$_2$), 3.92 (s, 3H, Im-C*H*$_3$), 3.76 (s, 2H, O=C-C*H*$_2$), 3.28 (t, 2H), 3.16 (t, 2H), 2.73 (t, 2H), 2.53 (t, 2H). ^{13}C NMR (101 MHz, CD_3OD, δ from solvent signal): 207.61 (*C*═O), 169.06, 141.70, 126.45, 120.66, 59.59, 53.58, 43.80, 35.80, 24.43, 20.79. FTIR (KBr pellet), ν_{max} (cm^{-1}): 3213 (br m, ν_{NH}), 3140 (br, m), 3063 (br, m), 2945 (m), 2773 (m), 2505 (br m, ν_{SH}), 1783 (w), 1681 (s, ν_{CO}), 1599 (m), 1564 (m), 1557 (m), 1532 (m), 1446 (m), 1404 (m), 1368 (w), 1280 (w), 1204 (m), 1168 (s), 808 (w), 765 (m), 720 (w), 693 (m), 648 (w), 587 (w), 449 (w). LR-ESI-MS (*m*/*z*): $[M + H]^+$ calcd for $C_{11}H_{21}N_4OS_2$, 289.2, 290.2, 291.2; found, 289.1.9, 290.1, 291.1.

Na[Ni($N_3S_2^{NMeIm}$)] ***(4^{Na})***

To a yellow MeOH solution (4 mL) of $H_3N_3S_2^{NMeIm}$•2HCl (373.3 mg, 1.034 mmol) was added 5 mol-equiv of Na^0 (112.9 mg, 4.91 mmol, 4.75 equiv) in 1 mL MeOH which bubbled for ~1 min. After stirring this mixture at RT for 10 min, 2 mL of a green MeOH soln of $NiCl_2$ (120.3 mg, 0.9283 mmol, 0.8978 equiv.) was added dropwise over a few seconds to immediately yield a dark brown solution. After stirring at RT for 1 h, the mixture was stored at -25 °C for 1.5 h then filtered over Celite to remove the white (NaCl) solid. The brown filtrate was concentrated to 2 mL, stored at -25 ºC for 30 min, then filtered again over Celite to remove remaining NaCl. The brown filtrate was concentrated to dryness. The brown residue was then scraped down in Et_2O and the resulting solid was collected and dried via vacuum filtration to yield a light brown powder (394.9 mg, 1.076 mmol, 116% likely due to excess NaCl). ^{1}H NMR (400 MHz, CD_3OD, δ from protio solvent): 7.09 (s, 1H), 6.84 (s, 1H), 4.70 (s, 3H), 4.49 (d, 1H), 3.51 (m, 1H), 3.48 (d, 1H), 3.37 (s, 1H), 2.95 (broad, m, 4H), 2.48 (broad, m, 1H), 2.42 (m, 2H), 1.97 (broad, m, 4H), 1.84 (s, 1H). ^{1}H NMR (500 MHz, D_2O, δ from protio solvent): 7.27 (s, 1H), 6.99 (s, 1H,), 4.93 (s, 3H), 4.51 (d, 2H), 3.80 (m, 2H), 3.65 (d, 2H), 3.42 (d, 1H), 3.11 (broad, m, 2H), 2.84 (broad, t, 1H), 2.62 (broad, t, 1H), 2.38 (m, 1H), 2.27 (broad, d, 1H), 2.12 (s, 1H), 2.06 (s, 1H). FTIR (KBr pellet), ν_{max} (cm^{-1}): 3433 (br w, ν_{OH} from H_2O), 2929 (w), 2843 (m), 1685 (w), 1595 (vs, ν_{CO}), 1496 (w), 1414 (w), 1284 (vw), 1206 (w), 1087 (w), 1034 (w), 844 (w), 821 (w), 762 (w), 572 (w), 574 (vw), 465 (w). UV–vis (MeOH, RT), λ_{max}, nm: 454, 565 (sh). LR-ESI-MS (*m*/*z*): $[M - Na]^-$ calcd for $C_{11}H_{17}N_4NiOS_2$, 343.0, 344.0, 345.0, 346.0, 347.0; found, 343.0, 344.0, 344.9, 345.9, 346.9. Anal. Calcd for $C_{11}H_{17}N_4NiOS_2Na \cdot 1.2H_2O$: C, 33.99; H, 5.03; N, 14.41. Found: C, 33.80; H, 4.92; N 14.11.

*$Et_4N[Ni(N_3S_2^{NMeIm})]$ (**4^{Et4N}**)*

To a 1 mL slurry of $Na[Ni(N_3S_2^{NMeIm})]$ (162.7 mg, 0.4432 mmol) in MeCN was added Et_4NCl (82.7 mg, 0.487 mmol) as a 1 mL aliquot. Within 1 min of addition, the soln began to turn deep brown. An additional 5 mL MeCN was added before stirring the mixture at RT for 1 h. Over this time, the brown insolubles dissolved and pale insolubles emerged. The slurry was then vacuum filtered over Celite yielding light brown insolubles with the Celite and a deep brown filtrate. The filtrate was concentrated to a brown, oily foam and was scraped down in Et_2O. The slurry was filtered and dried, yielding a light brown solid (195.3 mg, 0.4083 mmol, 92% yield). ^{1}H NMR (400 MHz, CD_3CN δ from protio solvent): 6.99 (s, 1H, Im-C*H*), 6.84 (s, 1H, Im-C*H'*), 4.52 and 3.89 (dd, 1H and 1H), 4.28 (s, 3H, Im-CH_3), 3.19 (m, 10H, Et_4NCl-CH_2, some excess), 3.11 (m, 3H), 2.93 (t, 1H), 2.72 (s, 1H), 2.44 (s, 3H), 1.22 (s, 15H, Et_4NCl-CH_3, some excess). ^{13}C NMR (101 MHz, CD_3CN, δ from solvent signal): 174.41 (*C*═O), 141.83, 128.18, 122.93, 65.46, 64.90, 53.01, 52.98, 49.96, 49.37, 34.67, 26.25, 7.67. FTIR (KBr pellet), ν_{max} (cm^{-1}): 3400 (br w, ν_{OH} from H_2O), 2941 (m), 2929 (m), 2832 (m), 1600 (vs, ν_{CO}), 1521 (vw), 1508 (vw), 1458 (m), 1399 (m), 1321 (vw), 1260 (w), 1183 (w), 1086 (w), 1028 (w), 795 (w), 755 (vw), 445 (w). UV–vis (MeCN, RT), λ_{max}, nm: 458, 485 (sh). LR-ESI-MS (*m*/*z*): $[M - Et_4N]^-$ calcd for $C_{11}H_{17}N_4NiOS_2$, 343.0, 344.0, 345.0, 346.0, 347.0; found, 343.1, 344.1, 345.1, 346.1, 347.1. $[Et_4N]^+$ calcd for $C_8H_{20}N$, 130.2, 131.2; found 130.1, 131.2.

*$Na[Zn(N_3S_2^{NMeIm})]$ (**5**)*

To a yellow MeOH solution (1 mL) of $H_3N_3S_2^{NMeIm}$•2HCl (69.5 mg, 0.192 mmol) was added 5 mol-equiv of Na^0 (24.1 mg, 1.06 mmol) in 1 mL MeOH which bubbled for ~1 min. Upon addition of Na^0, white insolubles immediately form. After stirring this mixture at RT for 10 min,

0.5 mL of a MeOH soln of $ZnCl_2$ (23.0 mg, 0.169 mmol, 0.877 equiv.) was added dropwise over a few seconds with no change in color. After stirring at RT for 1 h, the mixture was stored at -25 °C for 3 h then filtered over Celite to remove the white (NaCl) solid. The yellow filtrate was concentrated to 2 mL, stored at 25 ºC for 1 h min, then filtered again over Celite to remove remaining NaCl. The yellow filtrate was then concentrated to dryness and scraped down in Et_2O. The resulting solid was collected and dried via vacuum filtration to yield an off-white powder (97.4 mg, 0.261 mmol, 135% yield). All Celite was then collected, stirred in MeOH, filtered, added back to the pale-yellow solid, and dried once again. To the resulting off-white solid was added 3 mL *i*PrOH and 0.5 mL MeOH dropwise to dissolve all solids. This mixture was kept at –25 ºC for 7 h and then filtered over Celite, rinsing with cold 1:6 MeOH/*i*PrOH. The solid collected on top of the Celite was off-white-colored (59.4 mg, 1.02 mmol, 120% yield NaCl), leaving a pale-yellow filtrate which was dried to an off-white solid. This solid was scraped down in Et_2O, filtered over a fritted funnel, and dried to yield an off-white solid (57.7mg, 0.1543 mmol, 80% yield). ^{1}H NMR (400 MHz, CD_3OD, δ from protio solvent): 7.15 (br s, 2H), 7.03 (br m, 2H), 6.81 (m, 1H), 3.77 (m, 6H), 3.59 (br s, 7), 3.13 (br s, 3H), 3.01 (br s, 3H), 1.84 (m, 1H). Splittings and integrations are challenging, see Figure 2.S25. ^{13}C NMR (101 MHz, CD_3OD, δ from solvent signal): 170.48 (*C*═O), 146.23, 127.40, 123.64, 64.68, 25.31, 24.27, 15.47. FTIR (KBr pellet), ν_{max} (cm^{-1}): 3400 (br w, ν_{OH} from H_2O), 3111 (w), 2839 (w), 1669 (w), 1587 (vs, ν_{CO}), 1507 (w), 1441 (m), 1401 (m), 1337 (w), 1283 (w), 1206 (w), 1160 (w), 1130 (m), 1088 (w), 972 (w), 801 (vw), 743 (s), 671 (vw). LR-ESI-MS (*m*/*z*): $[M - Na]^-$ calcd for $C_{11}H_{17}N_4ZnOS_2$, 349.0, 350.0, 351.0, 352.0, 353.0, 354.0, 355.0; found, 349.1, 350.1, 351.1, 352.1, 353.2, 354.2, 355.2.

2.5.4 Reactivity Studies

Air Oxidation of $\boldsymbol{4^{Na}}$

At RT, a cuvette of $\mathbf{4^{Na}}$ in MeOH was exposed to ambient air for 1 min, then closed back up. The solution was monitored by UV-vis and scans were collected hourly for 9 hours followed by additional scans at 2 d and 6 d after exposure.

Air Oxidation of $\boldsymbol{4^{Et4N}}$

At RT, a cuvette of $\mathbf{4^{Et4N}}$ in MeCN was exposed to ambient air for 1 min then closed back up. The solution was monitored by UV-vis and scans were collected hourly for 8 hours followed by an additional scan at 3 d after exposure. LR-ESI-MS was collected 5 d following exposure.

Low-Temperature Chemical Oxidation of $\boldsymbol{4^{Na}}$

A cuvette of $\boldsymbol{4^{Na}}$ in DMF (0.411 mM) was held at 15 ºC. While stirring, 1 equiv of $FcPF_6$ (0.411 mM) was added via gas-tight syringe. The solution was monitored by UV-vis and scanned every 6 s for 2.5 min then every 2 min for the following 27.5 min, for a total of 30 min.

2.5.5 Computational Details

Density functional theory (DFT) calculations were performed with the ORCA electronic structure package, version 4.2.1.[46] Geometry optimization and single-point energy analyses were performed using the M06-L functional[47] and Grimme's D30 dispersion correction[48] with coordinates from the crystal structure of $\mathbf{4^{Na}}$. The triple-ζ basis set def2-SVP[49] was used for geometry optimization and frequency analysis with an def2/J auxiliary basis set on all atoms.[50] No imaginary frequencies were found.

2.5.6 X-Ray Crystallographic Data Collection and Structure Solution Refinement

Orange block crystals of $\mathbf{4^{Na}}$ were obtained from slow diffusion of Et_2O into a saturated solution of $\mathbf{4^{Na}}$ in MeOH stored at -25 ºC for nine days. X-ray intensity data were measured at 170 K on a Bruker D8 Quest PHOTON II diffractometer system Mo Kα radiation (λ = 0.71076 Å). The data were corrected for Lorentz and polarization effects and integrated with the manufacturer's SAINT V8.40B software. Absorption corrections were applied with the program SADABS 2016/2.[51] Subsequent solution and refinement was performed using the SHELXL 2018/3 package.[51]

2.6 Supporting Information

2.6.1 Characterization

Figures

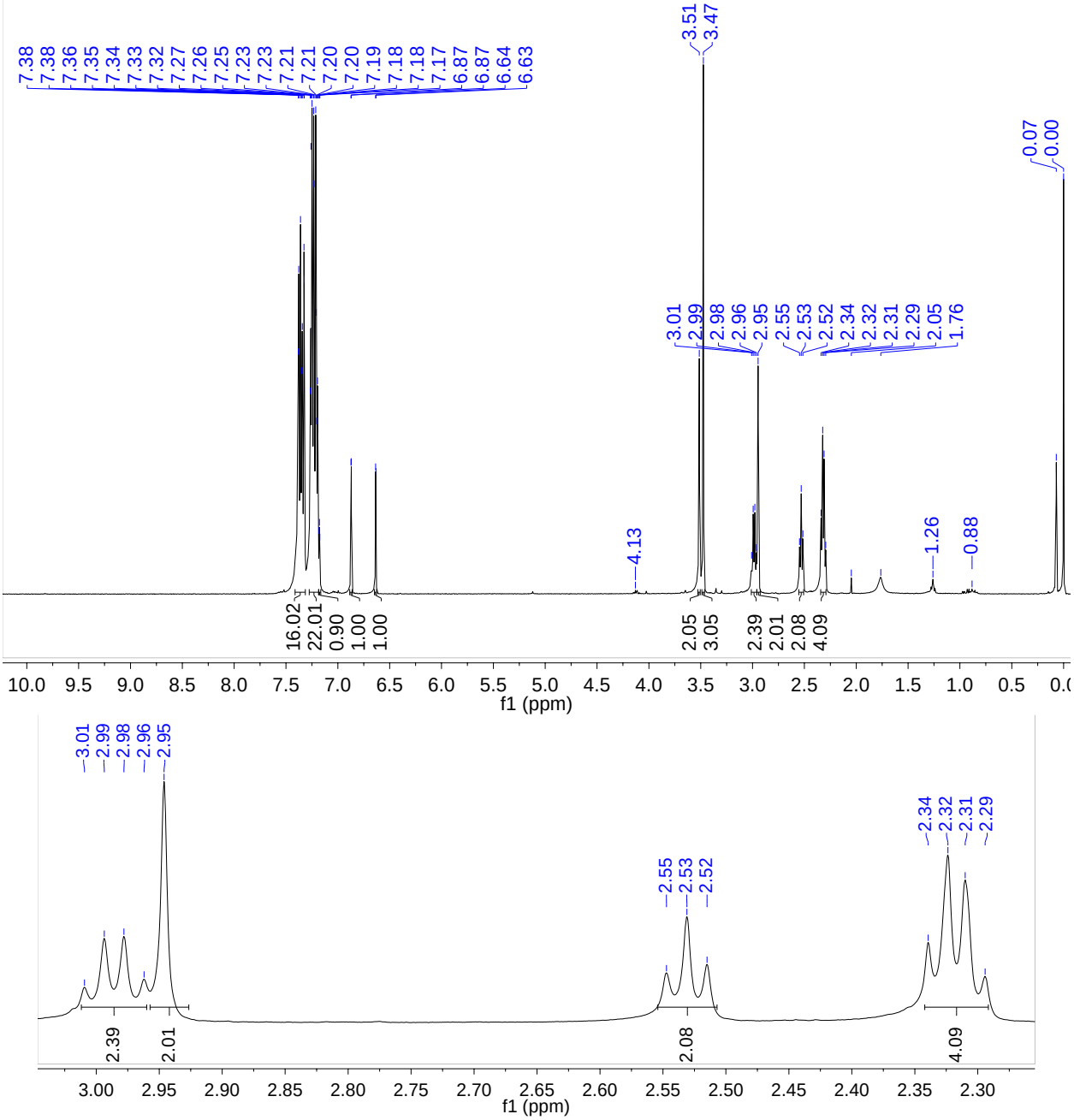

Figure 2.S1: ^{1}H NMR of $\mathbf{N_3S_2^{NMeIm}Tr_2}$ (400 MHz, $CDCl_3$ with 0.05% v/v TMS, RT, δ from TMS). Minor amounts of grease (0.07 ppm), hexane (0.88 ppm), and EtOAc (1.26, 4.12 ppm) from work-up. HDO from solvent (1.76 ppm). *Top*- full spectrum. *Bottom*- expansion of 2.3-3.0 ppm.

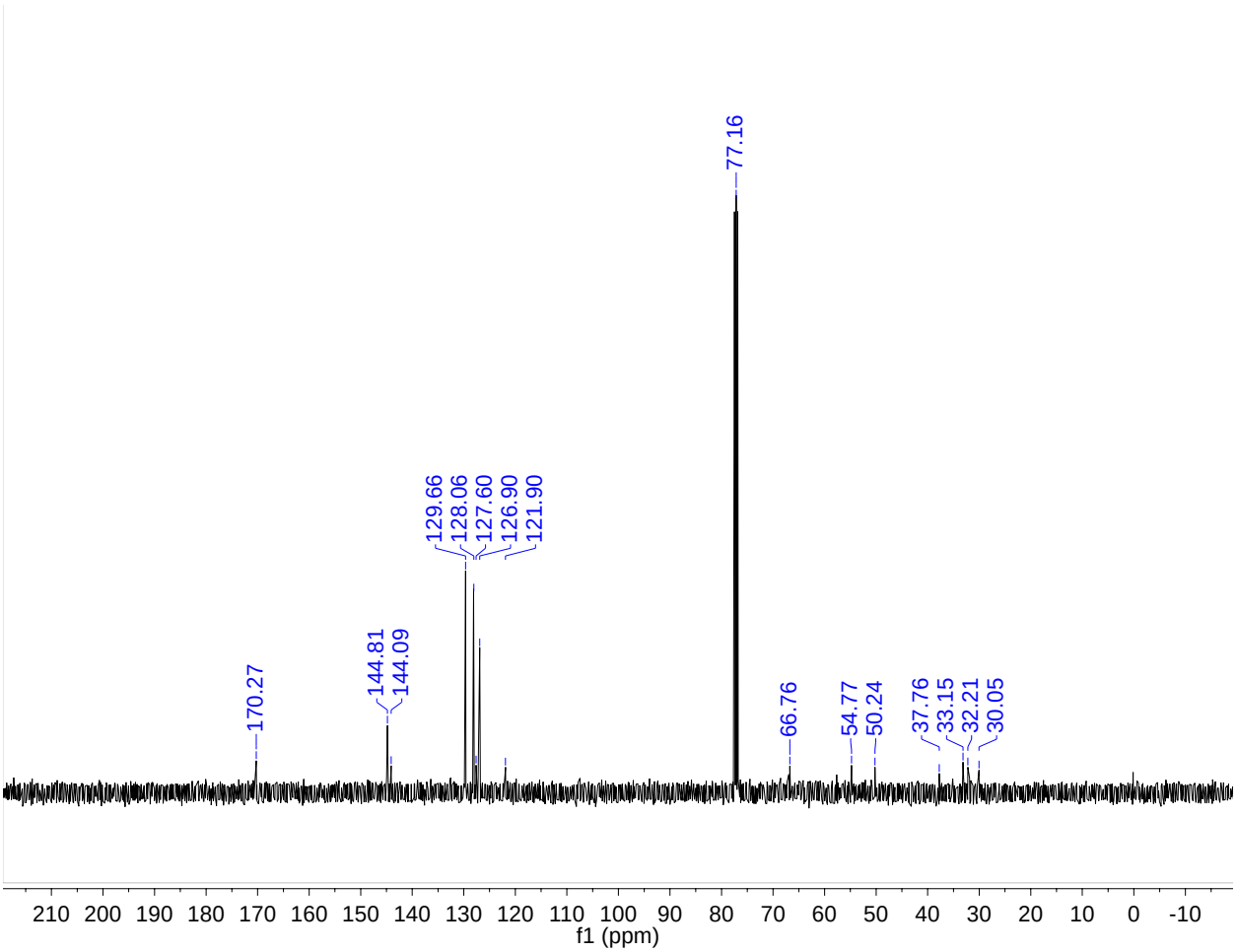

Figure 2.S2: ^{13}C NMR of $\mathbf{N_3S_2^{NMeIm}Tr_2}$ (101 MHz, $CDCl_3$). Solvent peak is referenced to 77.16 ppm.

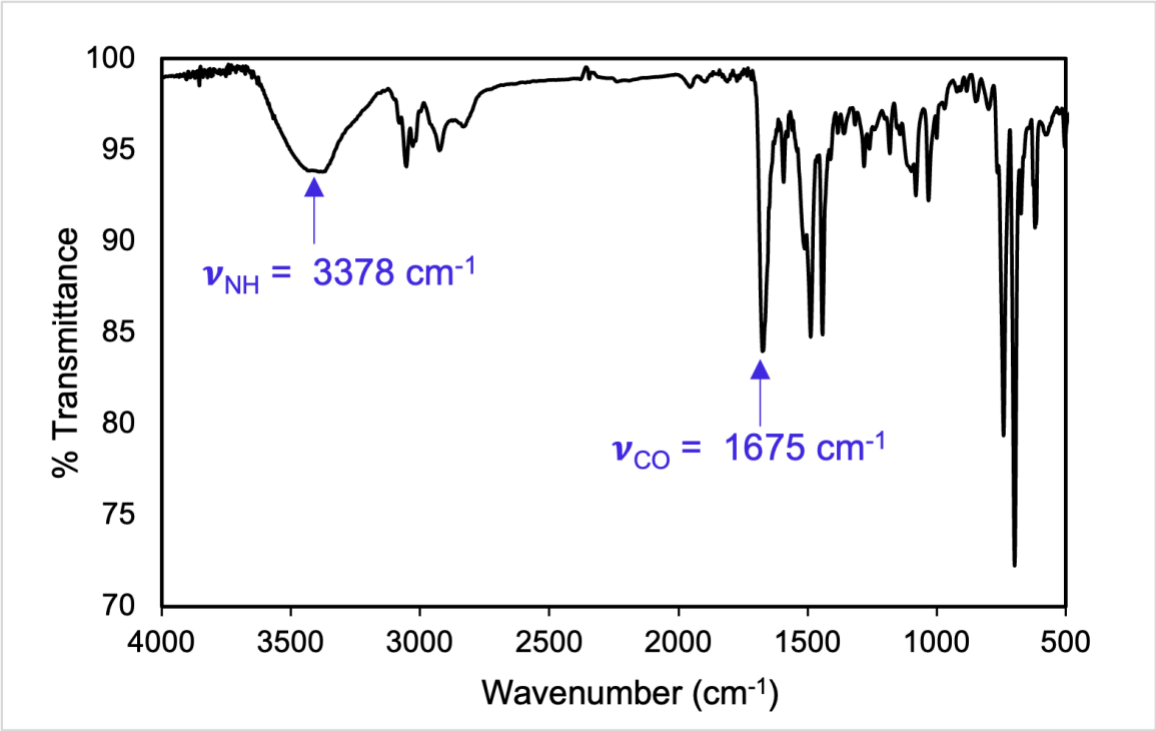

Figure 2.S3: Solid-state FTIR spectrum of $\mathbf{N_3S_2^{NMeIm}Tr_2}$ in a KBr matrix at RT.

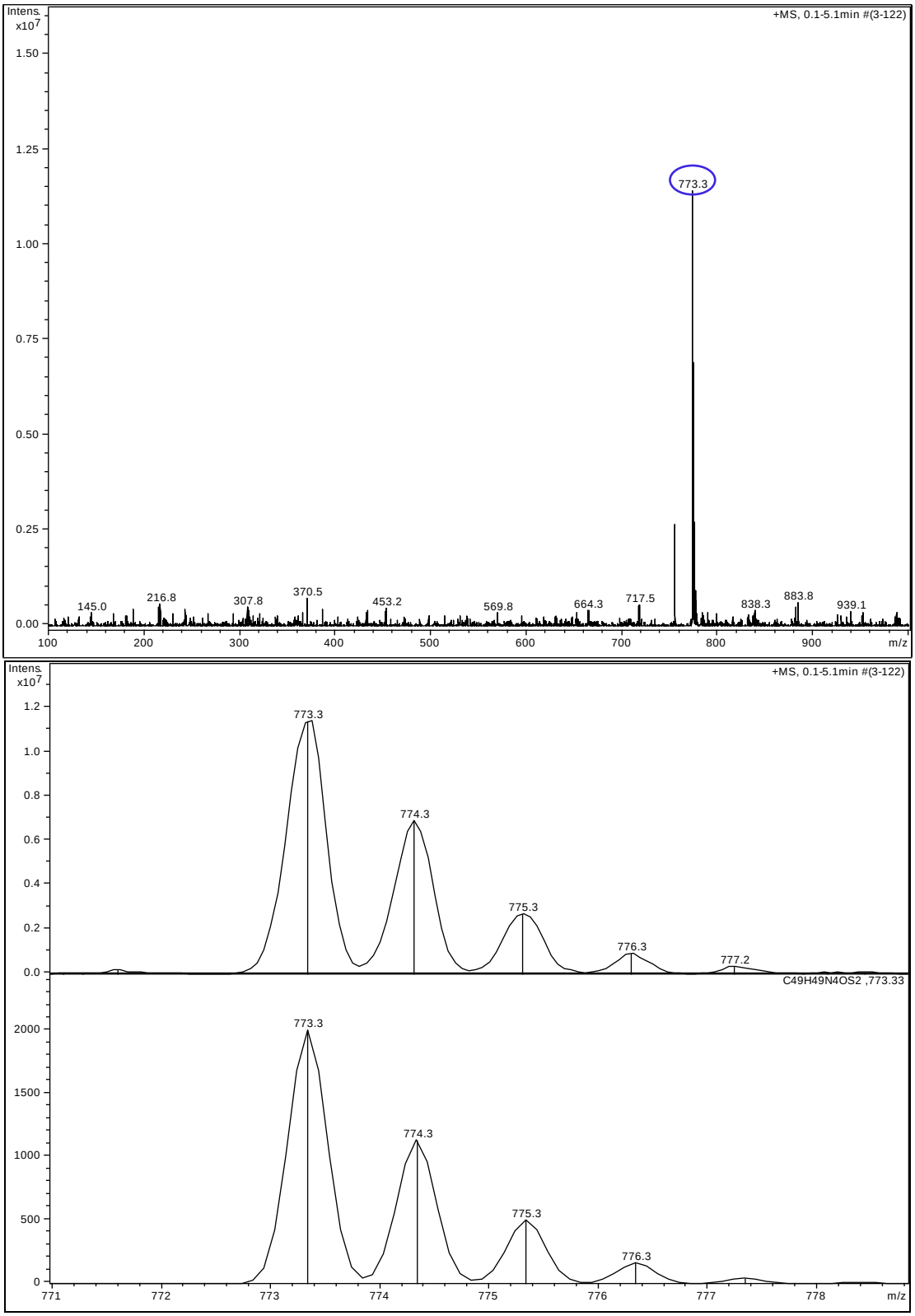

Figure 2.S4: *Top*: LR-ESI-MS(+) of **$N_3S_2^{NMeIm}Tr_2$** in CH_2Cl_2. *Bottom*: experimental (top) versus theoretical (bottom) isotopic distribution of $[N_3S_2^{NMeIm}Tr_2+H]^+$.

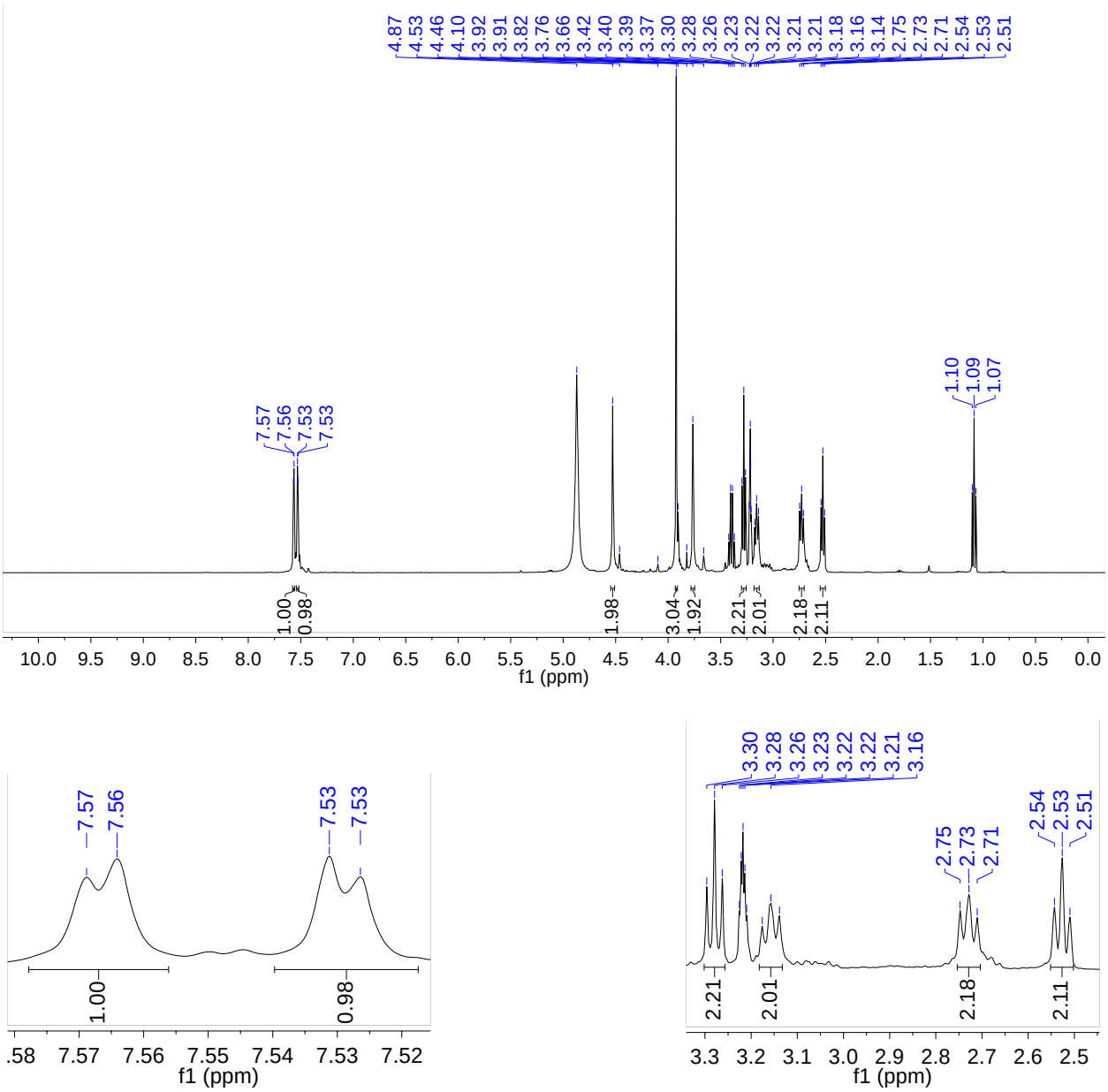

Figure 2.S5: ^{1}H NMR of **$H_3N_3S_2^{NMeIm}$•2HCl** (400 MHz, CD_3OD, δ from protio solvent). Minor amounts of Et_2O (1.09, 3.40 ppm) from work-up and residual protio solvent (3.22, 4.87 ppm). *Top*- full spectrum. *Bottom*- expansion of aromatic (left) and aliphatic (right) regions.

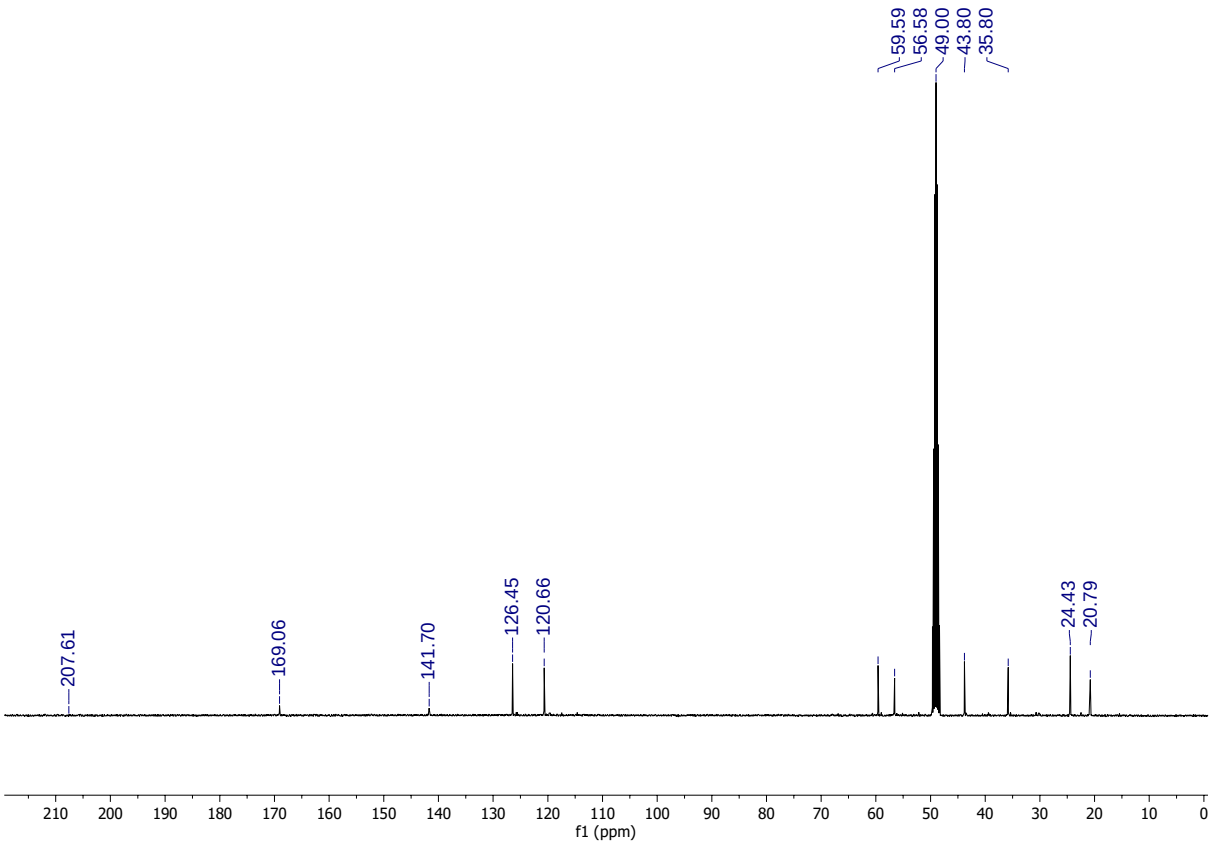

Figure 2.S6: ^{13}C NMR of **$H_3N_3S_2^{NMeIm}$•2HCl** (101 MHz, CD_3OD). Solvent peak is referenced to 49.00 ppm.

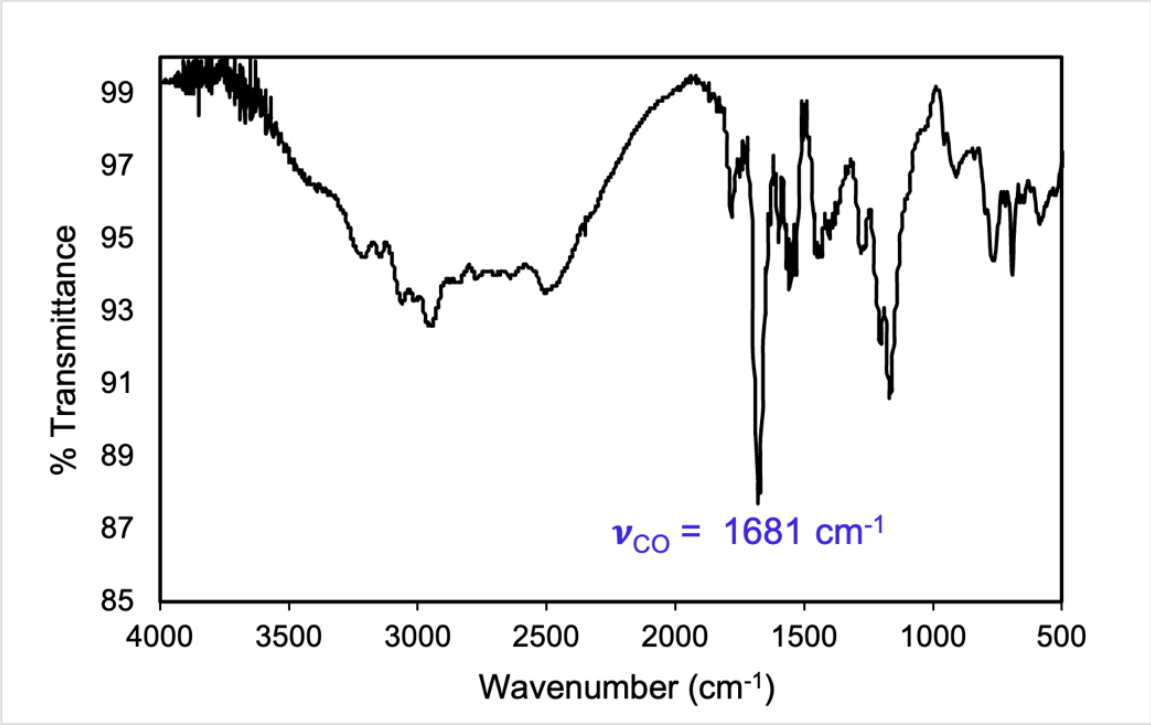

Figure 2.S7: Solid-state FTIR spectrum of **$H_3N_3S_2^{NMeIm}$•2HCl** in a KBr matrix at RT.

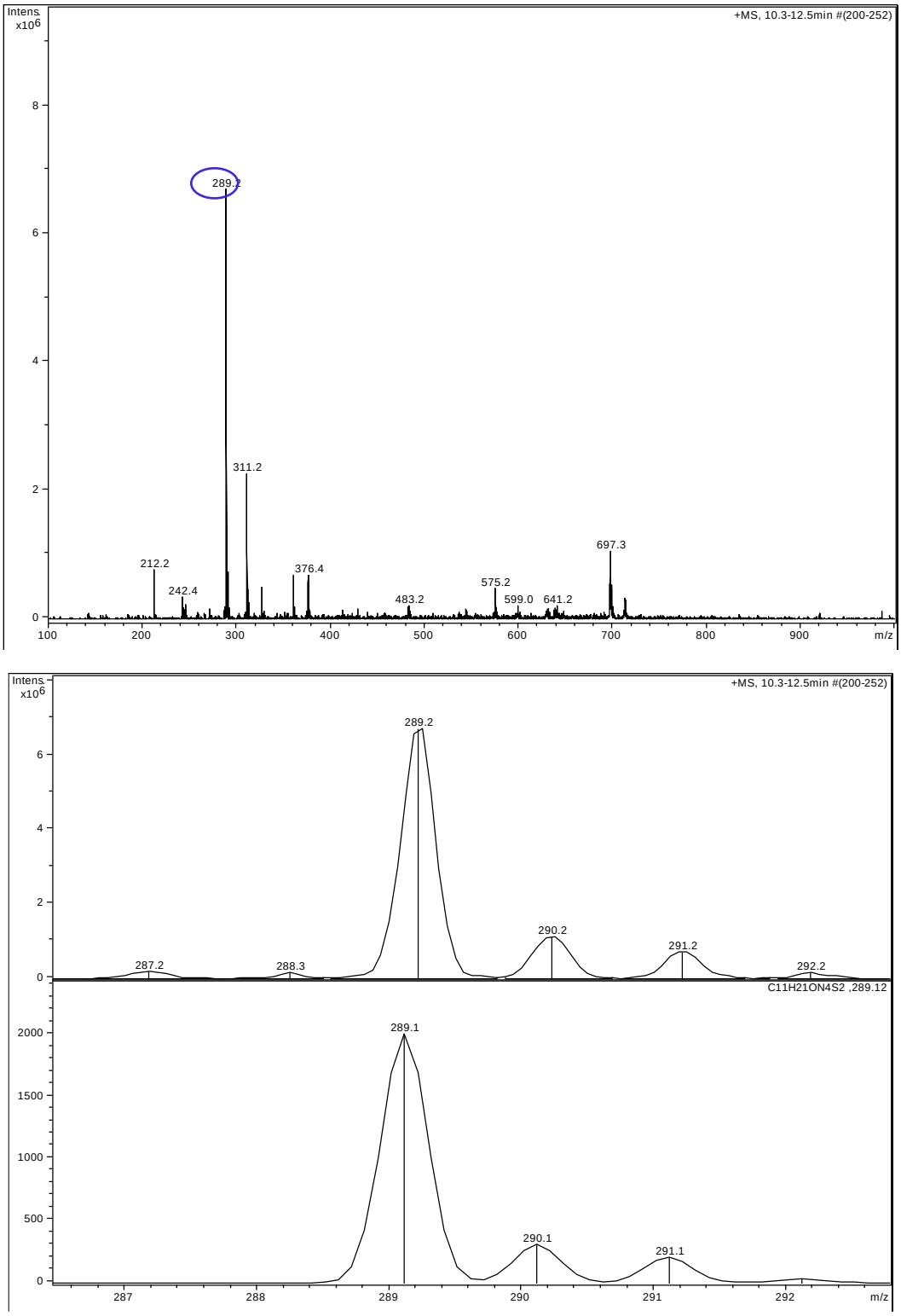

Figure 2.S8: *Top*: LR-ESI-MS(+) of **$H_3N_3S_2^{NMeIm}$•2HCl** in MeOH. *Bottom*: experimental (top) versus theoretical (bottom) isotopic distribution of $[H_3N_3S_2{}^{NMeIm}+H]^+$.

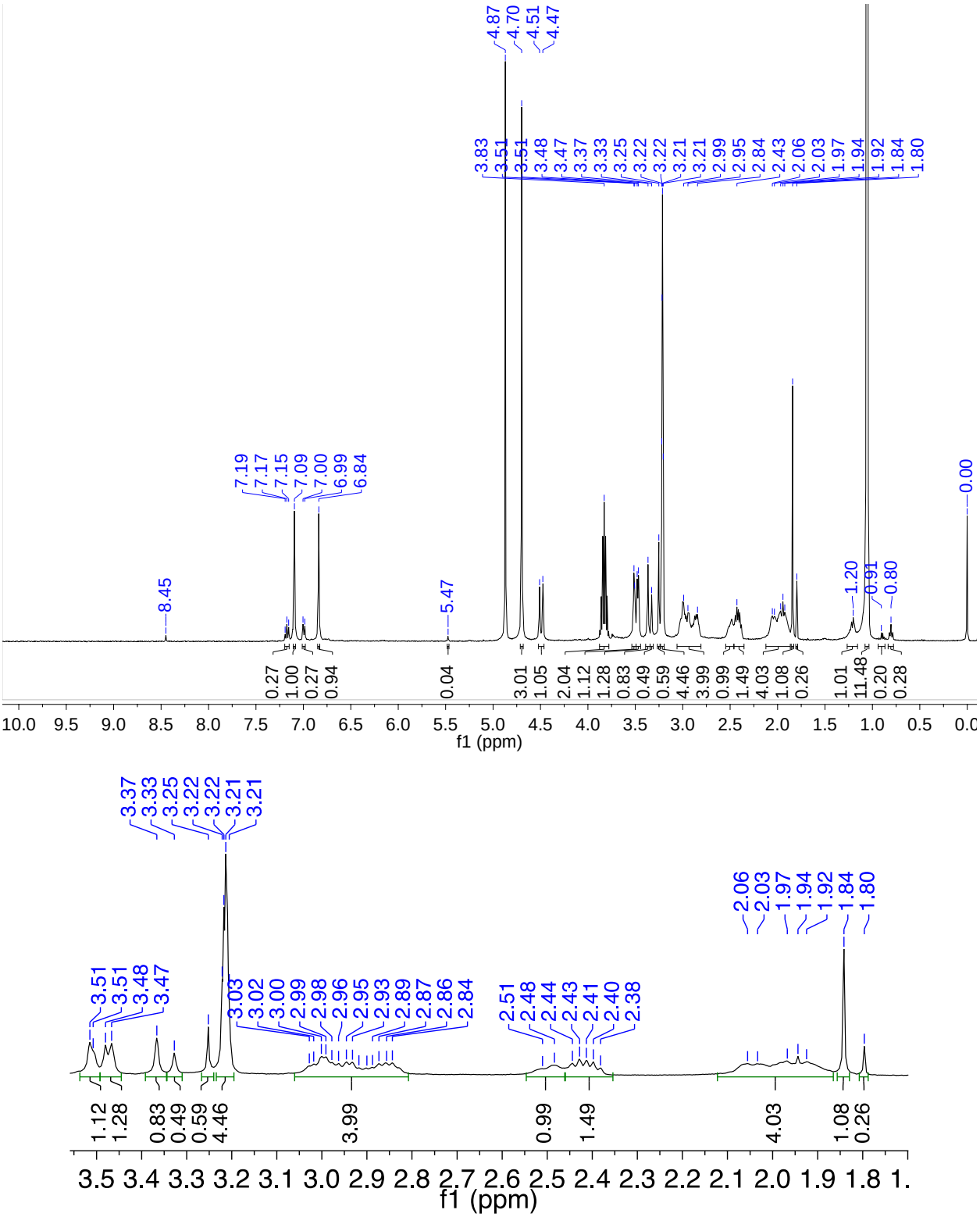

Figure 2.S9: ^{1}H NMR of **4Na** in CD_3OD (400 MHz, δ from protio solvent). Minor amounts of Et_2O (1.20, 3.49 ppm), pentane (0.90, 1.29 ppm), CH_2Cl_2 (5.47 ppm) from work-up, residual protio solvent (3.22, 4.87 ppm), and a sizable amount of *i*PrOH (1.05, 3.84 ppm) from NMR tube cleaning solution. *Top*- full spectrum. *Bottom*- expansion of aliphatic regions.

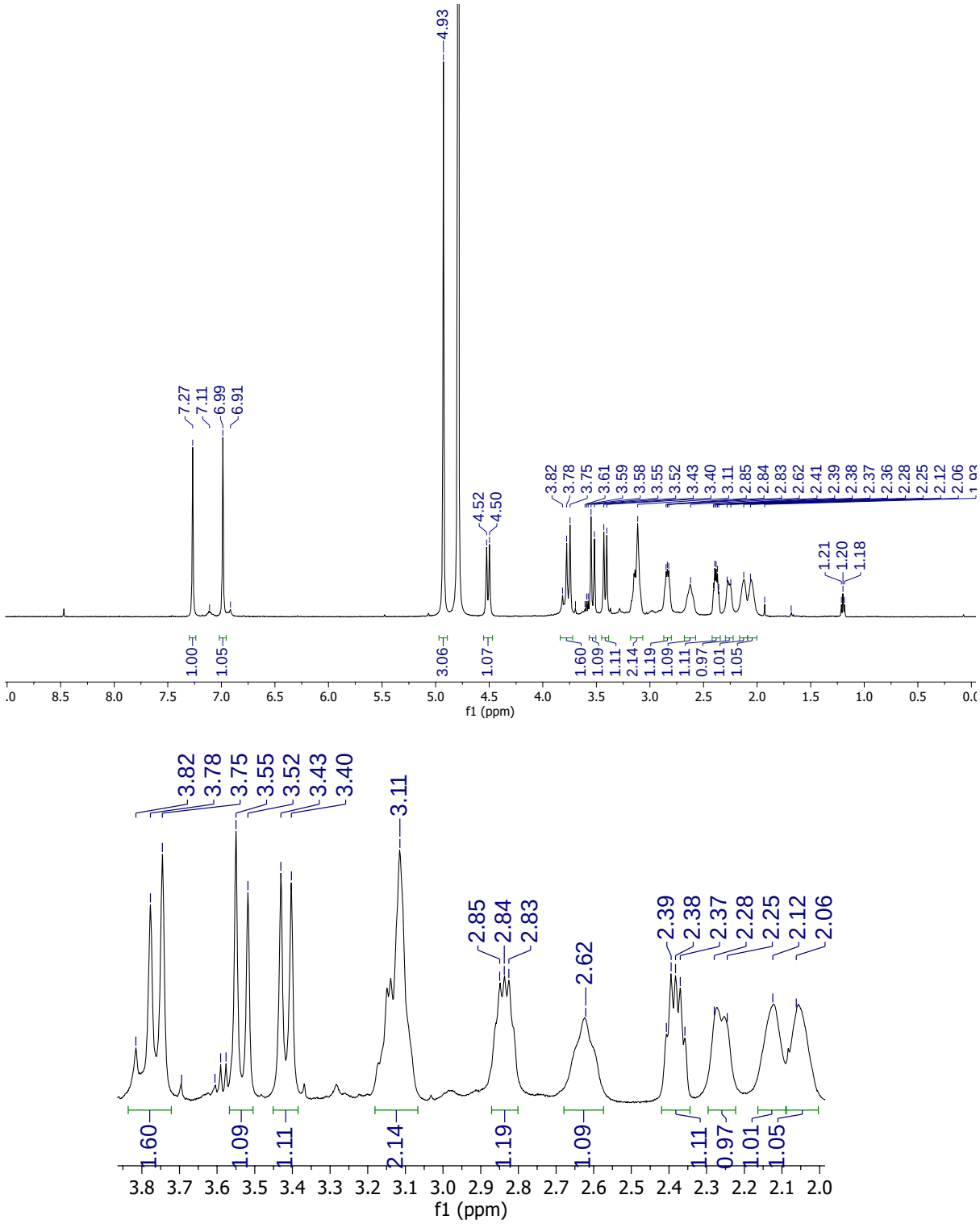

Figure 2.S10: ^{1}H NMR of **4Na** in D_2O (500 MHz, D_2O, δ from protio solvent). Minor amounts of Et_2O (1.20, 3.56 ppm) from work-up and residual protio solvent (4.79 ppm). *Top*- full spectrum. *Bottom*- expansion of aliphatic regions.

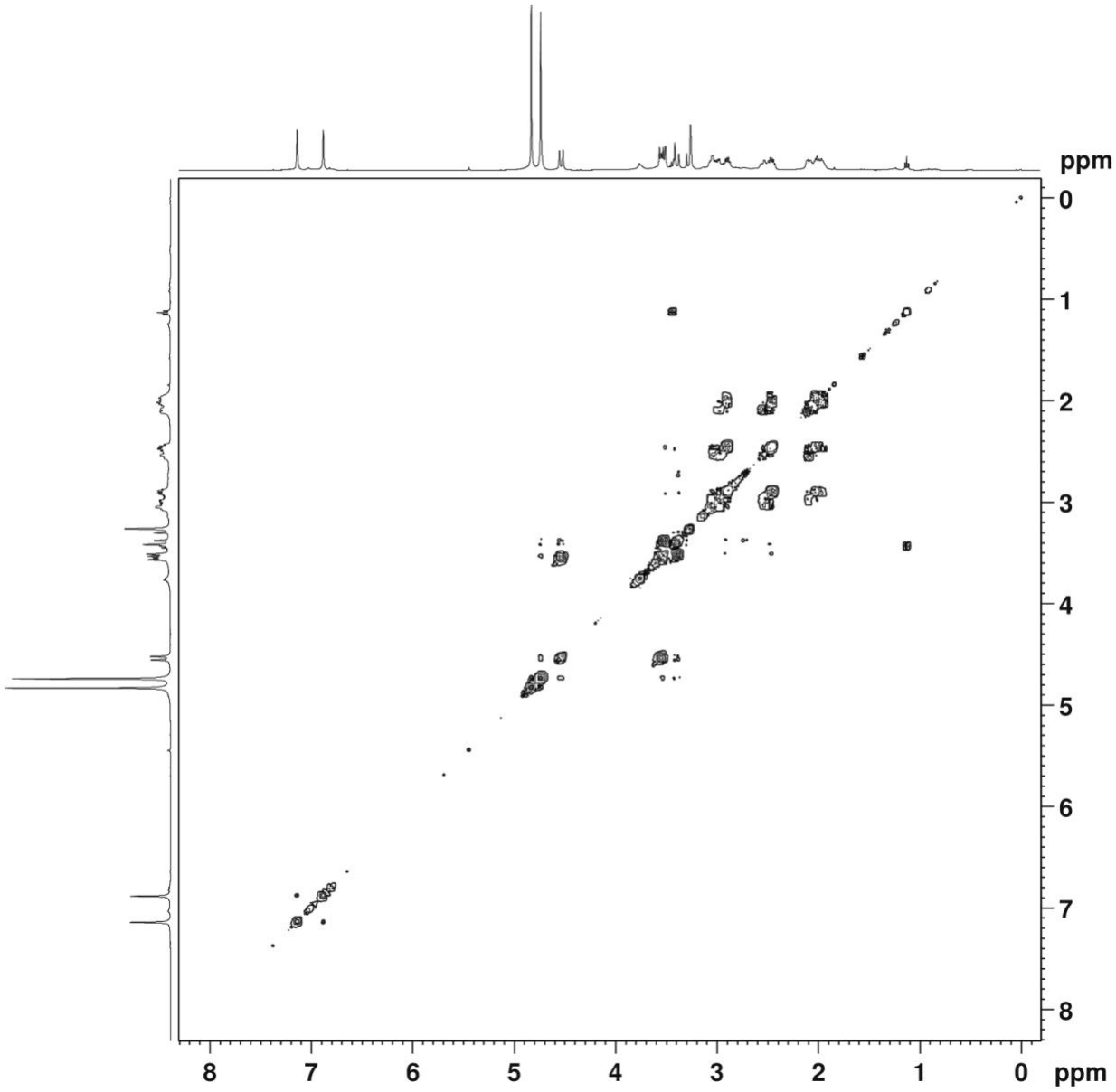

Figure 2.S11: COSY NMR of $\mathbf{4^{Na}}$ (400 MHz, CD_3OD, δ from protio solvent).

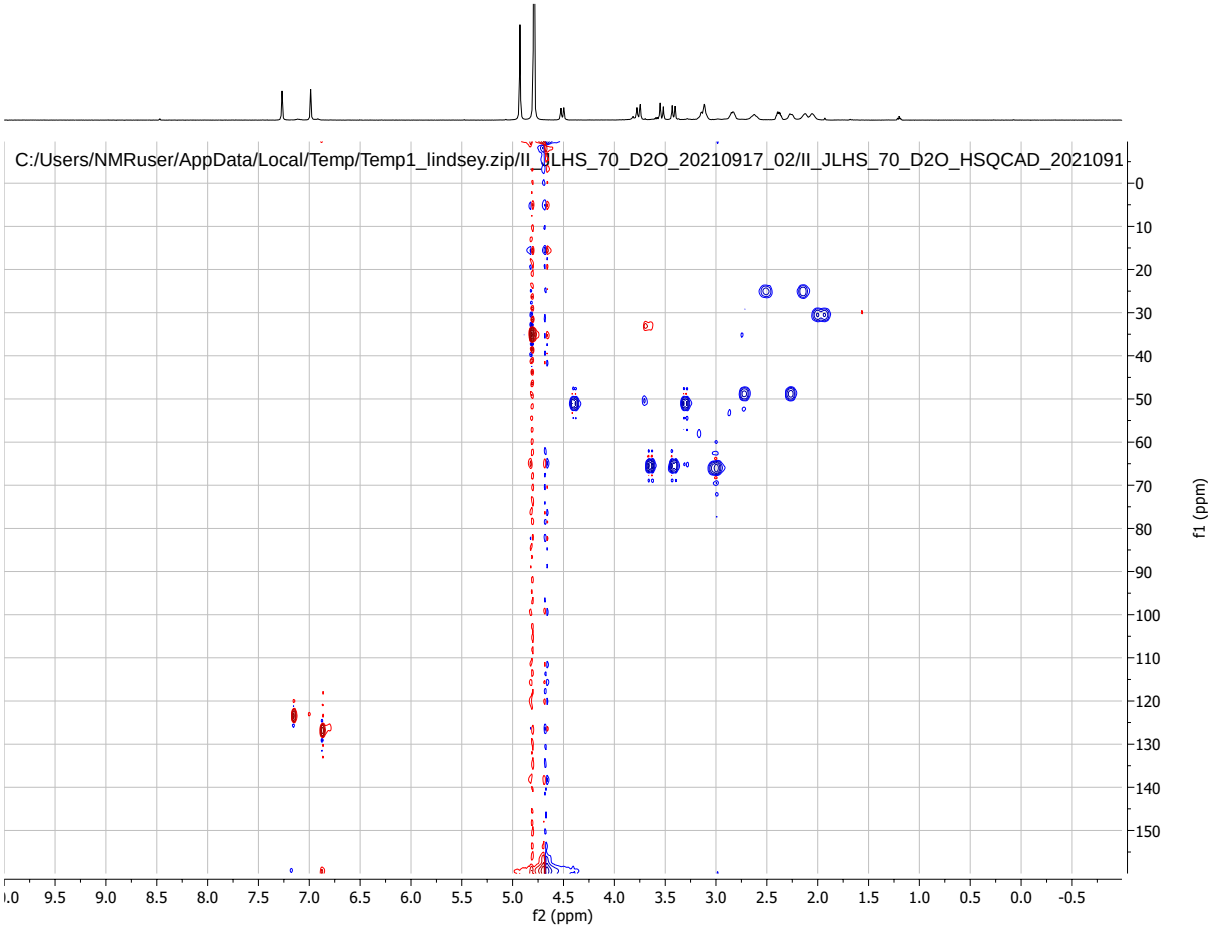

Figure 2.S12: HSQC NMR of $\mathbf{4^{Na}}$ in D_2O (500 MHz, ^1H δ from protio solvent).

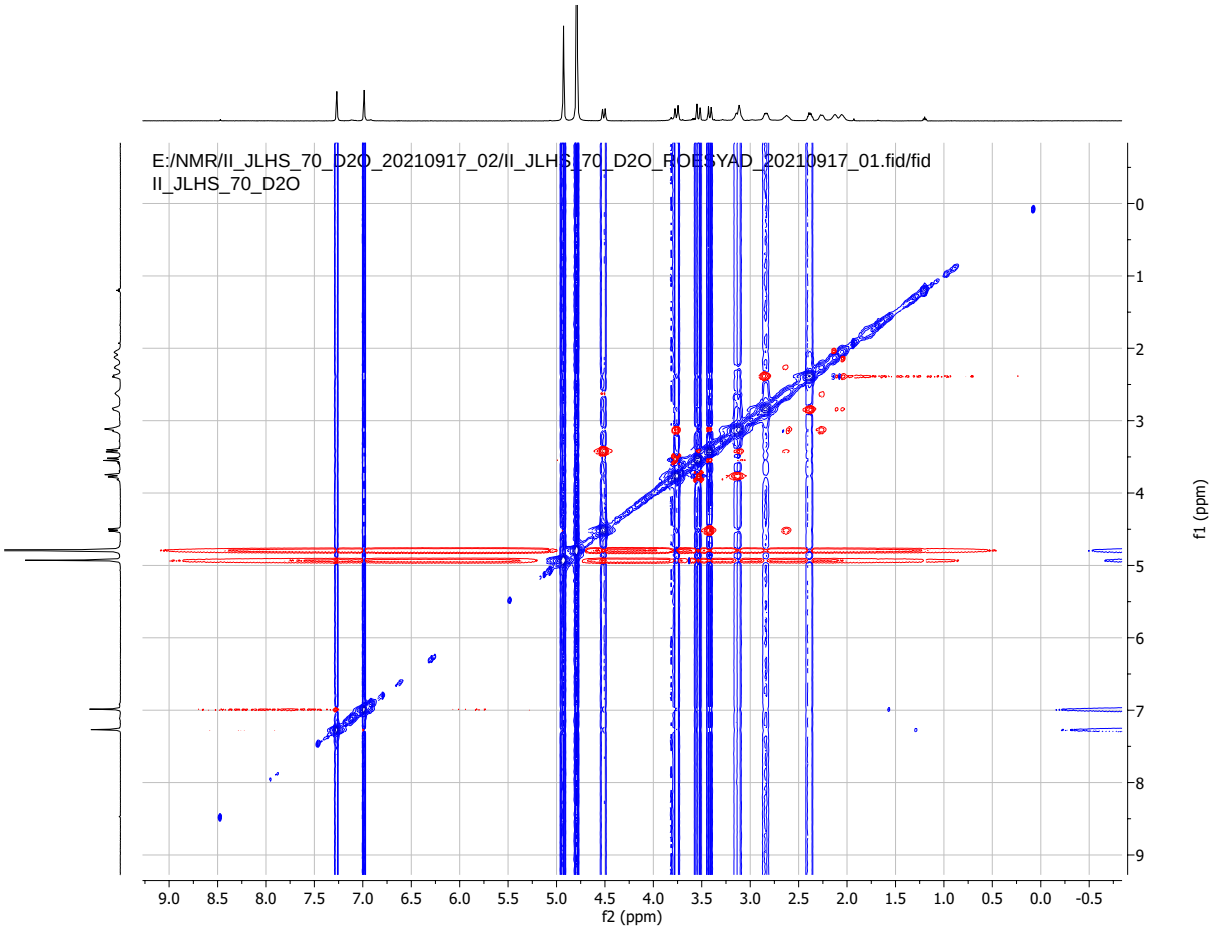

Figure 2.S13: ROESY NMR of **4**^{Na} in D_2O (500 MHz, δ from protio solvent). Blue signals indicate primary and tertiary C; Red signals indicate secondary C.

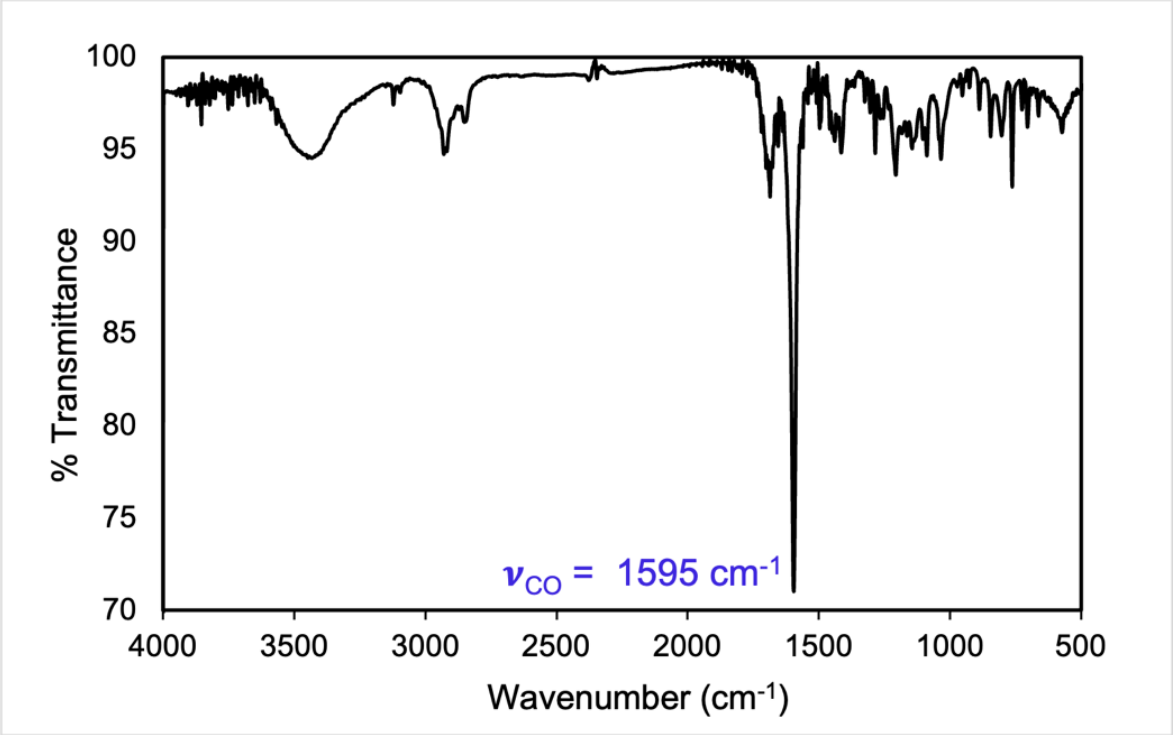

Figure 2.S14: Solid-state FTIR spectrum of **Na[Ni($N_3S_2^{NMeIm}$)]** (**4^{Na}**) in a KBr matrix at RT.

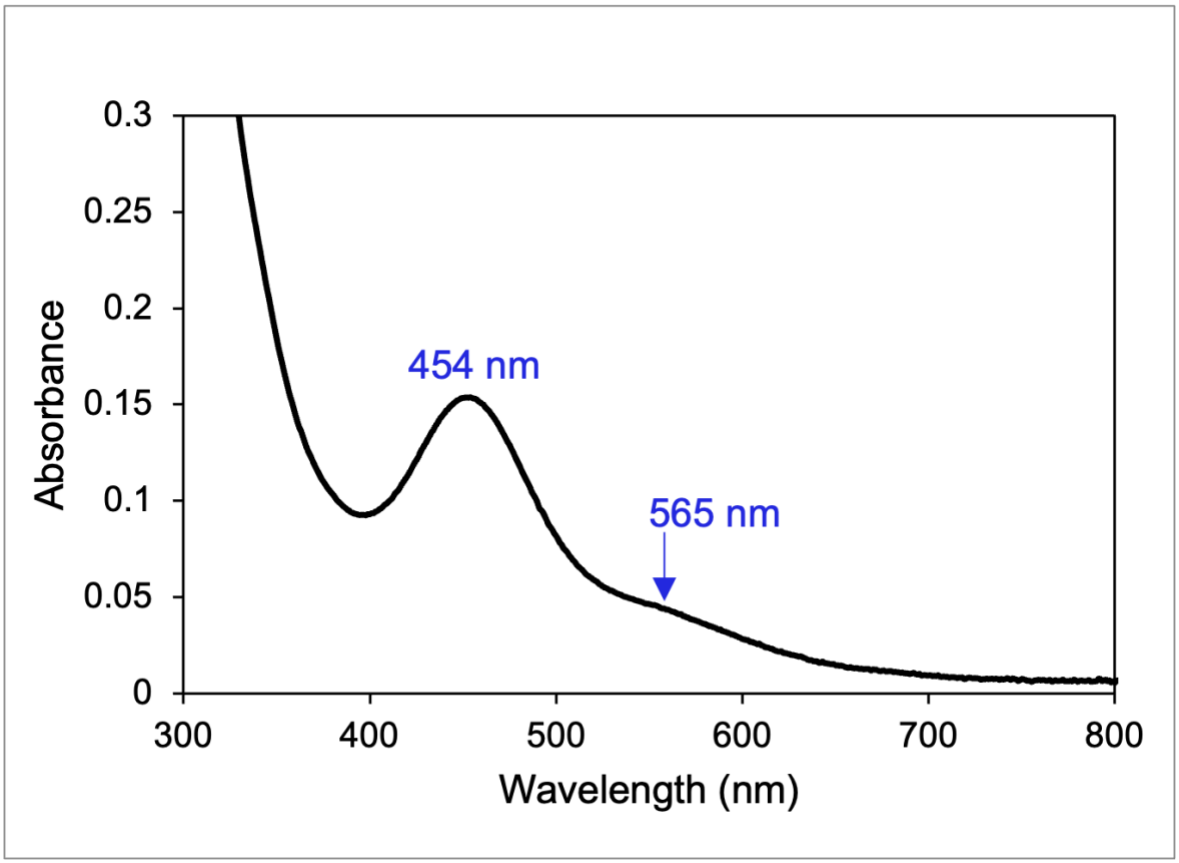

Figure 2.S15: UV-vis spectrum of **Na[Ni($N_3S_2^{NMeIm}$)]** (**4^{Na}**) in MeOH at RT.

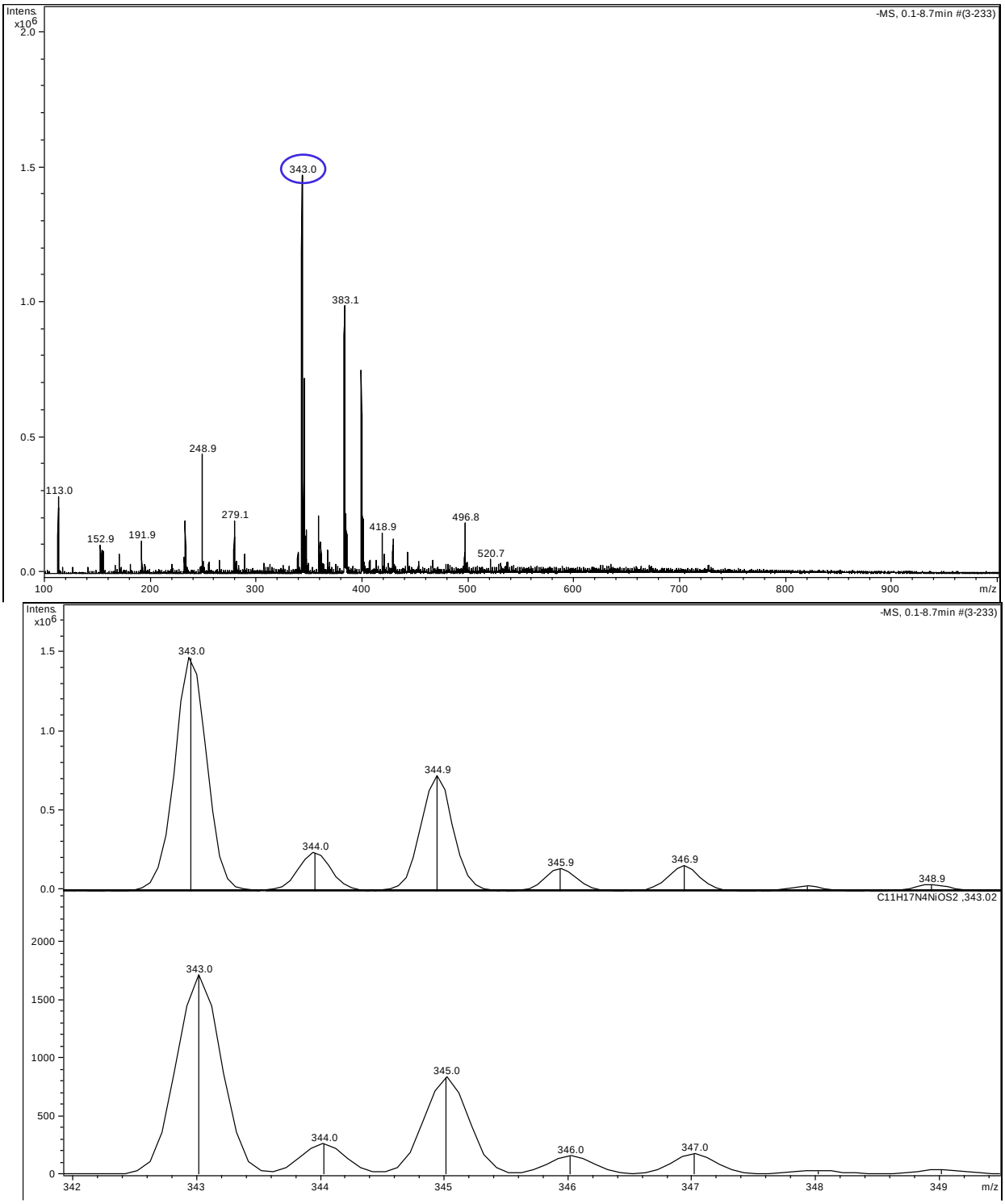

Figure 2.S16: *Top*: LR-ESI-MS(–) of **Na[Ni($N_3S_2^{NMeIm}$)]** (**4^{Na}**) in MeOH. *Bottom*: experimental (top) versus theoretical (bottom) isotopic distribution of $[M–Na]^-$.

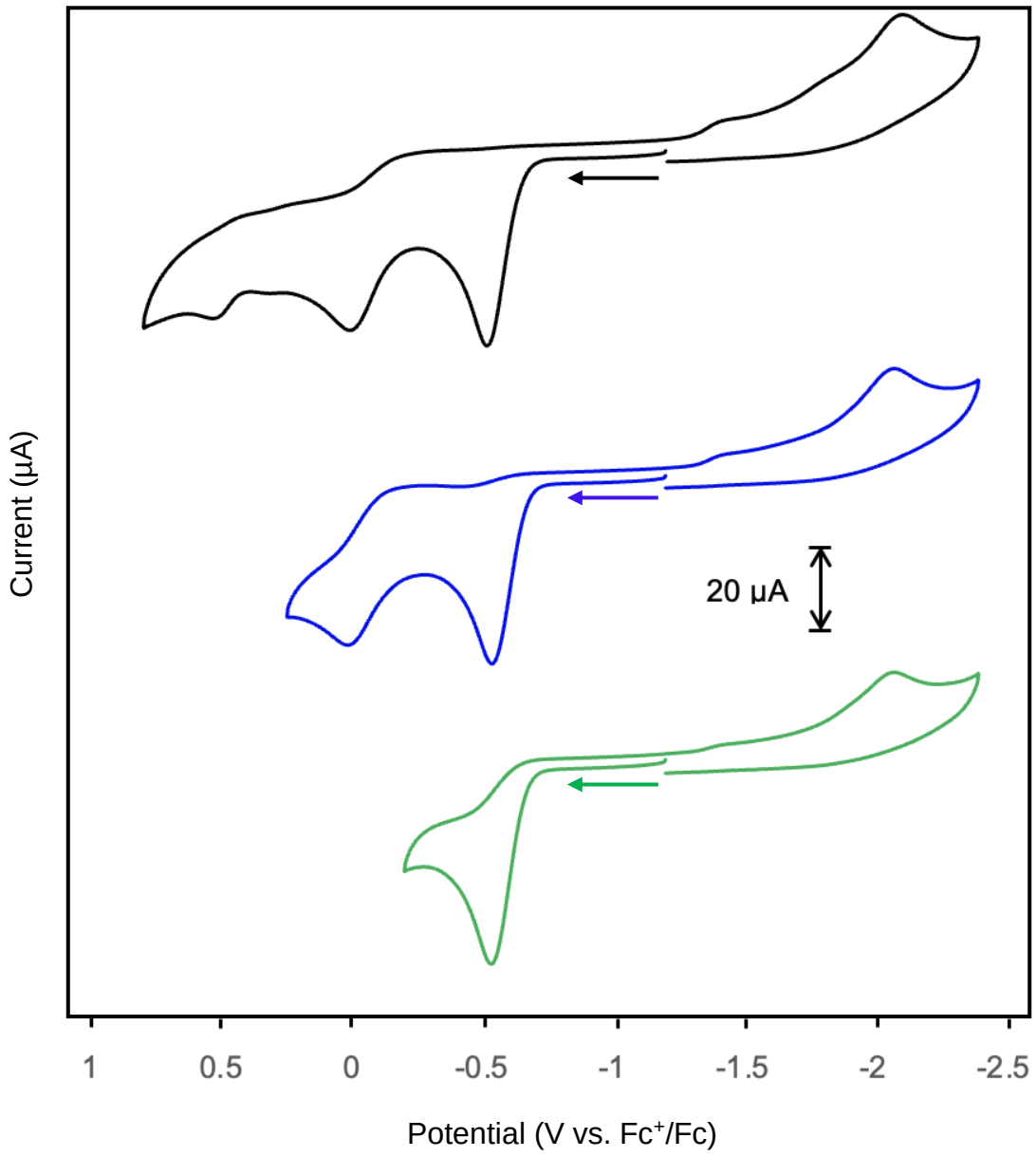

Figure 2.S17. CV of $\mathbf{4^{Na}}$ in DMF (3.14 mM) at RT (0.25 M $^{n}Bu_4NPF_6$ supporting electrolyte, glassy carbon working electrode, 100 mV/s scan rate). Arrow indicates direction of scan.

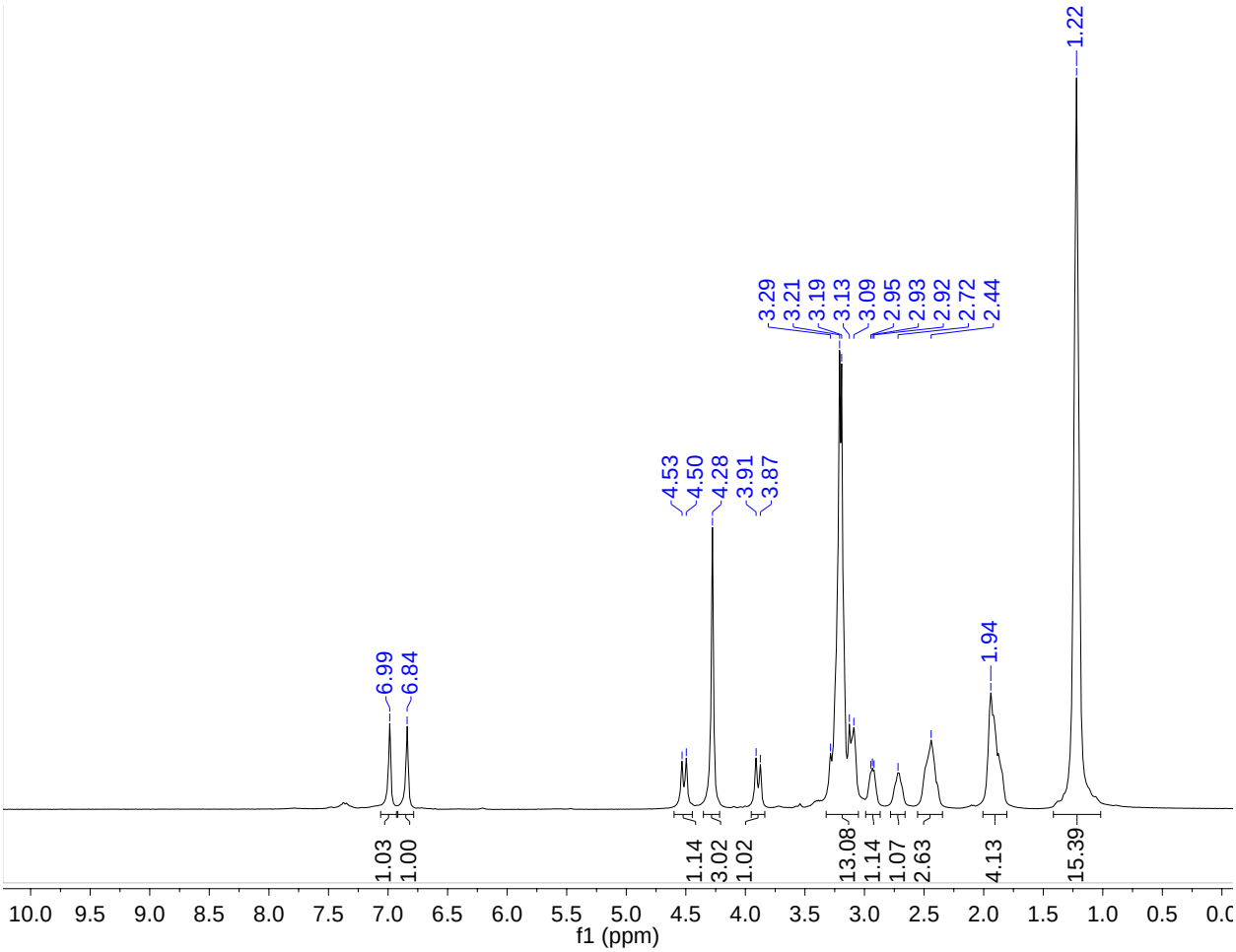

Figure 2.S18: ^{1}H NMR of $\mathbf{4^{Et4N}}$ (400 MHz, CD_3CN, δ from protio solvent). Excess Et_4NCl (3.19, 1.22 ppm), grease (0.07 ppm), hexane (0.88 ppm), and EtOAc (1.26, 4.12 ppm) from work-up. HDO from solvent (1.76 ppm).

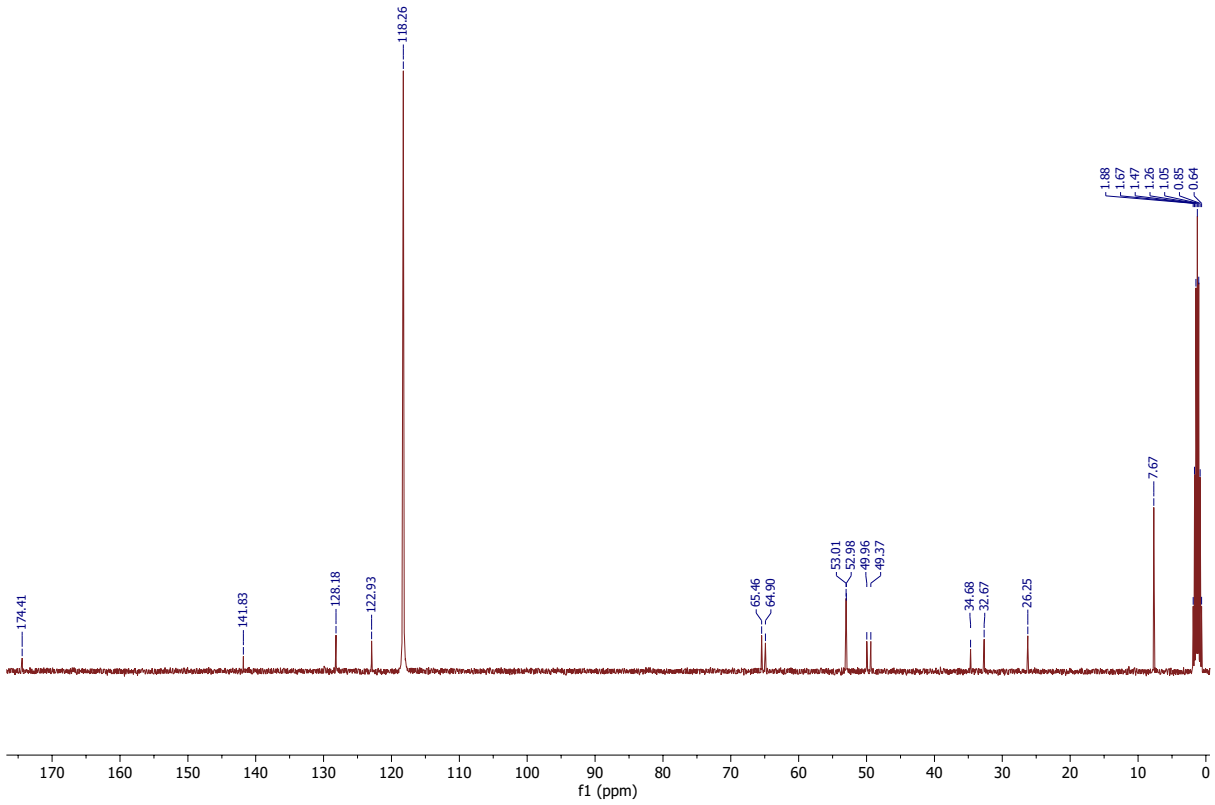

Figure 2.S19: ^{13}C NMR of $\mathbf{4^{Et4N}}$ (101 MHz, CD_3CN). Solvent peak is referenced to 118.26 ppm.

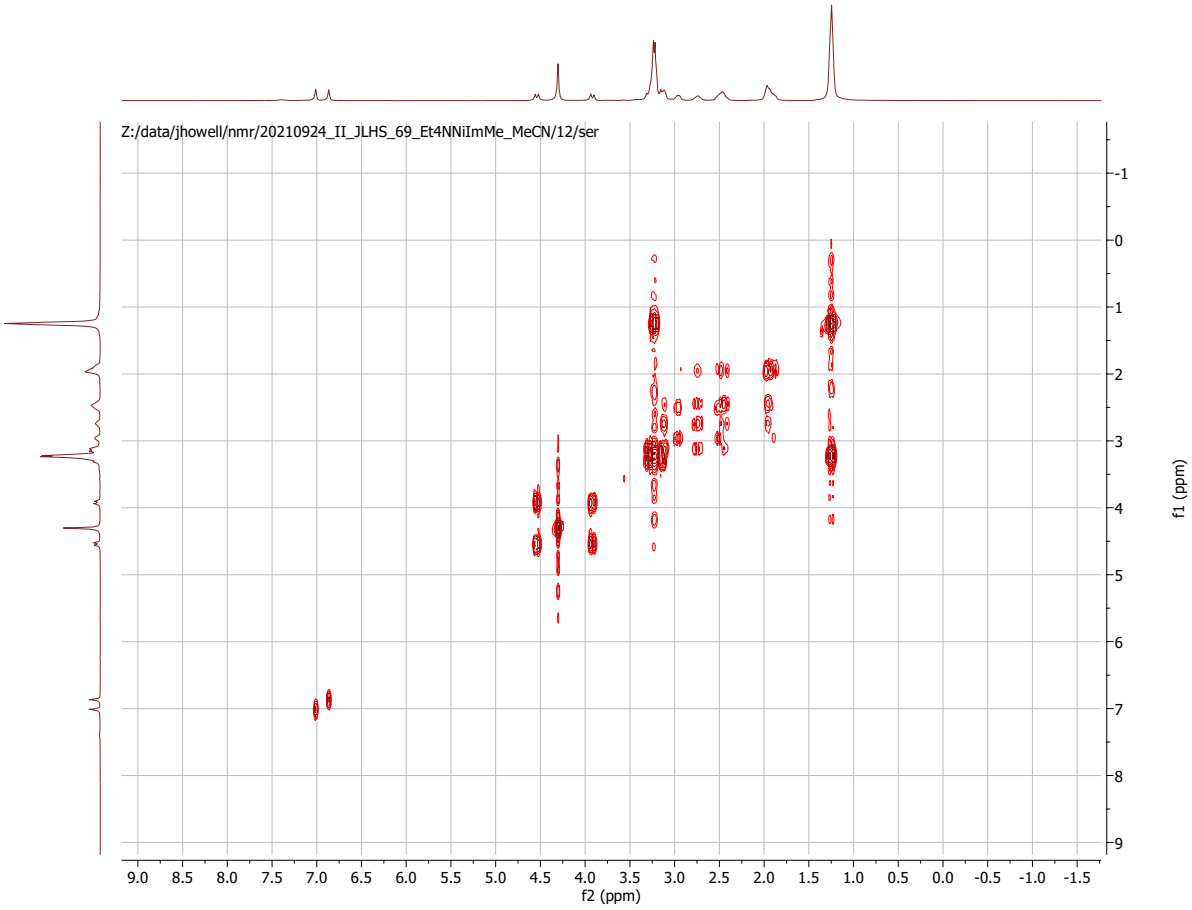

Figure 2.S20: COSY NMR of $\mathbf{4^{Et4N}}$ (400 MHz, CD_3CN, δ from protio solvent).

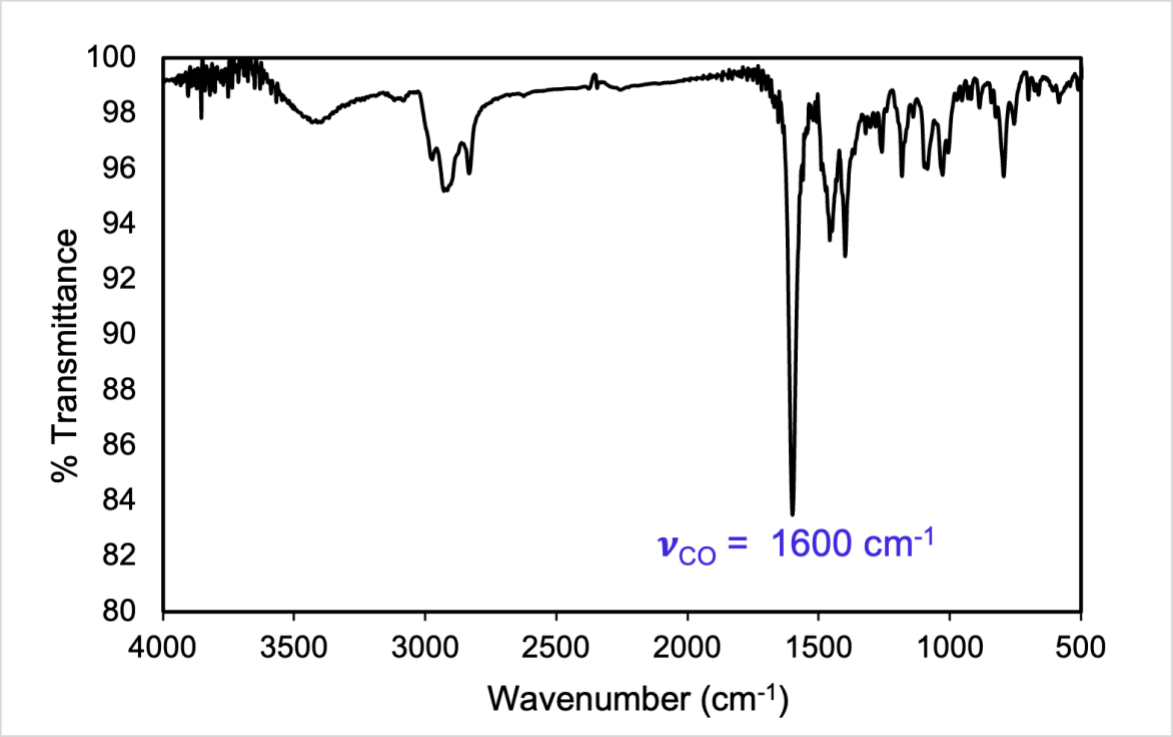

Figure 2.S21: Solid-state FTIR spectrum of **$Et_4N[Ni(N_3S_2^{NMeIm})]$** (**$4^{Et4N}$**) in a KBr matrix at RT.

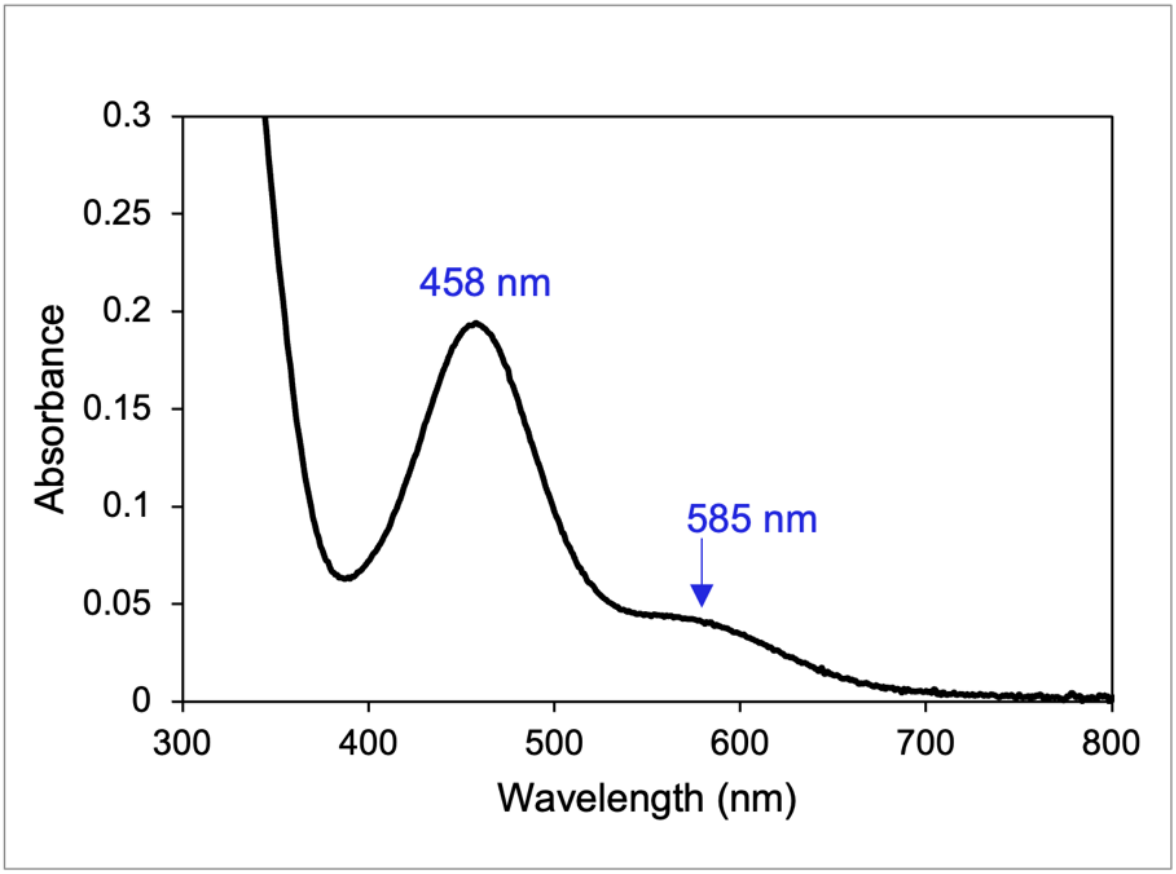

Figure 2.S22: UV-vis spectrum of **$Et_4N[Ni(N_3S_2^{NMeIm})]$** (**$4^{Et4N}$**) in MeCN at RT.

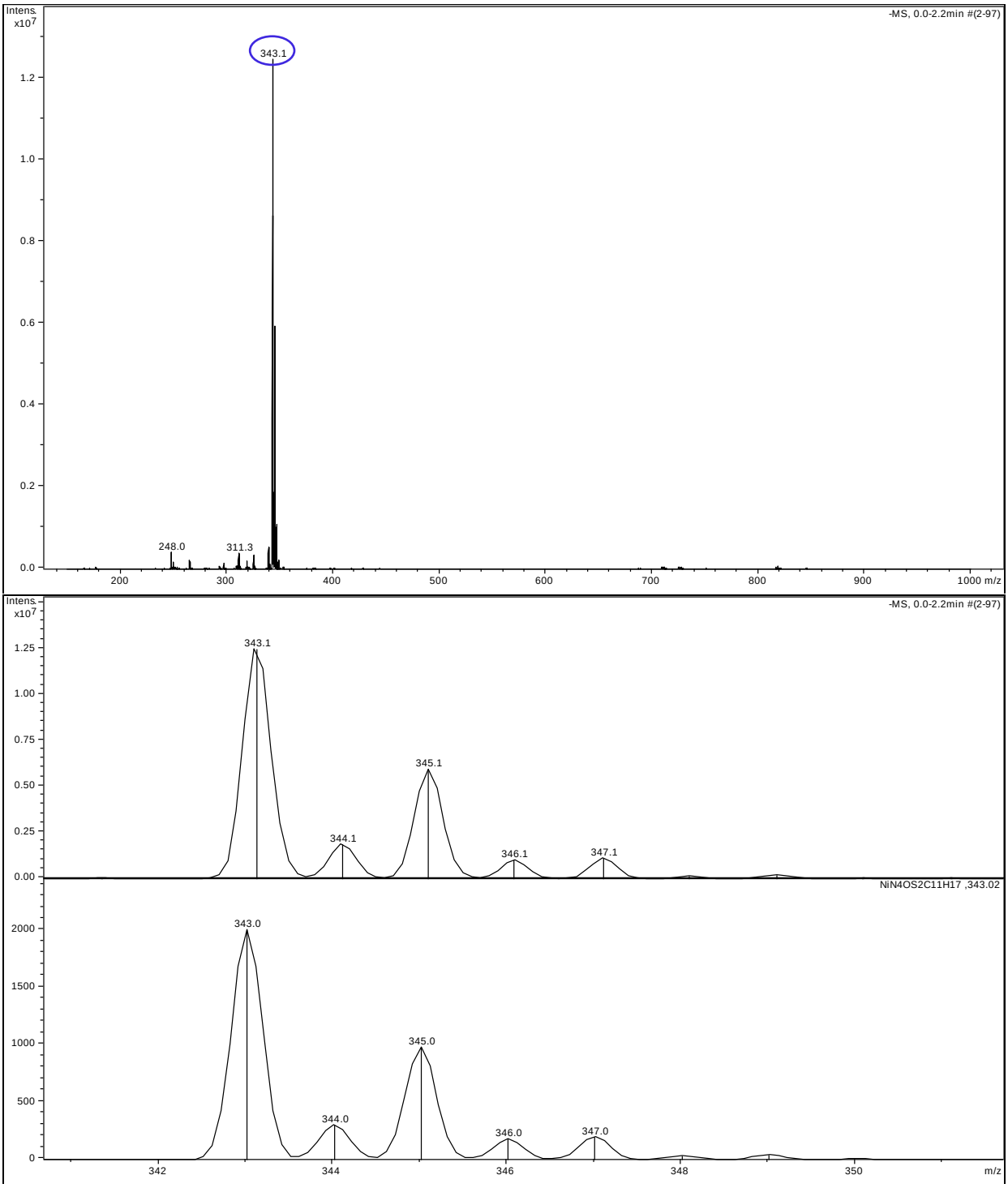

Figure 2.S23: *Top*: LR-ESI-MS(–) of **$Et_4N[Ni(N_3S_2^{NMeIm})]$** (**$4^{Et4N}$**) in MeCN. *Bottom*: experimental (top) versus theoretical (bottom) isotopic distribution of $[M–Et_4N]^-$.

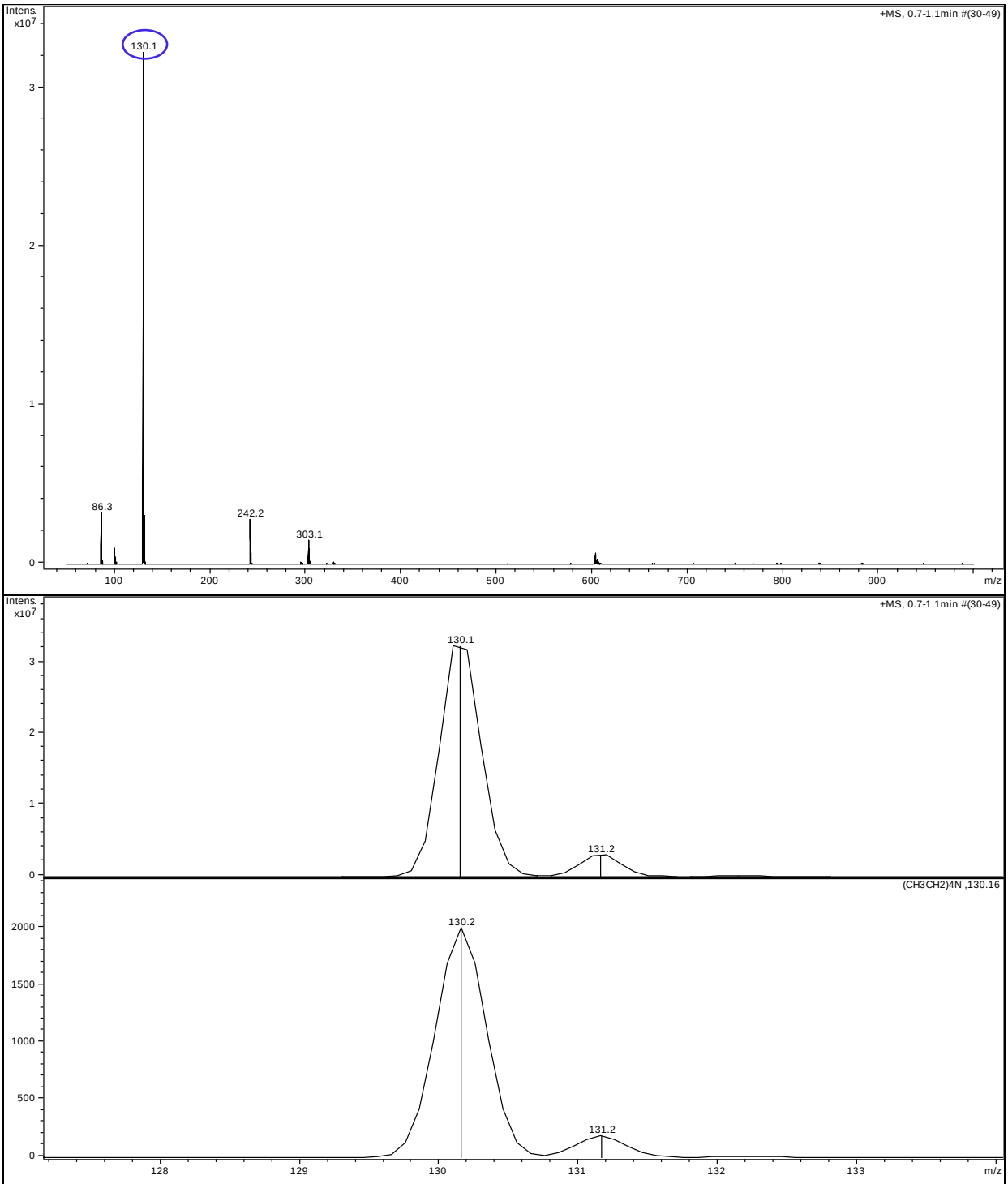

Figure 2.S24: *Top*: LR-ESI-MS(+) of **$Et_4N[Ni(N_3S_2^{NMeIm})]$** (**$4^{Et4N}$**) in MeCN. *Bottom*: experimental (top) versus theoretical (bottom) isotopic distribution of $[Et_4N]^+$.

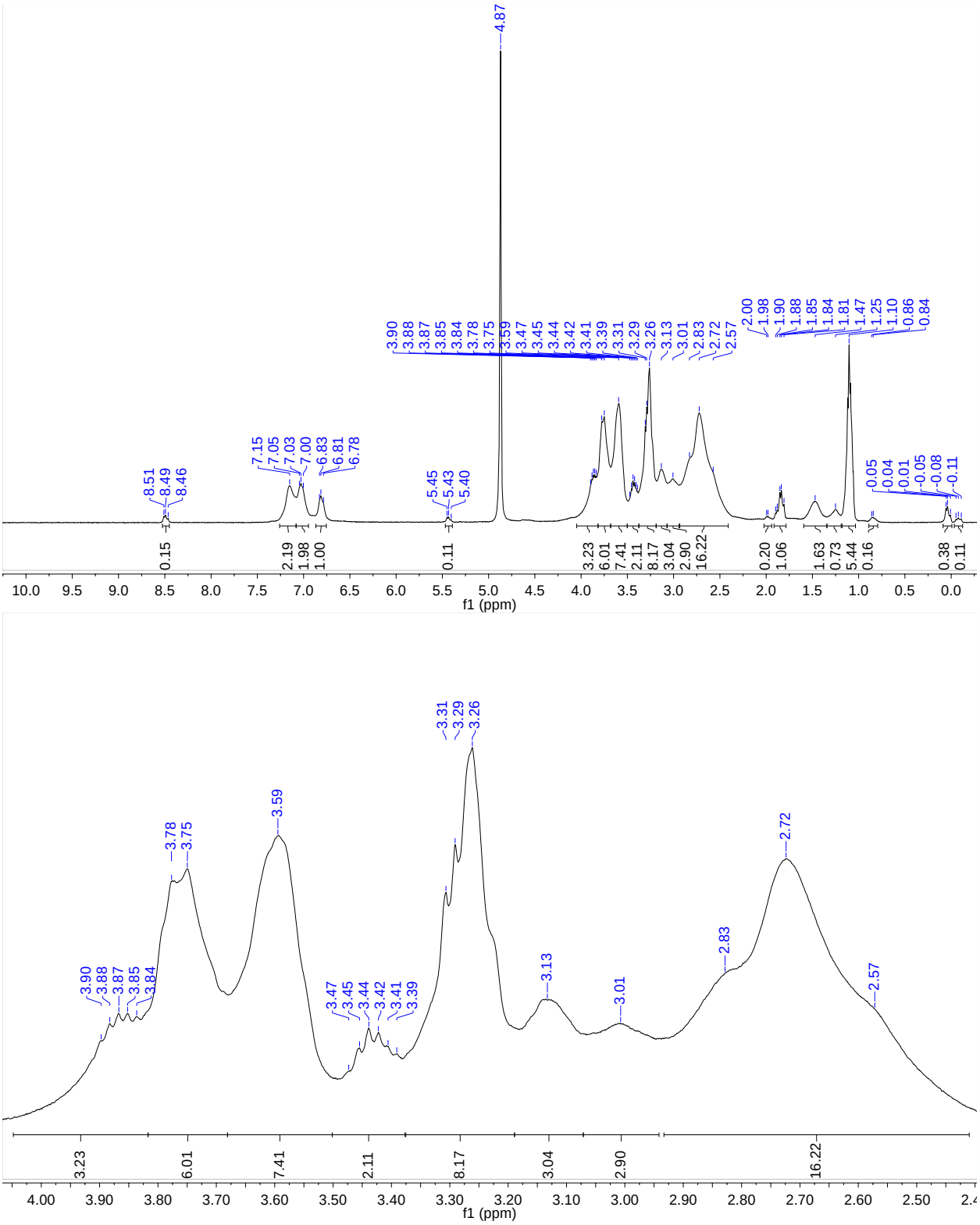

Figure 2.S25: ^{1}H NMR of **Na[Zn($N_3S_2^{NMeIm}$)]** (**5**) (400 MHz, CD_3OD, δ from protio solvent). *Top*- full spectrum. *Bottom*- expansion of 2.4-4.0 ppm. *i*PrOH (3.88, 1.47 ppm), Et_2O (3.49, 1.10 ppm), MeOH (3.29 ppm), and pentane (1.25, 0.85 ppm) from work-up.

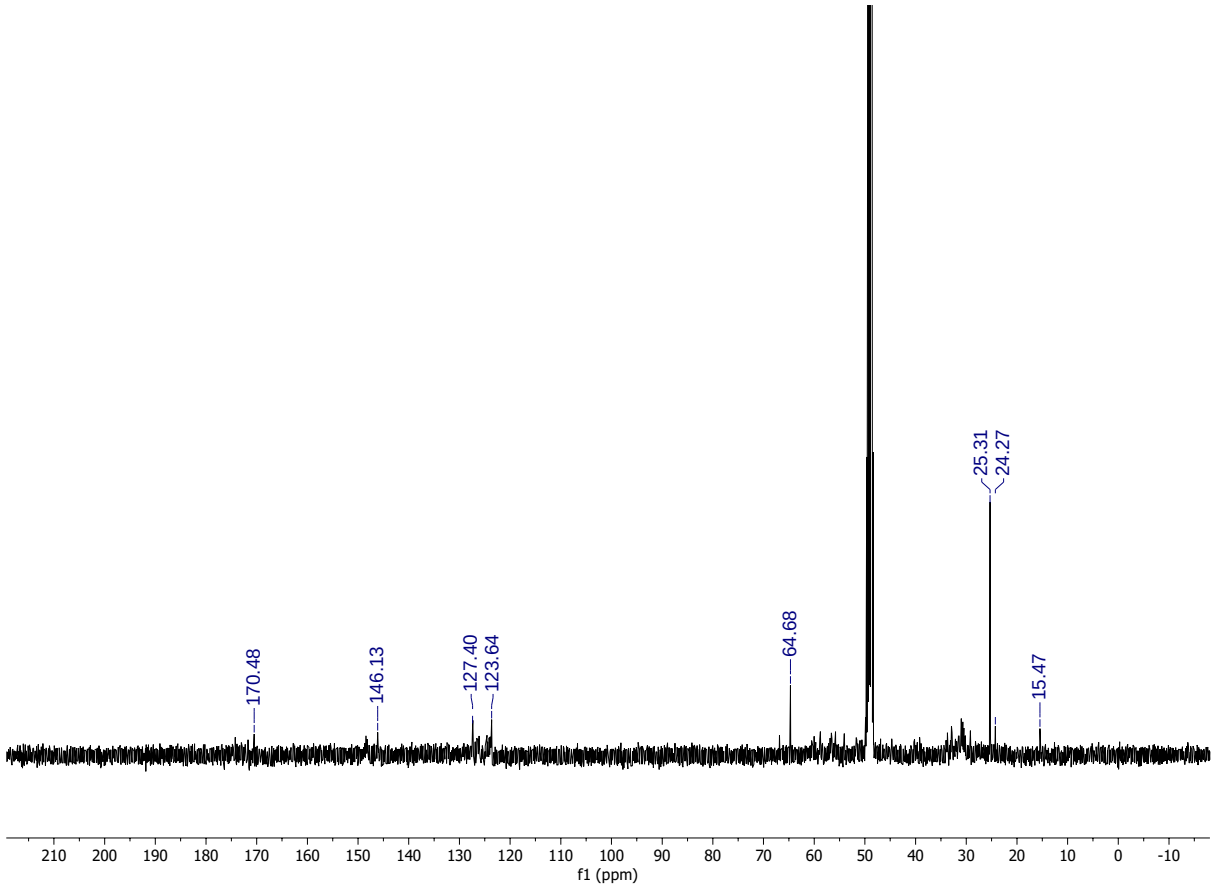

Figure 2.S26: ^{13}C NMR of **Na[Zn($N_3S_2^{NMeIm}$)]** (**5**) (101 MHz, CD_3OD). Solvent peak is referenced to 49.00 ppm. Minor amounts of *i*PrOH from work-up (64.68, 25.31 ppm).

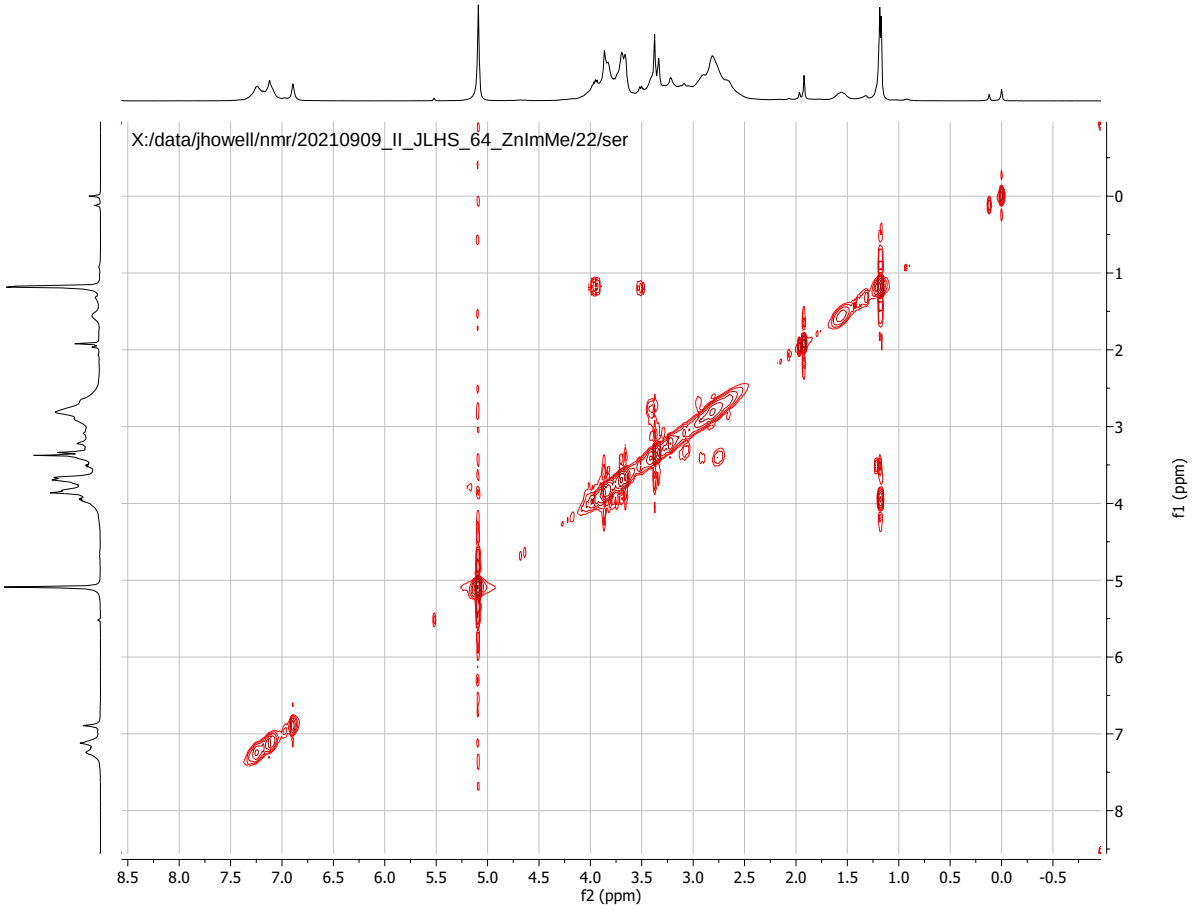

Figure 2.S27: COSY NMR of **Na[Zn($N_3S_2^{NMeIm}$)]** **(5)** (400 MHz, CD_3OD, δ from protio solvent).

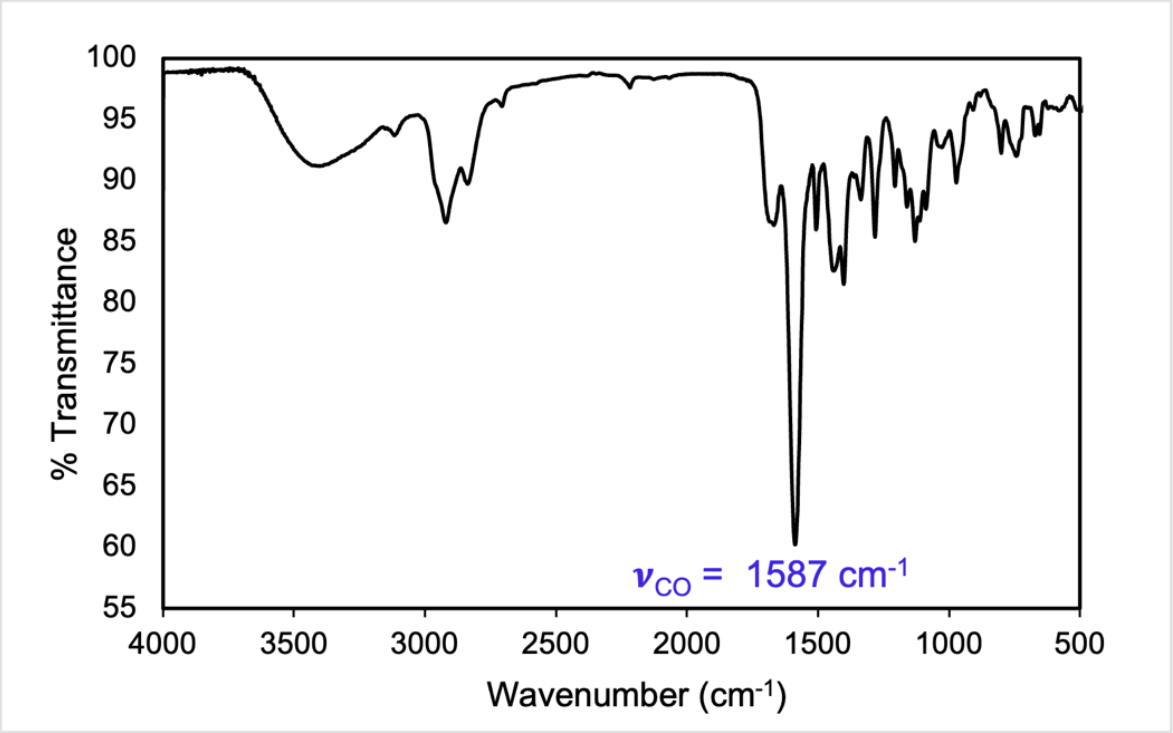

Figure 2.S28: Solid-state FTIR spectrum of **Na[Zn($N_3S_2^{NMeIm}$)]** (**5**) in a KBr matrix at RT.

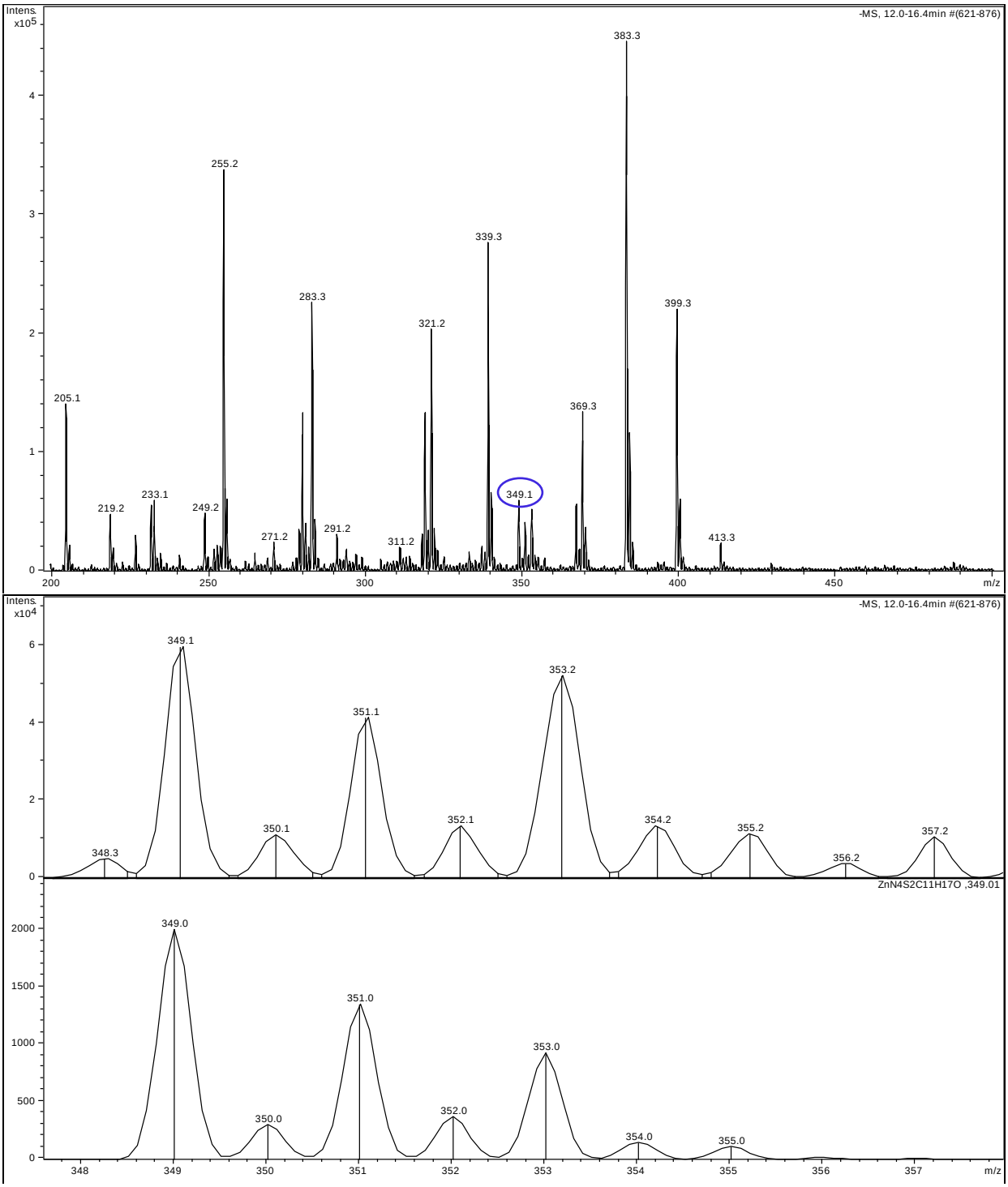

Figure 2.S29: *Top*: LR-ESI-MS(–) of **Na[Zn($N_3S_2^{NMeIm}$)]** (**5**) in MeOH. *Bottom*: experimental (top) versus theoretical (bottom) isotopic distribution of $[M–Na]^-$.

Tables

Table 2.S1: Summary of Crystal Data and Intensity Collection and Structure Refinement Parameters for Na[Ni($N_3S_2^{NMeIm}$)]•2MeOH (**4Na**).

Parameters	**4Na**
Formula	$C_{13}H_{25}O_3N_4NaNi$
Formula weight	431.19
Crystal system	Triclinic
Space group	*P*1
Crystal color, habit	block, orange
a, Å	8.9417 (7)
b, Å	10.4410 (9)
c, Å	11.9883 (9)
α, deg	66.910 (2)
β, deg	75.591 (2)
γ, deg	75.571 (2)
V, Å^3	982.64 (14)
Z	2
ρ_{calcd}, g/cm^3	1.457
T, K	170
abs coeff, μ (Mo Kα), mm^{-1}	1.24
θ limits, deg	2.8-25.3
total no. of data	11041
no. of unique data	3569
no. of parameters	231
no. of restraints	3
H-atom treatment	H atoms treated by a mixture of independent and constrained refinement
GOF of F^2	1.05
R_1, [a] %	0.023
wR_2, [b] %	0.060
max, min peaks, e/Å^3	0.41, −0.28

[a]$R_1 = \Sigma| |F_o| - |F_c| | / \Sigma |F_o|$; [b]$wR_2 = (\Sigma[w(F_o^2 - F_c^2)^2]/\Sigma[w(F_o^2)^2])^{1/2}$

2.6.2 Reactivity Studies

Figures

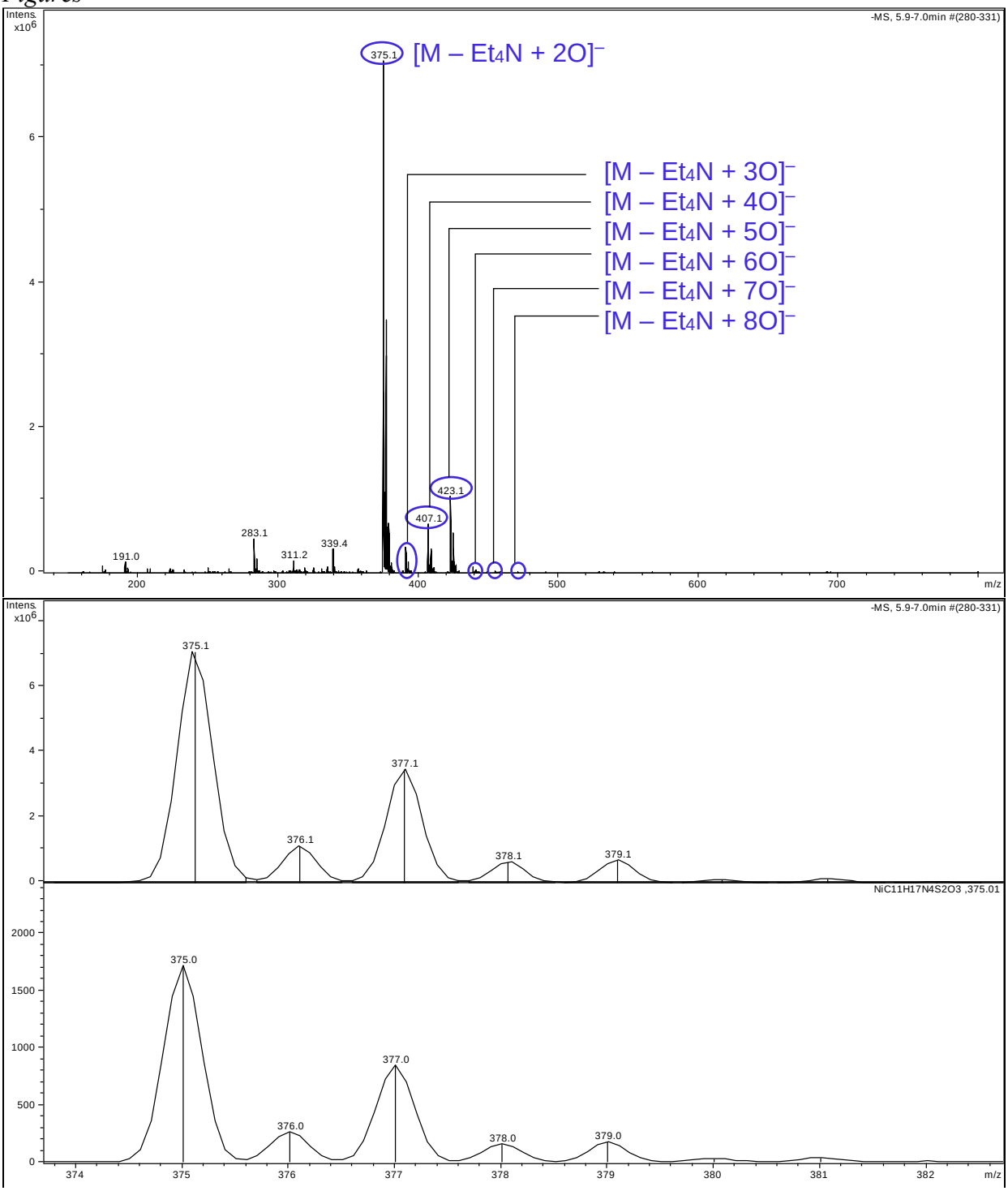

Figure 2.S30: *Top*: LR-ESI-MS(–) of **$Et_4N[Ni(N_3S_2)]$** (**4^{Et4N}**) in MeCN after exposed to air for 5 d. *Bottom*: experimental (top) versus theoretical (bottom) isotopic distribution of $[M–Et_4N + 2O]^–$.

2.6.3 Computations

Figures

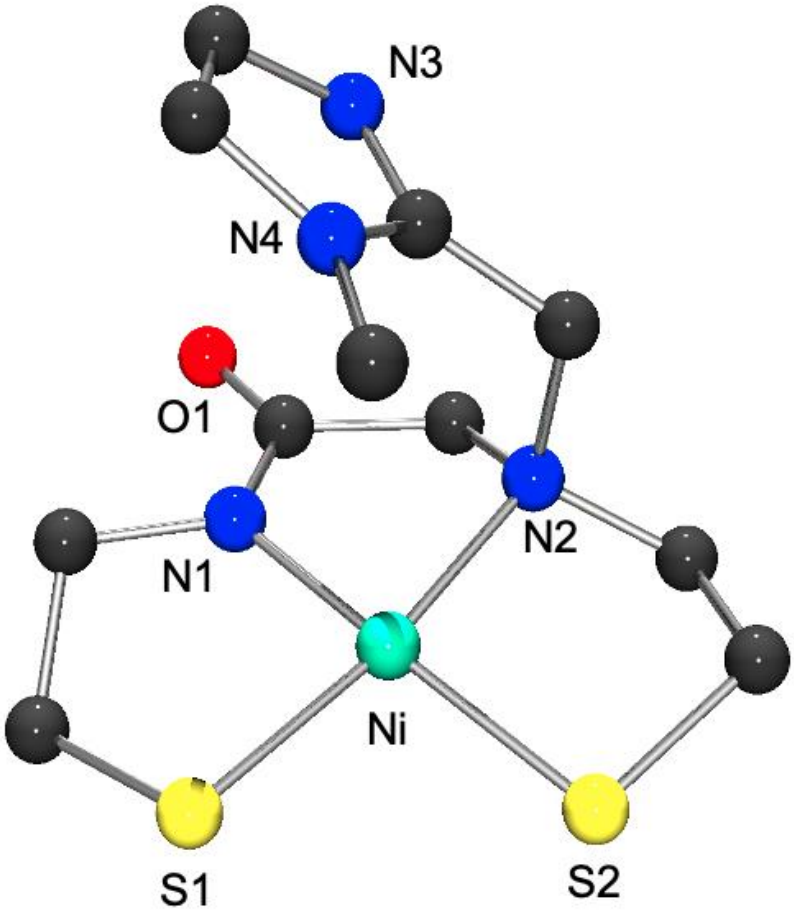

Figure 2.S31: Geometry-optimized structure of **4***. C = gray; Ni = aquamarine; S = yellow; N = blue; O = red.

Tables

Table 2.S2: Optimized M06-L/def2-SVP Cartesian coordinates (Å) for **4**[*]

C	-0.49738142032962	0.62704962009600	-1.59647015770359
C	0.93301577363986	0.08951748095221	-1.62893203905130
C	-2.70856676575203	0.09946451672592	-0.77941583035806
C	2.02415164740768	-1.99331710436041	-0.86971319246611
C	-3.40581479888359	-1.22810865196392	-0.57938461761264
C	2.13797922745029	-2.98337691053372	0.26761426435488
C	1.88655038571710	-0.10525912848081	0.62876149450541
C	1.22902305701711	3.39086326517472	0.97187917188131
C	1.39021054292248	1.26016343334620	0.91672517544578
C	0.18033867535978	2.90612096848416	1.71438602563551
C	-0.59621865271507	0.60867621211525	2.33536945610282
H	1.05587061955610	-0.48114481169547	-2.56198990529847
H	1.65877774981118	0.91789687891387	-1.65981451745683
H	-3.04651306486627	0.62160475631912	-1.69402638626949
H	1.52561477956928	-2.45984776222955	-1.73244666616341
H	-3.37426945601077	-1.79485874574942	-1.52544062558269
H	3.02509438680893	-1.64188323609870	-1.20822000834812
H	-4.46817263065774	-1.09170478139060	-0.32057156895757
H	-2.94296355670825	0.78131618839246	0.06574913590739
H	2.57297346553550	-3.91440927537325	-0.12921017022304
H	2.95368560617133	0.00749952725169	0.36235431177405
H	1.47814015976463	4.43101734011265	0.77023340435806
H	2.86179378048878	-2.61483740724811	1.01613844517810
H	1.81810557771453	-0.75249003966143	1.51543813540669
H	-0.63029430051691	3.38566850622647	2.25551448905791
H	-1.50209829387965	0.42855228235553	1.74057582944824
H	-0.10901913702363	-0.36705613678603	2.45106794948245
H	-0.87129523268559	0.99563553855214	3.32537906022379
N	-1.28641496727959	-0.15727870837919	-0.85035905972028
N	1.19751992259574	-0.82682855342966	-0.48792252642454
N	1.98227581069038	2.36462135950796	0.48140684587551
N	0.29695859701046	1.54186952876988	1.68357208554868
Ni	-0.55790568600814	-1.62210989184040	0.09617456142188
O	-0.81143071295611	1.62291380101492	-2.26351450757198
S	-2.58056325807782	-2.20949258058713	0.73176118680892
S	0.50887216911968	-3.32815747850336	1.03536075079070

Table 2.S3. Löwdin population analysis derived from the DFT computations for selected MOs of **4*** from M06-L/def2-SVP with no COSMO. Only s and p contributions were tabulated for N and S atoms. Bonding interactions are represented with a + and antibonding interactions are denoted with a –. N1 = carboxamido-N; N2 = amine-N; N3 = NMeIm-1N (without Me group); N4 = NMeIm-3N (with Me group); S1 = $S_{trans\text{-carboxamide}}$; S2 = $S_{trans\text{-amine}}$.

	MO#	**Energy (eV)**	**%Ni1**	**%S1**	**%S2**	**%N1**	**%N2**	**%N3**	**%N4**
LUMO+2	93	2.3971	1.10	0.30	0.00	0.50	18.70	1.20	1.40
LUMO+1	92	1.5968	1.10	0.30	0.10	18.30	8.90	4.20	0.50
LUMO	91	–0.2527	55.30	8.30	13.60	0.20	0.20	5.60	5.60
HOMO	90	–0.3884	61.60	22.00	1.70	0.00	0.00	0.00	4.80
HOMO-1	89	–0.4785	62.60	0.40	27.70	0.00	0.00	0.30	2.40
HOMO-2	88	–1.5884	83.30	1.00	10.80	0.00	0.00	0.40	0.80

2.7 References

1. Sheng, Y.; Abreu, I. A.; Cabelli, D. E.; Maroney, M. J.; Miller, A.-F.; Teixeira, M.; Valentine, J. S., Superoxide Dismutases and Superoxide Reductases. *Chem. Rev.* **2014,** *114*, 3854-3918.

2. Valentine, J. S.; Wertz, D. L.; Lyons, T. J.; Liou, L.-L.; Goto, J. J.; Gralla, E. B., The dark side of dioxygen biochemistry. *Curr. Opin. Chem. Biol.* **1998,** *2*, 253-262.

3. Maritim, A. C.; Sanders, R. A.; Watkins, J. B., Diabetes, oxidative stress, and antioxidants: A review. *J. Biochem. Mol. Toxic.* **2003,** *17*, 24-38.

4. Kocatürk, P. A.; Akbostanci, M. C.; Tan, F.; Kavas, G. Ö., Superoxide dismutase activity and zinc and copper concentrations in Parkinson's disease. *Pathophysiology* **2000,** *7*, 63-67.

5. De Leo, M. E.; Borrello, S.; Passantino, M.; Palazzotti, B.; Mordente, A.; Daniele, A.; Filippini, V.; Galeotti, T.; Masullo, C., Oxidative stress and overexpression of manganese superoxide dismutase in patients with Alzheimer's disease. *Neurosci. Lett.* **1998,** *250*, 173-176.

6. Miller, A.-F., Superoxide dismutases: active sites that save, but a protein that kills. *Curr. Opin. Chem. Biol.* **2004,** *8*, 162-168.

7. Fortunato, G.; Pastinese, A.; Intrieri, M.; Lofrano, M. M.; Bolletti Gaeta, G.; Censi, M. B.; Boccalatte, A.; Salvatore, F.; Sacchetti, L., Serum Mn-superoxide dismutase in acute myocardial infarction. *Clin. Biochem.* **1997,** *30*, 569-571.

8. Koppenol, W. H.; Stanbury, D. M.; Bounds, P. L., Electrode potentials of partially reduced oxygen species, from dioxygen to water. *Free Radical Biol. Med.* **2010,** *49*, 317-322.

9. Pelmenschikov, V.; Siegbahn, P. E. M., Nickel Superoxide Dismutase Reaction Mechanism Studied by Hybrid Density Functional Methods. *J. Am. Chem. Soc.* **2006,** *128*, 7466-7475.

10. Youn, H.-D.; Kim, E.-J.; Roe, J.-H.; Hah, Y. C.; Kang, S.-O., A novel nickel-containing superoxide dismutase from *Streptomyces* spp. *Biochem. J.* **1996,** *318*, 889-896.

11. Uudsemaa, M.; Tamm, T., Density-Functional Theory Calculations of Aqueous Redox Potentials of Fourth-Period Transition Metals. *J. Phys. Chem. A* **2003,** *107*, 9997-10003.

12. Grapperhaus, C. A.; Darensbourg, M. Y., Oxygen Capture by Sulfur in Nickel Thiolates. *Acc. Chem. Res.* **1998,** *31*, 451-459.

13. Truong, P. T.; Howell, J. L.; Chakraborty, I.; Olmstead, M. M.; Harrop, T. C., Synthetic Models of NiSOD with N_3S_2 Coordination: Modulation of Ligand Basicity Leads to Five-Coordinate Ni^{2+} and Reversible Ni-Redox. *submitted to Inorg. Chem.* **2021**, manuscript id: ic-2021-03791z.

14. Barondeau, D. P.; Kassmann, C. J.; Bruns, C. K.; Tainer, J. A.; Getzoff, E. D., Nickel superoxide dismutase structure and mechanism. *Biochemistry* **2004,** *43*, 8038-8047.

15. Broering, E. P.; Truong, P. T.; Gale, E. M.; Harrop, T. C., Synthetic Analogues of Nickel Superoxide Dismutase: A New Role for Nickel in Biology. *Biochemistry* **2013,** *52*, 4-18.

16. Fiedler, A. T.; Bryngelson, P. A.; Maroney, M. J.; Brunold, T. C., Spectroscopic and Computational Studies of Ni Superoxide Dismutase: Electronic Structure Contributions to Enzymatic Function. *J. Am. Chem. Soc.* **2005,** *127*, 5449-5462.

17. Herbst, R. W.; Guce, A.; Bryngelson, P. A.; Higgins, K. A.; Ryan, K. C.; Cabelli, D. E.; Garman, S. C.; Maroney, M. J., Role of conserved tyrosine residues in NiSOD catalysis: a case of convergent evolution. *Biochemistry* **2009,** *48*, 3354-3369.

18. Johnson, O. E.; Ryan, K. C.; Maroney, M. J.; Brunold, T. C., Spectroscopic and computational investigation of three Cys-to-Ser mutants of nickel superoxide dismutase: insight into the roles played by the Cys2 and Cys6 active-site residues. *J. Biol. Inorg. Chem.* **2010,** *15*, 777-793.

19. Ryan, K. C.; Johnson, O. E.; Cabelli, D. E.; Brunold, T. C.; Maroney, M. J., Nickel superoxide dismutase: structural and functional roles of Cys2 and Cys6. *J. Biol. Inorg. Chem.* **2010,** *15*, 795-807.

20. Bryngelson, P. A.; Arobo, S. E.; Pinkham, J. L.; Cabelli, D. E.; Maroney, M. J., Expression, reconstitution, and mutation of recombinant Streptomycescoelicolor NiSOD. *J. Am. Chem. Soc.* **2004,** *126*, 460-461.

21. Ryan, K. C.; Guce, A. I.; Johnson, O. E.; Brunold, T. C.; Cabelli, D. E.; Garman, S. C.; Maroney, M. J., Nickel Superoxide Dismutase: Structural and Functional Roles of His1 and Its H-Bonding Network. *Biochemistry* **2015,** *54*, 1016-1027.

22. Schilter, D.; Camara, J. M.; Huynh, M. T.; Hammes-Schiffer, S.; Rauchfuss, T. B., Hydrogenase Enzymes and Their Synthetic Models: The Role of Metal Hydrides. *Chem. Rev.* **2016,** *116*, 8693-8749.

23. Wuerges, J.; Lee, J.-W.; Yim, Y.-I.; Yim, H.-S.; Kang, S.-O.; Carugo, K. D., Crystal structure of nickel-containing superoxide dismutase reveals another type of active site. *Proc. Natl. Acad. Sci. U. S. A.* **2004,** *101*, 8569-8574.

24. Truong, P. T.; Gale, E. M.; Dzul, S. P.; Stemmler, T. L.; Harrop, T. C., Steric Enforcement about One Thiolate Donor Leads to New Oxidation Chemistry in a NiSOD Model Complex. *Inorg. Chem.* **2017,** *56*, 7761-7780.

25. Gale, E. M.; Simmonett, A. C.; Telser, J.; Schaefer, H. F.; Harrop, T. C., Toward Functional Ni-SOD Biomimetics: Achieving a Structural/Electronic Correlation with Redox Dynamics. *Inorg. Chem.* **2011,** *50*, 9216-9218.

26. Linnell, R., Notes- Dissociation Constants of 2-Substituted Pyridines. *J. Org. Chem.* **1960,** *25*, 290.

27. Lenarcik, B.; Ojczenasz, P., The influence of the size and position of the alkyl groups in alkylimidazole molecules on their acid-base properties. *J. Heterocycl. Chem.* **2002,** *39*, 287-290.

28. Sachs, D. H.; Schechter, A. N.; Cohen, J. S., Nuclear Magnetic Resonance Titration Curves of Histidine Ring Protons. *J. Biol. Chem.* **1971,** *246*, 6576-6580.

29. Rayer, A. V.; Sumon, K. Z.; Jaffari, L.; Henni, A., Dissociation Constants (pKa) of Tertiary and Cyclic Amines: Structural and Temperature Dependences. *J. Chem. Eng. Data* **2014,** *59*, 3805-3813.

30. Ragsdale, S. W., Nickel-based Enzyme Systems. *J. Biol. Chem.* **2009,** *284*, 18571-18575.

31. Platzer, N.; Goasdoue, N.; Davoust, D., Long‐range 1H coupling interactions: Identification of different pathways by 2D NMR δ—δ correlated spectroscopy. Applications in structural analysis. *Magn. Reson. Chem.* **1987,** *25*, 311-319.

32. Daisuke, N.; Yasuhiro, F.; Tomohiro, O.; Hideki, M., A Square-planar Ni(II) Complex with an Asymmetric N_2S_2 Donor Set as a Model for the Active Site of Nickel-containing SOD: Structural Conversion Driven by Addition of a Strong Donor Ligand in the High Oxidation State. *Chem. Lett.* **2010,** *39*, 344-346.

33. Shearer, J.; Zhao, N., [Me_4N][Ni^{II}(BEAAM)): A Synthetic Model for Nickel Superoxide Dismutase That Contains Ni in a Mixed Amine/Amide Coordination Environment. *Inorg. Chem.* **2006,** *45*, 9637-9639.

34. Mathrubootham, V.; Thomas, J.; Staples, R.; McCraken, J.; Shearer, J.; Hegg, E. L., Bisamidate and Mixed Amine/Amidate NiN_2S_2 Complexes as Models for Nickel-Containing Acetyl Coenzyme A Synthase and Superoxide Dismutase: An Experimental and Computational Study. *Inorg. Chem.* **2010,** *49*, 5393-5406.

35. Nakane, D.; Wasada-Tsutsui, Y.; Funahashi, Y.; Hatanaka, T.; Ozawa, T.; Masuda, H., A novel square-planar Ni(II) complex with an amino-carboxamido-dithiolato-type ligand as an active-site model of NiSOD. *Inorg. Chem.* **2014,** *53*, 6512-6523.

36. Senaratne, N. K.; Mwania, T. M.; Moore, C. E.; Eichhorn, D. M., Ni complexes of N_2S ligands with amine/imine and amine/amide donors with relevance to the active site of Ni superoxide dismutase. *Inorg. Chim. Acta* **2018,** *476*, 27-37.

37. Shearer, J.; Peck, K. L.; Schmitt, J. C.; Neupane, K. P., Cysteinate protonation and water hydrogen bonding at the active-site of a nickel superoxide dismutase metallopeptide-based mimic: implications for the mechanism of superoxide reduction. *J. Am. Chem. Soc.* **2014,** *136*, 16009-16022.

38. Yang, L.; Powell, D. R.; Houser, R. P., Structural variation in copper(I) complexes with pyridylmethylamide ligands: structural analysis with a new four-coordinate geometry index, τ_4. *Dalton Transactions* **2007**, 955-964.

39. Pavlishchuk, V. V.; Addison, A. W., Conversion constants for redox potentials measured versus different reference electrodes in acetonitrile solutions at 25°C. *Inorg. Chim. Acta* **2000,** *298*, 97-102.

40. Nakane, D.; Funahashi, Y.; Ozawa, T.; Masuda, H., Synthesis of an N_3S_2-type Ni(II) Complex Directed to NiSOD Active Site and Its Structural, Electrochemical, and Spectroscopic Properties. *Trans. Mater. Res. Soc. Jpn* **2009,** *34*, 513-516.

41. Bakar, N. A.; Hashim, N.; Mahamod, W. R. W.; Abd Azziz, S. S. S.; Juahir, Y.; Yahaya, R.; Fah, W. C.; Ibrahim, R.; Aziz, M. F.; Basir, N. A. M., The Potential of Ferrocenium as a Sensing Reagent for Determination of 2, 4, 6-Trichlorophenol in Water Samples. *J. Sci. Math. Lett. UPSI* **2015,** *3*, 15-23.

42. Gale, E. M.; Patra, A. K.; Harrop, T. C., Versatile Methodology Toward NiN_2S_2 Complexes as Nickel Superoxide Dismutase Models: Structure and Proton Affinity. *Inorg. Chem.* **2009,** *48*, 5620-5622.

43. O'Neil, J. P.; Wilson, S. R.; Katzenellenbogen, J. A., Preparation and structural characterization of monoamine-monoamide bis(thiol) oxo complexes of technetium(V) and rhenium(V). *Inorg. Chem.* **1994,** *33*, 319-323.

44. McCarthy, C.; Walker, E. R.; McMahon, P. S.; Frédéric, J.; Moulton, B.; Rogers, J. HYDROXAMATE COMPOUNDS AS ANTAGONISTS OF THE ADENOSINE A2A RECEPTOR. 30 December, 2020.

45. Fulmer, G. R.; Miller, A. J. M.; Sherden, N. H.; Gottlieb, H. E.; Nudelman, A.; Stoltz, B. M.; Bercaw, J. E.; Goldberg, K. I., NMR Chemical Shifts of Trace Impurities: Common Laboratory Solvents, Organics, and Gases in Deuterated Solvents Relevant to the Organometallic Chemist. *Organometallics* **2010,** *29*, 2176-2179.

46. Neese, F.; Wennmohs, F.; Becker, U.; Riplinger, C., The ORCA quantum chemistry program package. *J. Chem. Phys.* **2020,** *152*, 224108.

47. Wang, Y.; Jin, X.; Yu, H. S.; Truhlar, D. G.; He, X., Revised M06-L functional for improved accuracy on chemical reaction barrier heights, noncovalent interactions, and solid-state physics. *P. Natl. Acad. Sci.* **2017,** *114*, 8487-8492.

48. Grimme, S.; Antony, J.; Ehrlich, S.; Krieg, H., A consistent and accurate ab initio parametrization of density functional dispersion correction (DFT-D) for the 94 elements H-Pu. *J. Chem. Phys.* **2010,** *132*, 154104.

49. Weigend, F.; Ahlrichs, R., Balanced basis sets of split valence, triple zeta valence and quadruple zeta valence quality for H to Rn: Design and assessment of accuracy. *Phys. Chem. Chem. Phys.* **2005,** *7*, 3297.

50. Weigend, F., Accurate Coulomb-fitting basis sets for H to Rn. *Phys. Chem. Chem. Phys.* **2006,** *8*, 1057.

51. Sheldrick, G., Crystal structure refinement with SHELXL. *Acta Crystallographica Section C* **2015,** *71*, 3-8.

CHAPTER 3

CONCLUSIONS

Our group has successfully designed, synthesized, and characterized the most structurally accurate NiSOD low molecular weight model complex by incorporating 1-methylimidazole (NImMe) as the axial N-donor onto a well-studied mixed peptide/amide dithiolate ligand frame. Few examples of five-coordinate (5C) NiSOD model complexes exist in the literature and none with a structurally and electronically appropriate axial N-donor. This $[N_3S_2]^{3-}$ ligand is poised to coordinate Ni in a 5C, square-pyramidal geometry and exhibit SOD functionality. Spectroscopic and structural characterization of this latest complex reflect that of prior model complexes and the reduced state of NiSOD with an unbound axial N-donor. Electrochemical analysis of this complex is irreversible and suggests primarily S-based electrochemical events. Reactivity studies with ambient air and chemical oxidants indicate S-oxygenation but is still very different from similar studies with prior complexes. The unique spectral changes of this complex upon oxidation align with several features of oxidized NiSOD and therefore suggest an electronic structure more similar to NiSOD, specifically, a less S-based HOMO. Future work with this complex will involve oxidation experiments at low temperatures to capture unstable Ni^{3+} and visualize it with electron paramagnetic resonance (EPR) spectroscopy. Additionally, room-temperature experiments monitored by UV-vis and NMR may also provide more insight into the species forming during the reactivity studies discussed in this work.

In summary, this work emphasizes the role of the axial N-donor and specifically, its Lewis basicity and field strength. These results also highlight the essential role of the secondary sphere

of NiSOD in arranging the active site appropriately and supports mutagenic and theoretical biochemical works that conclude the same. Design and synthesis of a structurally and electronically accurate NiSOD model complex capable of $Ni^{3+/2+}$ redox and SOD functionality remains challenging though results of this work indicate progress toward that end. The bioinorganic community will continue to benefit from the findings of synthetic analogues such as this most recent complex from our group and the others that have preceded it. Future directions for this work include derivatization of the apical NMeIm N-donor to assess the role of Lewis basicity, ligand field strength, and secondary structure/H-bonding as well as thiolate modification to answer remaining questions about the proton source of NiSOD. This current and future work is anticipated to provide answers as to the role of the ligands and secondary structure in NiSOD, the proton source for the reductive half reaction of disproportionation, and the substrate binding mode which make NiSOD such an exceptional SOD and Ni metalloenzyme. Beyond the context of NiSOD, this work will also contribute to the broader field of redox-active Ni metalloenzyme chemistry and Ni-thiolate chemistry, which are related to reactions of environmental and physiological importance including the global carbon (CH_4, CO, CO_2), hydrogen (H_2), and oxygen (O_2, $O_2^{\bullet-}$, H_2O_2) cycles.